

UCLA

UCLA Electronic Theses and Dissertations

Title

Translational Research for Biophotonics Image-Guided Surgery

Permalink

<https://escholarship.org/uc/item/06h07815>

Author

Cheng, Harrison

Publication Date

2018

Peer reviewed|Thesis/dissertation

UNIVERSITY OF CALIFORNIA

Los Angeles

Translational Research for
Biophotonics Image-Guided Surgery

A dissertation submitted in partial satisfaction
of the requirements for the degree
Doctor of Philosophy in Bioengineering

by

Harrison Cheng

2018

© Copyright by
Harrison Cheng
2018

ABSTRACT OF THE DISSERTATION

Translational Research for
Biophotonics Image-Guided Surgery

by

Harrison Cheng

Doctor of Philosophy in Bioengineering
University of California, Los Angeles, 2018
Professor Warren Grundfest, Chair

There are many challenges to translating bench-top research biophotonics imaging system into the clinical setting. One commonality amongst many of these systems is that they fall short in the final *in vivo* clinical translation, which is the most critical step to truly have a clinical impact. The intent of this PhD thesis is to offer a comprehensive view of a project cycle and to provide insight that are important to successful clinical translation of research systems into the clinic setting. Many of these issues are typically neglected in academic setting due to the lack of academic novelty and publication possibilities; but is necessary for successful clinical translation. Some of these issues includes poor clinical practicality, high system complexity, and inconsistent results. The thesis will use the system development and clinical translation of Dynamic Optical Contrast Imaging (DOCI), a novel imaging system that uses fluorescence decay as the contrast mechanism to differentiate tissue types; as an example to address translational challenges. The research can be divided into a few distinct sections such as the development of DOCI system, challenges and considerations for clinical translation, and algorithm development for image processing and interpreting data. Each of the sections will entail solutions to improve clinical practicality, reduce system complexity, or attempts to standardize results across multiple systems.

The dissertation of Harrison Cheng is approved.

Tsu-Chin Tsao

Oscar M. Stafsudd

Zachary Deis Taylor

Maie A.R. St. John

Warren Grundfest, Committee Chair

University of California, Los Angeles

2018

*I wish to dedicate this work to the my professors, teachers, mentors, colleagues, friends,
and family for the support in my educational aspirations that made this doctoral research
possible.*

TABLE OF CONTENTS

1	Introduction	1
1.1	Clinical Significance - Intraoperative Tissue Differentiation	1
1.1.1	Head & Neck Squamous Cell Carcinoma	2
1.1.2	Parathyroid Detection	3
1.2	Intraoperative Biophotonic Imaging Systems	5
1.3	Role of Dynamic Optical Contrast Imaging (DOCI)	5
1.4	Fluorescence & Fluorescence Decay Imaging	6
2	Dynamic Optical Contrast Imaging (DOCI) Project Overview	10
2.1	System Development	11
2.2	Data Acquisition	14
2.3	Data Storage	16
2.4	Image Processing	16
2.5	Data Analysis	17
2.6	System Optimization	17
2.7	Conclusion	17
3	Dynamic Optical Contrast Imaging (DOCI) - Theory & Model	19
3.1	Idealized Model	20
3.1.1	Single Exponential Model	21
3.1.2	Multi-exponential Model	24
3.2	Model with Illumination Decay	25
3.2.1	Single Exponential Model	27
3.2.2	Multi-exponential Model	32

3.3	System Noise	33
3.4	Discussion	34
3.5	Conclusion	35
4	System Implementation	36
4.1	System Overview	36
4.2	Optics	39
4.3	Contrast Mechanism	41
4.4	Electronics	42
4.5	Discussion	45
5	Calibration	47
5.1	Methods & Materials	47
5.1.1	Calibration Dye Selection Criteria & Preparation	47
5.1.2	Time-Domain FLIM Characterization Method	48
5.1.3	Time-Domain FLIM Data Analysis	49
5.1.4	DOCI Characterization Method	51
5.1.5	DOCI Data Analysis	54
5.1.6	DOCI Computational Modeling	54
5.2	Results	55
5.3	Discussion	57
6	Clinical Data Acquisition	59
6.1	Software Automation Tools	59
6.2	Experimental Procedure	62
6.2.1	Human <i>ex vivo</i>	62

6.2.2	Human <i>in vivo</i>	64
6.3	DOCI Image Results	66
6.4	Experiment & Patient Documentation	69
6.4.1	Image Registration - 1st Iteration	72
6.4.2	Image Registration - 2nd Iteration	76
6.4.3	Image Registration - 3rd Iteration	79
6.5	Discussion	80
7	Image Processing	81
7.1	Motion Correction	81
7.2	Scale-Invariant Feature Transform (SIFT) Overview	82
7.3	Motion Correction Results	85
7.4	Discussion	88
8	Conclusion	90
9	Future Work	91
9.1	Data Management	91
9.2	Registration, Region of Interest Selection, and Multivariate Statistical Analysis	92
9.3	Noise Characterization	93
9.4	Illumination Source	94
9.5	Progress of Surgery	94
A	Appendix - Theory	96
A.1	main idealModel function	96
A.2	main parameterEffect function	97

B Appendix - Calibration	100
B.1 main FLIM function	100
B.2 analyzeDye function	103
B.3 main FLIM vs DOCi function	107
C Appendix - SIFT Implementation	112
C.1 main checkRaw function	112
C.2 generateRGB function	115
C.3 generateLT function	117
C.4 motionCorrect function	120
D Other	125
References	126

LIST OF FIGURES

1.1	(left) Example of conventional time-domain method and (right) frequency domain method.	7
2.1	Outline of DOCI project.	10
3.1	(left) Comparison between conventional time-domain method, (center) frequency domain method (center), and (right) DOCI method.	19
3.2	Comparison of the closed form solution and simulated convolution model for $q(t)$. The model is partitioned into four fluorescence states R1, R2, R3, and R4.	22
3.3	Comparison of $q(t)$ between with and without excitation decay. The model is also partitioned into four fluorescence states R1, R2, R3, and R4.	28
3.4	<i>(top)</i> Simulated linear decay model vs model with insufficient integration time. <i>(bottom)</i> Residual error deviation from linear model and β constant factor amongst different decay times	30
3.5	<i>(top)</i> Simulated linear decay model vs model with sufficient integration time. <i>(bottom)</i> Residual error deviation from linear model and β constant factor amongst different decay times	31
4.1	DOCI system diagram.	36
4.2	Different iterations of the DOCI system implementation.	37
4.3	Camera quantum efficiency specifications. <i>(left)</i> Generation 2 detector and <i>(right)</i> generation 3 detector provided by Andor.	40
4.4	<i>(left)</i> Optical bandpass filter spectra [1] and <i>right</i> major biological fluorophore absorption and fluorescence spectrum [2].	41
4.5	DOCI illumination circuit diagram.	43
4.6	Comparison of measured and modeled DOCI illumination profile.	44

5.1	Time-domain FLIM dye calibration system setup that consists of the nitrogen laser, dye sample, optical filter, and photodetector.	49
5.2	Intensity profile for excitation laser pulse, dye fluorescence measurements, and fitted predicted model.	51
5.3	DOCI dye calibration system setup that consists of UV-LEDs, dye sample, optical filter, imaging lens, and detector.	52
5.4	Comparison of measured and modeled DOCI illumination profile.	53
5.5	<i>(left)</i> Time-domain FLIM and <i>(right)</i> DOCI method results for each calibration dyes.	56
5.6	Fluorescence lifetime-DOCI curve that compares the experimental results, simulated results, fitted empirical results, and theoretical model.	57
6.1	Initial software user interface provided by Andor and Optec.	60
6.2	Software interface developed in LABVIEW to provide automation features. . . .	61
6.3	Human <i>ex vivo</i> clinical experimental procedure.	63
6.4	Human <i>in vivo</i> clinical experimental procedure.	65
6.5	Human <i>ex vivo</i> SCCA image results. <i>(left)</i> Multi-spectral DOCI images, <i>(top-right)</i> DSLR color image, and <i>(bottom-right)</i> H&E stained histology image. . . .	66
6.6	Human <i>ex vivo</i> parathyroid image results. <i>(left)</i> Multi-spectral DOCI images, <i>(top-right)</i> DSLR color image, and <i>(bottom-right)</i> H&E stained histology image. . . .	67
6.7	Human <i>in vivo</i> lip image results. Multi-spectral DOCI <i>(left)</i> normal lip and <i>(right)</i> abnormal lip.	68
6.8	Simplified ideal database proposal.	70
6.9	Microsoft Excel-MATLAB DOCI experiment database/table implementations. <i>(left)</i> Microsoft Excel user input table. <i>(right)</i> MATLAB converted table.	71
6.10	Database filtering and case selection. <i>(left)</i> Filtering by tissue types for data analysis. <i>(right)</i> Filtering by patient for histopathology-DOCI registration. . . .	73

6.11	First DOCI image ROI selection.	74
6.12	DOCI region of interest (ROI) database implementations. <i>(top)</i> Manual registration between DOCI data and histology reference. <i>(bottom)</i> ROI database for each respective experiment.	75
6.13	DOCI experiment and histology registration.	77
6.14	Second DOCI experiment ROI selection. <i>(left)</i> ROI selection on DOCI image. <i>(right)</i> ROI selection on histology image.	77
6.15	DOCI region of interest (ROI) database implementation. <i>(top)</i> ROI database from each experiment, <i>(bottom)</i> ROI database with pathologist’s labeling, and <i>right</i> histology with ROI annotations.	78
6.16	Third DOCI image ROI selection.	79
7.1	Image scale space.	82
7.2	Visualization of Gaussian curves and Different of Gaussians. <i>(red)</i> and <i>(green)</i> curves are Gaussians with different σ s. <i>(blue)</i> curve is the the resultant DoG curve that is computed by the subtraction between the two Gaussian curves. . .	83
7.3	Identifying local ”3-D” optima by stacking multiple DoG frames.	83
7.4	Gradient vector map for each optima.	84
7.5	Example of SIFT features mapping. <i>(left)</i> Steady state fluorescence image and <i>(right)</i> decay state image	85
7.6	Example of SIFT algorithm applied to RGB images. <i>(left)</i> Before motion correction and <i>(right)</i> after motion correction	85
7.7	DOCI result before motion correction for both normal and abnormal lip	86
7.8	DOCI result before and after motion correction for normal lip	87
7.9	DOCI result before and after motion correction for abnormal lip	87
7.10	DOCI result after motion correction for both normal and abnormal lip	88

9.1	<i>(left)</i> Automated RGB background segmentation, <i>(center)</i> automated region of interest clustering, and <i>(right)</i> feature analysis using machine learning techniques.	92
9.2	<i>(top)</i> Intraocular robotic interventional and surgical system (IRISS) a pseudo-automated cataract robotic surgery and <i>(bottom)</i> progression of surgery.	95

LIST OF TABLES

4.1 Trade-off of different imaging lens.	39
--	----

ACKNOWLEDGMENTS

The work presented in this thesis could not have been completed without the help of many others. First and foremost, I am grateful to my committee members, Dr. Warren Grundfest, Dr. Maie St John, Prof Zachary Taylor, Prof Tsu-Chin Tsao, and Prof Oscar Stafsudd for their patient mentorship and providing a flexible and accessible research environment that allowed many of the exploratory work. The works of numerous researchers have made intellectual contribution to this thesis, of whom only a limited number are directly credited in this document.

All of the clinical work was made possible by clinical collaborators from UCLA Ronald Reagan Medical Center that contributed to the research. The human tissue specimens were provided by numerous surgeons from UCLA Head & Neck Surgery; and the histopathology processing were performed by UCLA Surgical Pathology and UCLA Translational Pathology Core Lab (TPCL). I am grateful to Dr. Miguel Fernando Palma Diaz & Dr. Gregory A. Fishbein for spending their valuable time experimenting with different pathology research processes. I am grateful to all the surgical residents that I worked closely with on a day-to-day basis, which includes Dr. Irene Kim, Dr. Jon St. Clair, Dr. Julianna Pesce, Dr. Kelly Pettijohn, and Dr. Karam Badran for their patience with experimenting new research process.

Additionally, I am grateful for the technical engineering guidance and assistance by George Saddik, Asael Papour, Brad Liu, Christian Vega, Chengwei Chen, Yao Xie, Yong Hu, and Peter Pellionisz. I also had several undergraduate students that I am truly grateful for in providing assistance with the development of challenging preliminary work. Aidan Pearigen and Khuzaima Rangwalla made contributions to the calibration work; Eddie Kim and Jonathan Baruch experimented with image processing algorithms; and Carlos Zhang with many mechanical designs.

Lastly, the work presented in this thesis was made possible and funded by the National Institute of Health (NIH) (1R01CA205051-01A1, 1R01CA220663-01A1); and Tobacco-Related Disease Research Program of the University of California (TRDRP-UC) (24RT-0029).

VITA

- 2009 Undergraduate Researcher, "Anatomically Correct Testbed (ACT) Hand", Neurobotics Lab, Computer Science Department, University of Washington–Seattle.
- 2010 Clinical Shadowing–Surgical Oncology, General Surgery Department, University of Washington–Seattle.
- 2010–2012 Undergraduate Researcher, "Spiral Imaging Waveform and Image Reconstruction" & "Automated Optical Coherence Tomography (OCT) Alignment", Biophotonics and Imaging Lab (BAIL) Lab, Bioengineering Department, University of Washington–Seattle.
- 2012–2013 Volunteer, Software Mentor–Robotics Club, Nathan Hale High School, Seattle, Washington.
- 2013 B.S. (Bioengineering), University of Washington–Seattle.
- 2014–2017 Graduate Student Consultant–Lead Optical Engineer, "Pseudo–Automated Robotic Cataract Surgery", Mechatronics Lab, Center for Advance Surgical Intervention Technology (CASIT), Mechanical Engineering Department, UCLA.
- 2014–present Graduate Student Researcher–Systems Engineer, "Translational Research for Biophotonics Image–Guided Surgery" and "Dynamic Optical Contrast Imaging (DOCI)", Biophotonics Lab, Center for Advance Surgical Intervention Technology (CASIT), Bioengineering Department, UCLA.
- 2018 Group Mentor–Intro to Digital Imaging, Engineering Department, UCLA.
- 2018 Teaching Assistant–Intro to Digital Imaging, Engineering Department, UCLA.

CHAPTER 1

Introduction

Translational research is the process of translating basic scientific discoveries to clinical applications with the goal to ultimately improve public health [3]. Biophotonics is an interdisciplinary field that intersects diverse engineering, life sciences, and physical sciences to understand light-tissue interactions. Through greater understanding of light-tissue phenomenon, diagnostic and therapeutic applications can be developed to advance medicine [4, 5]. Image-guided surgery is the application specific field of providing surgeons with real-time imaging technologies to assist in surgical guidance and decision making [6–8]. "Translational Research for Biophotonics Image-guided Surgery" is the composition of these disciplines and are often separated in academic research. The goals and requirements for each of these disciplines are typically different. Translational research typically requires intuitive and streamlined process in order to educate clinical practitioners to follow a specific process. Biophotonics research is advancing the engineering of instrumentation and enhancing our understanding of biology, but may not necessarily allow non-technical users to operate the system. Image-guided surgery requires real-time and non-intrusive methods to enhance current surgical practice from both the surgeon's and the patient's perspective. The amalgamation of these requirements were considered in this research by using the Dynamic Optical Contrast Imaging (DOCI) project as a model.

1.1 Clinical Significance - Intraoperative Tissue Differentiation

The ability to perform real time tissue differentiation has an enormous implications regardless what the application is. During surgery, the surgeon's experience, visual, and tactile feedback

remains the primary "imaging modalities" used to decide *in situ* surgical decisions [7,8]. Palpation and visual inspection are not always sufficient for discriminating various tissue types and can lead to incomplete resections or the unnecessary removal of healthy tissue [7, 8]. There are currently a few imaging modalities are routinely used for patient care - radiography (plain film, fluoroscopy, and computed tomography [CT]), magnetic resonance imaging (MRI), ultrasonography (US), single-photon emission computed tomography (SPECT), and positron emission tomography (PET) [6]. However, none of these imaging modalities are translatable into surgical setting where the patient's anatomy and physiology is highly dynamic. Furthermore, frozen sections are typically performed during surgery as a method to provide detailed confirmation of tissue type to surgeons, but the process can take between 20-60min depending on the availability of pathologists. During this time, the surgeon has to wait for confirmation and manage the patient before the surgery can progress. Histopathology is the current gold standard to validate tissue types of interest, but cannot be performed during surgery and typically takes 1-7days for the specimen to be processed. The focus of the DOCI research project is to address these issues by attempting real-time tissue differentiation at different stages of surgery. The primary clinical focus will be for head & neck applications, specifically squamous cell carcinoma (SCCA) and parathyroid localization.

1.1.1 Head & Neck Squamous Cell Carcinoma

Head and neck cancers are debilitating diseases where patient prognosis depends heavily on complete tumor resection. Currently, a battery of preoperative imaging and biopsy techniques are used to assess tumor size and the progression of the disease. However, intraoperative margin detection relies solely on visual and tactile feedback during surgical resection. After the tumor is removed, the assessment of the margins is performed with frozen section microscopy. Additional surrounding tissues are continued sampled by frozen section in an effort to ensure that no cancerous cell remains. The efficacy of this approach varies widely and is subject to sampling error.

Numerous optical and ultrasonic techniques for margin detection have not succeeded

clinically for many reasons. Fluorescence imaging has produced very promising results, but deconvolution of *in vivo* image contrast confounders from the acquired data has proven difficult [9–15]. Infrared imaging in general has been relatively nonspecific and requires the use of exogenous fluorophores [16]. A variety of ultrasound techniques have been explored for margin detection, but the bulk of these have not been applied to head and neck cancers [17–25]. A small number of studies have been published regarding the application of ultrasound to head & neck SCCA detection and imaging, but the bulk of the work is limited to guiding fine needle aspirations [26]. Currently, there is a lack of intraoperative tools to delineate tumor margins in real-time.

1.1.2 Parathyroid Detection

There are two types of clinical applications that requires parathyroid detection. The first is surgeries that require removing abnormal parathyroid glands. Primary hyperparathyroidism is a disease can lead to elevated parathyroid hormone (PTH) levels, which results in hypercalcemia [27–29]. There are several associated morbidities that results from hypercalcemia, or elevated calcium levels in the blood [29]. Surgical excision of the abnormal parathyroid is the current standard of care to reduce PTH and calcium levels back to to baseline. The small size, variable location, and indistinct external features of parathyroid glands makes distinguishing them from adjacent fat, lymph tissue, or thymus tissue challenging during surgery [30,31]. Patient outcome and well-being depends heavily on complete resection of the involved parathyroid glands.

The second type of clinical application that requires parathyroid detection includes other neck surgeries where the surgeon wants to ensure that normal parathyroids are not removed. Accidental removal of healthy parathyroid glands during thyroid surgery causes postoperative hypocalcemia, which also induces a range of symptoms [30,31]. Approximately 80,000 parathyroid and thyroid surgeries are performed in the United States each year and one of the most common problems in these surgical intervention is the inability to localize the parathyroid glands [30,31]. Thyroid and parathyroid surgery involves dissection through

skin and subcutaneous tissues, retraction of neck muscles, and careful dissection of the thyroid gland as the parathyroid glands are most often located on the posterior surface of the thyroid. In cases where the parathyroid glands are diseased, insufficient removal of affected parathyroid glands during parathyroidectomy can require reoperation due to persistent hypercalcemia [30,31].

Similar to the clinical management in surgical oncology, the current intraoperative practice for validating parathyroid glands include frozen section analysis and intact PTH assay via blood test. However, a biopsy or partial excision of the gland is needed in order to obtain parathyroid tissue for the frozen section validation. This procedure risks damage to the parathyroid gland's local blood supply [30,31]. The efficacy of frozen section analysis varies widely and is subject to sampling error and is not always reliable. The other intraoperative validation test is the intact PTH assay, which is a blood test that is drawn fifteen minutes after the candidate diseased parathyroid is excised during surgery. If the intact PTH level drops significantly as compared to preoperative levels, the surgeon is informed that the diseased gland(s) have been removed. The utility of this test is somewhat debated because the intact PTH assay suffers from false-negative rates and is usually employed *ex vivo* once the parathyroid has been excised, thus offering no assistance in intraoperative parathyroid localization [30,31]. Furthermore, not all hospitals are equip to perform PTH assay tests. There is currently no intraoperative method for identifying the parathyroid gland. Surgeons must rely on visual and tactile cues, which is highly subjective and dependent on experience [30,31].

A multitude of imaging studies like ultrasonography (US), ^{99m}Tc - sestamibi SPECT/CT (SeS), computed tomography (CT), and magnetic resonance imaging (MRI), but the choice and quality of imaging studies differ depending on surgeon preference, technology availability, and operator skill [32]. The sensitivities for ultrasonography and sestamibi imaging glands varies widely and may not be particularly reliable [32,33]. SeS requires administering radiotracers and results can be affected by nonselective tissue uptake. Ultrasonography is widely utilized, but is suboptimal in patients with co-existing nodular thyroid disease or deep-seated adenomas [27]. These methods are limited by their inability to reliably localize

parathyroid glands or provide rapid intraoperative information [30, 31]. There is a critical need for an improved intraoperative imaging method for rapid parathyroid identification.

1.2 Intraoperative Biophotonic Imaging Systems

Biophotonic imaging systems that are currently adapted in the operating room can be generalized to use three distinct contrast mechanisms each with varying diversities of form factors. There is brightfield imaging, which is the conventional 8-bit RGB color image. There is continuous wave spectroscopy that uses reflectance and fluorescence property of tissue. These include imaging using infrared, dye-specific contrast agents, and wavelength-specific illumination and acquisition [7, 8]. Lastly, there is optical coherence tomography (OCT), which uses interferometry techniques to reconstruct 3-D volumetric images [34]. Form factors of each of these imaging modalities can range from endoscopic designs, hand-held probes, surgical microscopes, or a bulk imaging module at the distal region of a mechanical arm. Imaging systems that use alternative contrast mechanisms have stayed in academic research and have low clinical translation yield [3, 35]. The reasons may be due to poor practicality, complex operational use, or inconsistent clinical results [36–38].

1.3 Role of Dynamic Optical Contrast Imaging (DOCI)

Dynamic optical contrast imaging (DOCI) is an imaging technique that seeks to generate contrast from relative differences in fluorophore lifetime ratios without the need to compute absolute lifetime values. Conventional fluorescence lifetime imaging microscopy (FLIM) are powerful tools for tissue differentiation in the *ex vivo* lab setting, but complex, computationally intensive data fitting routines are impractical towards real-time visualization and intraoperative guidance for the surgeon. Data are often fit to an exponential decay model, a set of Laguerre polynomials, or frequency analysis from the phasor approach to extract coefficients related to decay times [39–43]. In addition, uniquely resolving the macroscopic lifetimes of heterogeneous tissues remains challenging when considering unknown mixing

ratios, diverse multi-exponentials, and variations in individual fluorophore lifetimes due to underlying physiological and biochemical properties of tissue [44, 45].

The DOCI method is a ratiometric version of time-resolved autofluorescence imaging in which the weighted ratios of endogenous tissue fluorophore lifetimes provides image contrast [46]. These fluorophores mainly consist of collagen, elastin, reduced nicotinamide adenine dinucleotide (NADH), oxidised flavins, lipofuscin, keratin, and porphyrins [47]. Fluorescence lifetime is an intrinsic property of tissue that the DOCI method utilizes in order to provide quantitative measurements via an image. Furthermore, the absence of dye or injected contrast simplifies the use of this technique in an intraoperative environment. Prior work have provided a conceptual approach for the DOCI algorithm [48–50]; and remarkable contrast have been demonstrated between different tissue types in *ex vivo* pilot studies with human tissue [51, 52].

There is also a growing concern where many scientific and medical findings are neither repeatable nor reproducible [36–38]. The National Institute of Health (NIH) has funded >\$20 billion every year since 1994, but the rate of translation of this work into clinical practice has been low [3, 35, 53]. Studies have found that less than 25% of highly promising medical discoveries resulted in a published randomized clinical trial and less than 10% were established in clinical practice within the past 20 years [3, 35]. The DOCI project also aims to identify these issues by providing varying methods for calibrating the system, provide diverse solutions for reducing human error, and improving data reproducibility by partitioning patient populations.

1.4 Fluorescence & Fluorescence Decay Imaging

A fluorophore excited by a photon may spontaneously emit another photon through the phenomenon of fluorescence. This process has been modeled as a first order differential equation and is shown in Eq. (1.1), where a is the rate of decay and $f(t)$ is the fluorescence intensity response with respect to time. Notably, this formula assumes the fluorophore does

not possess multiple conformational states of different lifetimes.

$$\frac{df(t)}{dt} = -af(t) \quad (1.1)$$

When solving for the first order differential equation, the resultant time-domain response is an exponential decay as shown in Eq. (1.2) where i_0 is the initial fluorescence yield and τ is the inverse of the decay rate (a), termed the time it takes for the decay to reach 37% of the initial response [47].

$$f(t) = i_0e^{-at} = i_0e^{-\frac{t}{\tau}} \quad (1.2)$$

Conventionally, the methods for acquiring fluorescence lifetime data operate in the time-domain or the frequency-domain. The optical setup and utilized detectors will differ in regards to the chosen technique. The measured response of the acquired fluorescence lifetime signal, however, $g(t)$ can be commonly described as the convolution of the fluorescence decay response $f(t)$ and the excitation response $h(t)$, as shown in Eq. (1.3).

$$g(t) = f(t) * h(t) \quad (1.3)$$

Figure 1.1 illustrates the excitation of a fluorophore with the subsequent fluorescence optical response in both the conventional time-domain and also the frequency-domain lifetime techniques.

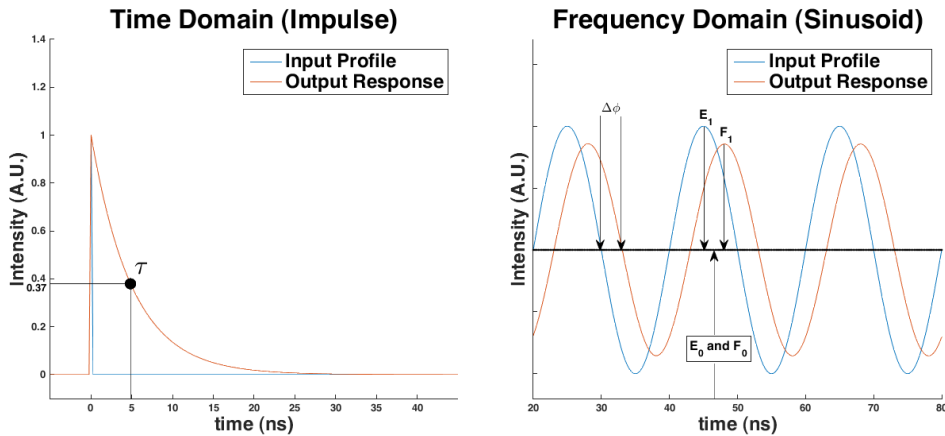


Figure 1.1: (left) Example of conventional time-domain method and (right) frequency domain method.

Following data acquisition, the fluorescence lifetime constant τ for both approaches is mathematically calculated. In the time-domain method, an ultra-short subnanosecond full-width half-maximum laser pulse is generally used as the source of excitation, which can be modeled as a dirac $\delta(t)$ function as $i(t)$ [54]. Experimentally, the input source will typically exhibit a subnanosecond full-width half-maximum Gaussian pulse. This requires deconvolving the measured decay profile with the excitation pulse before performing the decay fit to accurately extract mono-exponential fluorescence lifetime. Otherwise, if the deconvolution is not performed, the computed fluorescence decay would seem slightly longer than the actual lifetime property [47].

The homodyne frequency-domain fluorescence lifetime method uses an excitation source that is modulated in a sinusoidal pattern. The fluorescence lifetime response can then be extracted using the amplitude (M), phase (ϕ), and frequency (ω) of the modulated excitation and resultant fluorescence response as shown in Eq. (1.4) and Eq. (1.5). Eq. (1.6) shows the magnitude ratio for amplitude based lifetime.

$$\tau_{\phi} = \frac{\tan(\Delta\phi)}{\omega} \quad (1.4)$$

$$\tau_{Amp} = \frac{\sqrt{\frac{1}{M^2-1}}}{\omega} \quad (1.5)$$

$$M = \frac{F_1 E_0}{F_0 E_1} \quad (1.6)$$

Practical concerns when using these methods includes long computation times (>1min/image) needed when trying to reconstruct high pixel count images for the conventional time-domain methods [55]; and high average power in the illumination source using the frequency-domain excitation method, which is not practical for biological samples [56]. Also, the different initial conditions and assumptions in many fitted models can result in decay constant profiles that are non-unique for multi-exponential decays. The DOCI method does not suffer from these disadvantages. Instead, the DOCI method was developed because it is impractical to uniquely identify all relevant fluorophores, know their mixing ratios, and pinpoint the dynamically changing lifetimes due to physiological effects. The trade-off of the DOCI method is to sacrifice identification of fluorophore for speed and practicality while offering

enough contrast for tissue differentiation.

CHAPTER 2

Dynamic Optical Contrast Imaging (DOCI) Project Overview

The clinical translation of the DOCI project is organized into six major phases in a cyclical process with the goal to utilize the DOCI system for surgical guidance as shown figure 2.1.

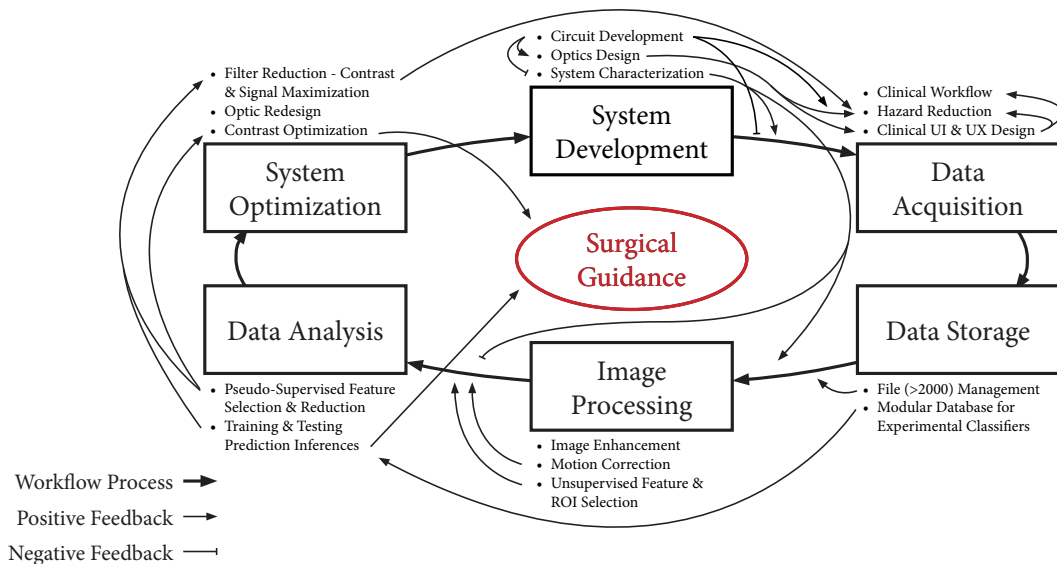


Figure 2.1: Outline of DOCI project.

The bullet points in each phase represents the challenges and tasks that were explored during the process of developing this thesis and is not an exhaustive list. The intent of the chart is to provide a visual to show the connections amongst various important aspects of the project. It is also to demonstrate that it is very difficult to advance the project if only a few phases are pursued while a few are neglected.

The large arrows that links the six phase are used as workflow guidance of processes,

whereas the two smaller types of arrows used in the bullet points are used to depict the positive and negative feedback loops associated with how it affects specific processes. Positive feedback arrows are used to show that development or advancement in specific tasks can improve certain aspects of the project quality. Negative feedback arrows show that if development is neglected, it will have negative impact on the project. The process starts at the system development phase, which is the initial step to develop a system for testing. Only after a system is developed can clinical experiments be performed. Data organization & database is essential as a method to partition datasets from large patient heterogeneity that have often resulted in skewed or inconsistent results. Image processing techniques are needed to enhance image quality prior to analysis. Data analysis is necessary to identify remarkable, redundant, or meaningless features for tissue differentiation. Lastly, using the analyzed data results to identify methods to optimize the system for the next system iteration. The system can be used for "surgical guidance" at any time of the project workflow, but true progress will not improve until tasks in data analysis and system optimization are performed. The subsections of this chapter will describe each of the elements in greater details.

2.1 System Development

The three primary tasks that is listed in the system development phase is system characterization, optics design, and circuit development.

System characterization has many forms and tiers that includes developing a robust and generalizable model that can be adapted to different system behavior, developing calibration processes to verify system behavior, finding methods to aggregate and standardize results across multiple systems, and quality control to enable reproducible systems and results. For many imaging systems and almost all research systems, the system characterization is one of the most difficult steps and is the first step in any research cycle. Ubiquitous RGB imaging has methods in white balancing and resolution targets to standardize color schemes and to identify and correct for optical and electronic artifacts. Well-established medical imaging modality like x-ray computed tomography (x-ray CT), magnetic resonance imaging

(MRI), and positron emission tomography (PET) have been developed and standardized using phantoms representative of each respective contrast mechanism.

The transition from physics & engineering to clinical diagnosis often requires exogenous contrast agents to be used as endogenous images often do not provide sufficient information or clarity. However, due to the nature of using contrast agents for visual enhancement, most diagnostic images are taken in transient states that varies amongst patients and time and is often difficult to provide reproducible quantifiable models. This leads to the historic methodology of using qualitative contrast for medical diagnosis and the outcomes are often highly dependent on physician's training & experience.

The inception of the DOCI system was developed based on the notion that the current clinical diagnosis standards use relative contrast and that it is impossible to quantify fluorophores in people as the physical properties are continuously transient and are dependent on acidity (pH), density ratios, temperature, and proximity of other molecules or proteins [45]. Although prior research was to determine whether the DOCI method can provide sufficient contrast to differentiate tissue, this ultimately led the research system in the direction where the behavior was completely relative and the omission of proof of system behavior resulted in data that varied across multiple system and irreproducible data.

Progress in system characterization is needed to strive for data reproducibility, data accuracy, and data aggregation across multiple system and iterations. Chapter 3 will provide a comprehensive model, proof, and outline of the DOCI contrast behavior and methodology to standardize the DOCI system to provide consistent results for known samples. Chapter 5 will reinforce the model using experimental measurements with calibration dyes. While the DOCI value should be theoretically proportionate to fluorescence lifetime values, not characterizing the system can lead to drastic range of values, difficulty to determining system behavior, and prevent robust analytical methods. Furthermore, not characterizing the system noise can lead to poor image quality and data consistency.

The optics design of the system includes several components including the detector, imaging lens, wavelength specific optical filters for contrast selection, and illumination source.

Different types of clinical applications will have different optical setups such as selecting the type of imaging lens to optimize signal, safe working distance, field of view (FOV), and resolvable resolution. For example, parathyroid detection does not require high resolution images as the gland is relatively large and typical surgeries entail removing an entire gland, but requires opto-mechanical setup to access deep neck cavities. On the other hand, the needs for surgical oncology would depend whether the tool is used for real-time guidance, which requires distance between the system and the patient for surgeons to maneuver; or as a post-resection validation that can be performed *ex vivo* and the working distance can be minimized to maximize signal-to-noise and resolution. Furthermore, the spectroscopic selection for both the illumination source and optical filters will depend on the specific types of tissue that needs to be differentiated. The success in the data acquisition phase greatly depends on the clinical application and the optics that are designed for the purpose. Good optics designs can reduce operating hazards, streamline the data collection process, enhance surgeons' performance, and improve patients' comfort when they are awake for applications such as cancer screening. Improving upon existing light-emitting diodes (LED) circuits or using alternative illumination driver circuits can further improve the optical design and integration, such as fiber coupling for hand-held or endoscopic form factors; or improved illumination gradients and control.

This leads to the third critical component for developing the DOCI system, which is the illumination circuit development. Due to the unique operating characteristics of the DOCI system, off-the-shelf drivers and sources are difficult to come by. Prior research explored clinical feasibility of the DOCI method and consisted of a single illumination circuit in which the optical response was difficult to reproduce. As a result, only one DOCI system can be used at a given time and any changes to the system will cause a reset to the data accumulation phase as results will be unreproducible. Furthermore, due to the unconventional operating range of the LED to use electrical power much greater than the original equipment manufacturer (OEM) specifications that is necessary to provide enough signal-to-noise, there is also an uncertainty of the illumination integrity over extended periods of time. Thus, if the illumination circuit development is neglected, it can negatively impact the quality of

the data acquired. However, the data integrity of the project would be substantially increased if better illumination circuit or sources are explored. Furthermore, it could lead to improved optical design by enabling varying form-factors, such as hand-held probe; that could ultimately reduce various hazards in the clinical environment.

2.2 Data Acquisition

After the system is built and tested on phantoms, the process of accumulating patient data needs to be developed. The user interface/experience design entails the process and ergonomics of operating the DOCI system to perform clinical experiments both *in vivo* and *ex vivo*. It is critical to take into account all the potential clinical hazards posed by the system in its current iteration and make improvements to mitigate these hazards in future iterations by improving the optical, mechanical, electrical, and software design. Lastly, there is the clinical logistics of handling tissue, finding methods of correlating DOCI results with the clinical gold standard of histopathology, and also providing accurate annotations to datasets for data analysis.

One of the primary focus of this task is to minimize human intervention redundancy as much as possible. Every button click, file naming, parameter changes to the system, labeling has an intrinsic probability where mistakes can occur especially over long periods of time. Prior to development of software automation, each DOCI experiment would take 20-40min in which hundreds of actions were performed in the form of changing camera parameters for each spectroscopic dataset, changing the filter wheel position through end-user software provided by the vendor, creating folders and providing annotation to save each experiment datasets, and naming files for each spectroscopic dataset. Developing an automated software user interface for operating the system can mitigate human errors and accelerate the experimental process. Simplifying the experimental process also allows more attention to be directed at the patient/tissue of interest instead of worrying about mistakes that can occur in the 100's of performed actions, which can void the integrity of the particular experiment. This redirection of attention also provides a safer environment for the patient,

clinicians, and system operator.

The UI/UX is not limited to just software as the hardware design and implementation also plays an important role. Most research systems are designed to work in a laboratory environment and all the efforts are made to ensure the system behaves properly. However, little efforts are made to understand how the non-research end-user will use the system in the clinical translation step. Large bulky system that is difficult in transporting, maneuvering, and positioning will wear out the operator before the experiment is done. Meanwhile, poor ergonomics and lengthy preparations in the data acquisition process can pose as distraction for not just the researcher, but also all of the clinical personals'. Additionally, the ease of training new individuals of less technical background to run the data acquisition process is necessary for the DOCI project to be scalable. Lastly, safety considerations is mandatory in any clinical-related experiments as increasing complexity in both the system and procedure will introduce unwarranted hazards.

There are many hazards that needs to be considered such as mechanical integrity, electromagnetic interference, electrical integration with clinical electronics, optical radiation from UV exposure, and maintaining clinical sterility. While a comprehensive list can be drafted, design considerations that can provide simplicity should be emphasized for the long-term as complexity will only increase as new challenges get introduced. As previously discussed, improving upon various aspects of engineering and design of the system and process can mitigate problems.

The clinical workflow is the procedure of how the steps in the DOCI project intervenes with the existing clinical process and use the existing infrastructure to verify experimental results. There are many protocols and regulations in clinic that are necessary to ensure patient safety and accurate diagnosis. One of the major consideration is the amount of time on each of the stages during the clinical experimental process. These stages includes the system setup, patient setup, experiment duration, sample transportation, tissue sectioning, image registration, and data annotation. Improvements in systems operations were previous discussed in the clinical UI & UX design. The objective of improving existing clinical workflow process is to allow accelerated data curation process while maintaining data integrity.

2.3 Data Storage

After the data is collected, the methods of organizing and documenting large dataset is essential for both data access, data mining, and data analysis. While most research endeavors predetermine the number of sample size to determine statistical significance, medicine is an ever-changing environment where the phenotypes of patient population is highly heterogeneous and dynamic. Societal and habitual changes can also change research results as tissue fluorescence lifetime is highly dependent fluorophore ratios, temperature, pH, tissue oxygenation, etc... [44,45]. Furthermore each DOCI experiment provides hundreds of thousands of data points that can be utilized. Conventional statistical methods where predetermined sets of data point is no longer valid when data set is of this scale. Methods of quickly or autonomously accessing certain subsets of data is also necessary both from the workflow and analytical perspective as labeling and correlating data can be extremely time consuming; and methods to segregate data diversity in order to validate tissue response under different physiological conditions is needed to identify data heterogeneity. Therefore, software user interfaces are necessary for this entire process to work and optimization of this can further make the research more efficient.

2.4 Image Processing

The ability to provide accurate DOCI images can help with finding proper methods for image enhancement, better local features for motion correction, and provide improved results from unsupervised feature selection. Noise characterization from the system development process can improve all aspects of image processing by being able to remove specific types of noise with specific filters and regularization methods to further enhance images. Doing these tasks can enhance the data analysis by providing more accurate representations.

2.5 Data Analysis

For accurate data analysis to occur, the system characterization has to be robust, data storage and must be managed properly, and certain characteristics of image processing must be performed. If all the prerequisites are met, then pseudo-supervised features selection methods such as k-means or expectation-maximization (EM) can be used for clustering like-feature data together. This can reduce user selection bias and reduce the time needed to draw regions of interests (ROIs). The current DOCI system provides multi-spectral 1 megapixel (MPx) images. This means that when small ROIs are selected, each DOCI experiments can contain thousands of data points with 10 spectral features and even more statistical and image features. When the data is aggregated across dozens to hundreds of experiments, the size of the data would operate at hundreds of millions of data entries with dozens of features.

2.6 System Optimization

Lastly, once proper data analysis is performed, the next full iteration of the DOCI system can be made. This includes methods of reducing the number of data points or features needed via less filters by finding which filters are best at separating tissue types based on clinical applications or combining filters to increase signal-to-noise that are highly correlated. By doing this, the optics can be redesigned to use only a small subset of filters as oppose to the current set of 10 bandpass filters to optimize contrast between tissue types.

2.7 Conclusion

The DOCI project overview addresses many unsolved challenges in the current academic environment that is necessary for successful clinical translation of the system. Many time-consuming, but essential work such as data management, user interface, and user experience design provide little academic merit in the forms of academic publications. Development in these areas in addition to the core research system and clinical experiments have been demonstrated to provide an accelerated streamlined research process. Until a complete cycle

is achieved, it is difficult to quantify system performance or determine metrics to research progress. Once a full cycle is achieved, optimizing time and minimizing tasks will be essential for scaling the project towards clinical translation.

CHAPTER 3

Dynamic Optical Contrast Imaging (DOCI) - Theory & Model

DOCI is a technique that seeks to generate contrast from relative differences in fluorophore lifetimes without the need to compute absolute lifetime values. This eliminates the complex, computationally intensive data fitting routines that has prevented successful translation of using fluorescence lifetime properties to differentiate tissue types. The mathematics behind the ideal system is to utilize relatively long pulse widths (>20 ns) with short fall times (~ 1 ns) to produce contrast between fluorophores of different decay rates. Figure 3.1 shows how the DOCI method differs from conventional FLIM methods.

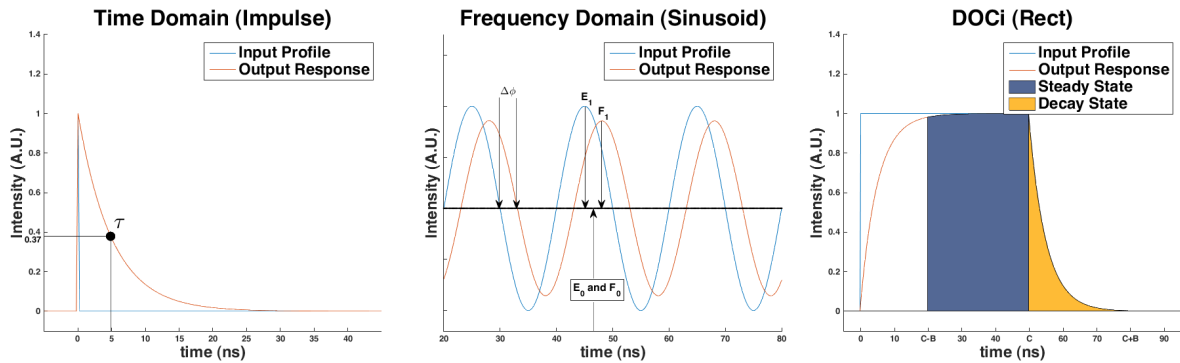


Figure 3.1: (left) Comparison between conventional time-domain method, (center) frequency domain method (center), and (right) DOCI method.

The DOCI system uses a rectangular illumination source and is modeled as a rectangular function. Unlike conventional FLIM methods where multiple data points at different time points are acquired, the DOCI method acquires two data points by integrating fluorescence signals at two specific time intervals - the steady state and the decay state. The steady

state is used as a reference peak intensity for normalization and the decay state represents fluorophores. Previous work have demonstrated the initial concept and promising human *ex vivo* pilot study image results have been demonstrated from the DOCI system [51, 52]. The aim of this work is to mathematically model the DOCI system through rigorous proofs to describe the contrast mechanism of the system and differentiate DOCI from existing fluorescence lifetime imaging methodologies. Several mathematical expressions have been formulated to describe the behavior of the DOCI system and how the contrast mechanism is interpreted. Non-ideal models and assumptions are also provided when the illumination source contains a first-order decay because the illumination source cannot be experimentally turned off instantaneously.

3.1 Idealized Model

In the idealized model, the fluorophore is treated as first order differential equations while the illumination source is set to be an ideal rectangular function. Eq. (3.1) reiterates the time-domain response for the first order differential equation as an exponential decay in which $f(t)$ is the decay response as a function of time. Variables a and A_0 will be used as intermediary variables to replace $\frac{1}{\tau}$ and i_0 respectively to simplify calculations.

$$f(t) = i_0 e^{-\frac{t}{\tau}} = A_0 e^{-at} \quad (3.1)$$

The DOCI rectangular excitation is modeled as the subtraction between a step function and a shifted step function as shown in Eq. (3.2), in which $h(t)$ is the rectangular excitation pulse as a function of time and C is the rectangular pulse width.

$$h(t) = u(t) - u(t - C) \quad (3.2)$$

Eq. (3.3) and Eq. (3.4) is the Laplace transform for the exponential decay and the rectangular pulse function respectively.

$$\mathcal{L}[f(t)] = F(s) = i_0 \left(\frac{1}{s + a} \right) \quad (3.3)$$

$$\mathcal{L}[h(t)] = H(s) = \frac{1}{s} - \frac{e^{-Cs}}{s} \quad (3.4)$$

These two equations will be the primary models to explain the DOCI system theory and how its contrast mechanism differentiates from the other methodologies.

3.1.1 Single Exponential Model

The general model of the DOCI system can be described as a finite integration of the convolution between the rectangular response and the hypothetical exponential sample decay as shown in Eq. (3.5).

$$q(t) = \int_0^t (f * h)(t) dt \quad (3.5)$$

In order to expand upon Eq. (3.5) and to not get confused with the convolution integral from the DOCI integral, the time-domain DOCI algorithm can be expanded into a double integral as shown in Eq. (3.6).

$$q(t) = \int_0^t \int_{-\infty}^{\infty} f(\tau) h(t - \tau) d\tau dt \quad (3.6)$$

Due to the complex nature of the equation in the time-domain, a closed form solution can be derived by defining the DOCI Laplace form $Q(s)$ in Eq. (3.7) and calculating the Laplace form of the DOCI method as shown in Eq. (3.8).

$$\mathcal{L}\{q(t)\} = \mathcal{L}\left\{ \int (f * h)(t) dt \right\} = Q(s) \quad (3.7)$$

$$Q(s) = \frac{F(s) \cdot H(s)}{s} = A_0 \left[\frac{1 - e^{-Cs}}{s^2(s + a)} \right] \quad (3.8)$$

Similarly, the time-domain DOCI ($q(t)$) can be redefined as the inverse Laplace transform as shown in Eq. (3.9).

$$\mathcal{L}^{-1}\{Q(s)\} = \mathcal{L}^{-1}\left\{ \frac{F(s) \cdot H(s)}{s} \right\} = q(t) \quad (3.9)$$

This allows the determination of the closed form time-domain DOCI that removes the previous double integral as in Eq. (3.10).

$$q(t) = \frac{A_0}{a^2} \left[e^{-at} - 1 + at - \left(e^{-a(t-C)} - 1 + a(t-C) \right) u(t-C) \right] \quad (3.10)$$

Figure 3.2 shows an example output of the computed model $q(t)$ with a 5ns decay with a 50ns pulse width(C) excitation. The derived closed form solution is compared with a discrete

convolution of between a rectangular function with an exponential decay with temporal increment of 0.25ns.

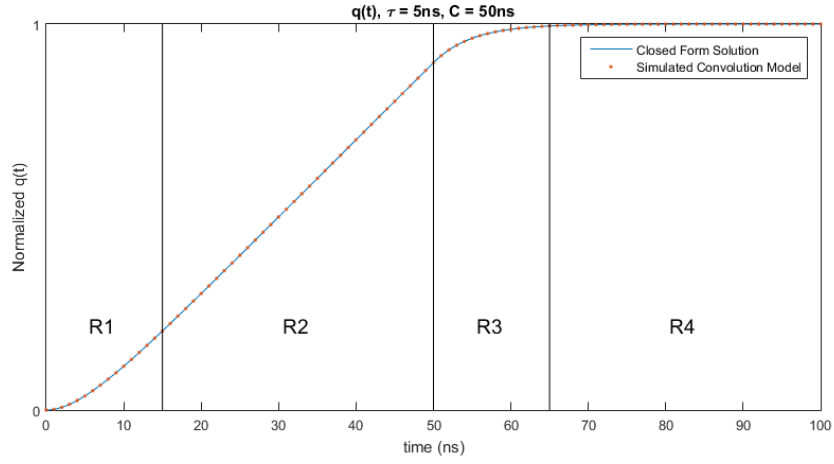


Figure 3.2: Comparison of the closed form solution and simulated convolution model for $q(t)$. The model is partitioned into four fluorescence states R1, R2, R3, and R4.

The two methods show identical results, which verifies the closed-form derivation. The model can be broken up into four distinct fluorescence states - R1, R2, R3, and R4, which corresponds to the fluorescence rise-time, steady state, decay state, and off-state respectively. The fluorescence steady-state and off-state can be approximated to be 3τ or 95% of the signal during the transient R1 and R3 regions respectively. However, this is not the complete DOCI method because the DOCI method integrates subregions of $q(t)$ as previously shown in figure 3.1 and a division between the integral of the decay state by the integral of the steady state. Eq. (3.11) shows the complete form of the ideal DOCI method in which C is the pulse-width of the rectangular illumination source and B is the integration time.

$$DOCI = \frac{Decay\ State}{Steady\ State} = \frac{q(C+B) - q(C)}{q(C) - q(C-B)} \quad (3.11)$$

The region $q(C+B)$ is the integral of the regions from $t=0$ to $t=C+B$ of $g(t)$ as previously shown in figure 3.1. Likewise, the region $q(C)$ is the integral of regions from $t=0$ to $t=C$. The integral of the decay region remains when $q(C)$ is subtracted from $q(C+B)$. The steady-state follows synonymous analogy, but happens before the decay state. Eq. (3.12) shows the

expanded form of the DOCI method for a sample following a single exponential.

$$\frac{q(C+B) - q(C)}{q(C) - q(C-B)} = \frac{A_0 \frac{1}{a^2} [1 + e^{-a(C+B)} - e^{-aB} - e^{-aC}]}{A_0 \frac{1}{a^2} [e^{-aC} - e^{-a(C-B)} + aB]} \quad (3.12)$$

Two assumptions are made to simplify this expanded form of the DOCI equation. Eq. (3.13) and Eq. (3.14) shows that the pulse-width must be much longer than integration time and the integration time must be much longer than the longest lifetime to be obtained respectively.

$$C \gg B \quad (3.13)$$

$$B \gg \tau \quad (3.14)$$

In the approximation, the pulse-width (C) should be at least 3x longer than the integration time (B) and the integration time (B) should be at least 3x longer than the longest fluorophore lifetime (τ) of interest. A reasonable upper bound lifetime is assumed to be 10ns. The exponential terms from the expanded DOCI equation can be approximated to be 0 with these assumptions as shown in Eq. (3.15), Eq. (3.16), and Eq. (3.17).

$$e^{-\frac{C}{\tau}} \rightarrow e^{-\frac{3B}{\tau}} = e^{-\frac{9\tau}{\tau}} \approx 0 \quad (3.15)$$

$$e^{-\frac{B}{\tau}} \rightarrow e^{-\frac{3\tau}{\tau}} = 0.050 \approx 0 \quad (3.16)$$

$$e^{-\frac{C+B}{\tau}} \rightarrow e^{-\frac{4B}{\tau}} = e^{-\frac{12\tau}{\tau}} \approx 0 \quad (3.17)$$

The exponential from Eq. (3.16) seems to be much greater than the rest of the other exponentials. However, due to possible system noise and fluctuations, 0.05 or 5% error margin seems to be a reasonable estimation. Eq. (3.18) provides the result simplified DOCI equation after all the exponential terms are approximated to be 0.

$$DOCI = \frac{A_0 \frac{1}{a^2} [1 + e^{-a(C+B)} - e^{-aB} - e^{-aC}]}{A_0 \frac{1}{a^2} [e^{-aC} - e^{-a(C-B)} + aB]} \approx \frac{A_0 \frac{1}{a^2}}{A_0 \frac{1}{a^2} aB} \quad (3.18)$$

Finally, a is converted back to $\frac{1}{\tau}$ to show the relationship of the DOCI equation with the fluorophore lifetime as shown in Eq. (3.19).

$$DOCI \approx \frac{A_0 \frac{1}{a^2}}{A_0 \frac{1}{a^2} aB} = \frac{1}{aB} = \frac{\tau}{B} \quad (3.19)$$

The extracted DOCI value is proportional to the lifetime with a scaling factor of inverse integration time. This mathematical derivation provides a generalized concept for the DOCI model applied to a single-exponential sample and validates previous related-works [49, 50]. However, previous work did not provide the analysis of the derived assumptions, which is essential for accurate and reproducible results, especially from system-to-system variations and long lifetime fluorophores.

3.1.2 Multi-exponential Model

Next, the DOCI model is presented in the case of multiple fluorophores of unknown concentration with varying fluorescence lifetime $\tau_0, \tau_1, \dots, \tau_n$, which is relevant for heterogeneous samples such as biological tissues. To aggregate multi-exponentials into the DOCI model, the previous a_0 and A_0 is redefined to a_i and A_i respectively. Eq. (3.20) shows a summation of multiple exponentials with different decay and fluorescence intensity.

$$f(t) = A_0 e^{-a_0 t} + A_1 e^{-a_1 t} + \dots + A_n e^{-a_n t} \quad (3.20)$$

The fluorescence intensity A_0 is dependent on several factors, including non-uniform illumination, quantity of present fluorophore, and respective fluorescence yield. A benefit of the DOCI method is that the division process enables normalization of these above mentioned non-uniformities. The illumination fluence is constant across all fluorophore constituents and can be divided out, as detailed below. The convolution theorem still applies, but the distributive property of convolution is applied to separate variables as shown in Eq. (3.21).

$$q(t) = \int_0^t (f_0 * h)(t) dt + \int_0^t (f_1 * h)(t) dt + \dots + \int_0^t (f_n * h)(t) dt \quad (3.21)$$

Similar to the single exponential model, Laplace transform is used to calculate the closed form solutions for each element i individually as shown in Eq. (3.22).

$$\int_0^t (f_i * h)(t) dt = \frac{A_i}{a_i^2} \left[e^{-a_i t} - 1 + a_i t - \left(e^{-a_i(t-C)} - 1 + a_i(t-C) \right) u(t-C) \right] \quad (3.22)$$

Likewise, the DOCI method from Eq. (3.11) and the assumptions made in Eq. (3.15), Eq. (3.16), and Eq. (3.17) is applied to the summation of multiple convolution integrals.

However, the terms have to be aggregated in the numerator and denominator independently. Only after the aggregation can terms between the numerator and denominator be canceled out. To reiterate, this is due to the system acquisition of the data in which only 2 frames are acquired independently with the DOCI system - the steady state and the decay state. Eq. (3.23) shows the resultant closed form solutions of the DOCI method for multiple lifetime decays.

$$\frac{\text{Decay State}}{\text{Steady State}} = \frac{q(C + B) - q(C)}{q(C) - q(C - B)} \approx \frac{A_0\tau_0^2 + A_1\tau_1^2 + \dots + A_n\tau_n^2}{B(A_0\tau_0 + A_1\tau_1 + \dots + A_n\tau_n)} \quad (3.23)$$

Eq. (3.24) shows a condensed summation version of the multi-exponential DOCI method.

$$\frac{A_0\tau_0^2 + A_1\tau_1^2 + \dots + A_n\tau_n^2}{B(A_0\tau_0 + A_1\tau_1 + \dots + A_n\tau_n)} = \frac{\sum_{i=0}^n A_i\tau_i^2}{B \sum_{i=0}^n A_i\tau_i} \quad (3.24)$$

This equation details the contrast mechanism of the DOCI system. The contrast visible from the pixels of the produced image is derived from different fluorophore yields, lifetimes, and augmented ratios. Furthermore, to decouple the non-uniform illumination from the rest of the detected fluorescence intensity, as shown in Eq. (3.25), where $\gamma(x, y)$ is the illumination profile as a function of space.

$$A_i = \gamma(x, y)A'_i \quad (3.25)$$

Unlike the single exponential where A_i is completely divided out, there are ratios that consists of the fluorescence yield and the fluorophore counts. The illumination profile from Eq. (3.26) is divided out and thus the DOCI system is resilient to non-uniform illumination in the ideal model (without considering signal to noise (SNR) of the system).

$$DOCI = \frac{\sum_{i=0}^n \gamma(x, y)A'_i\tau_i^2}{B \sum_{i=0}^n \gamma(x, y)A'_i\tau_i} = \frac{\cancel{\gamma(x, y)} \sum_{i=0}^n A'_i\tau_i^2}{\cancel{\gamma(x, y)} B \sum_{i=0}^n A'_i\tau_i} = \frac{\sum_{i=0}^n A'_i\tau_i^2}{B \sum_{i=0}^n A'_i\tau_i} \quad (3.26)$$

Although lifetime data can be decoupled from the illumination non-uniformity of the system, regions of dimmer illumination will produce result with worse SNR than regions that are well illuminated.

3.2 Model with Illumination Decay

Experimentally, it is difficult to generate an ideal rectangular excitation function as illumination sources can never turn on and off instantaneously. Furthermore, the DOCI method

to allow for rapid wide-field imaging utilizes light-emitting diodes (LED), which has a longer decay time relative to conventional pulsed laser sources. A DOCI model that factors in the illumination sources decay is proposed, where the source is also approximated to follow a first order differential equation decay similar to that of a simple mono-exponential fluorophore. The illumination source decay is modeled as shown in Eq. (3.27). Also similar to defining the constants in the fluorophore exponential, the variables in the decay from the excitation source such that the $\frac{1}{\tau_{exc}}$ is redefined to be d and that the $\gamma(x, y)$ from the multi-exponential non-uniform source is used to describe the maximum illumination intensity at a specific location in space. The intent is to demonstrate that the DOCI method is also insensitive to illumination profile heterogeneity so long as it is above a certain signal-to-noise threshold.

$$g(t) = \gamma(x, y)e^{\frac{-t}{\tau_{exc}}} = \gamma(x, y)e^{-dt} \quad (3.27)$$

Eq. (3.28) shows the Laplace transform of the LED decay, which is synonymous to a single lifetime decay.

$$\mathcal{L}[g(t)] = G(s) = \frac{\gamma(x, y)}{s + d} \quad (3.28)$$

Eq. (3.29) shows the LED illumination profile modeled as the convolution of the rectangular pulse. A model that better represent the empirical illumination pulse shape $h'(t)$ is the ideal pulse shape $h(t)$ convolved by the LED decay $g(t)$.

$$h'(t) = h(t) * g(t) \quad (3.29)$$

The fluorescence response over time is more precisely the convolution of the single exponential empirical illumination pulse shape $h'(t)$ with the fluorophore sample $f(t)$. Eq. (3.30) describes the DOCI system with the LED decay factored with sample fluorescence response through the associative property of convolution.

$$q(t) = \int_0^t (f * h * g)(t)dt = \int_0^t (f * h')(t)dt = q(t) = \int_0^t \int_{-\infty}^{\infty} f(\tau)h'(t - \tau)d\tau dt \quad (3.30)$$

This resultant equation is similar to that of Eq. (3.5), described previously in the ideal DOCI model. The closed form solution of this equation will be derived in the following sections also for both single and multiple exponential responses. In the current iteration of the

DOCI system, the illumination uses 375nm ultraviolet-A (UV-A) LEDs, so the illumination decay times ($\sim 4ns$) are comparable to biologic fluorescence decays so this factor cannot be neglected.

3.2.1 Single Exponential Model

Similar to the ideal DOCI derivation, the Laplace form of the DOCI method can be redefined in Eq. (3.31), which is the multiplication of the sample fluorescence decay $F(s)$, the rectangular pulse function $H(s)$, and the illumination decay function $G(s)$. Both a and d are the inverse lifetime decays of the sample and illumination respectively.

$$\mathcal{L}[q(t)] = \frac{F(s) \cdot H(s) \cdot G(s)}{s} = \gamma(x, y)A'_0 \left(\frac{1}{s^2(s+d)(s+a)} - \frac{e^{-Cs}}{s^2(s+d)(s+a)} \right) \quad (3.31)$$

The inverse Laplace transform from Eq. (3.31) is used to obtain the final time domain form of the 3-part convolution function shown in Eq. (3.32).

$$q(t) = \frac{\gamma(x, y)A'_0}{(d-a)} \left(\left[\frac{e^{-at} - 1 + at - (e^{-a(t-C)} - 1 + a(t-C))u(t-C)}{a^2} \right] - \left[\frac{e^{-dt} - 1 + dt - (e^{-d(t-C)} - 1 + d(t-C))u(t-C)}{d^2} \right] \right) \quad (3.32)$$

The constant $\frac{\gamma(x, y)A'_0}{(d-a)}$ is a function of the fluorescence yield, the illumination profile, and difference between the lifetime of the sample and the illumination decay. If the sample fluoresces longer than the time for the illumination to decay, the constant would be negative. At the same time, the subtraction between the two inverse squared terms will cancel out this negative constant. This is to demonstrate that the optical response $q(t)$ should never be negative, regardless of the combinations of illumination decay or sample fluorescence. If the decay for both the sample and illumination is the same ($a=d$), an equivalent alternative form is shown in Eq. (3.33) can be used.

$$q(t) = \frac{\gamma(x, y)A'_0}{d^3} \left(e^{-dt}(dt+2) - 2 + dt - \left[e^{-d(t-C)}(d(t-C)+2) - 2 + d(t-C) \right] u(t-C) \right) \quad (3.33)$$

Figure 3.3 shows the comparison of $q(t)$ between the models with and without illumination decay.

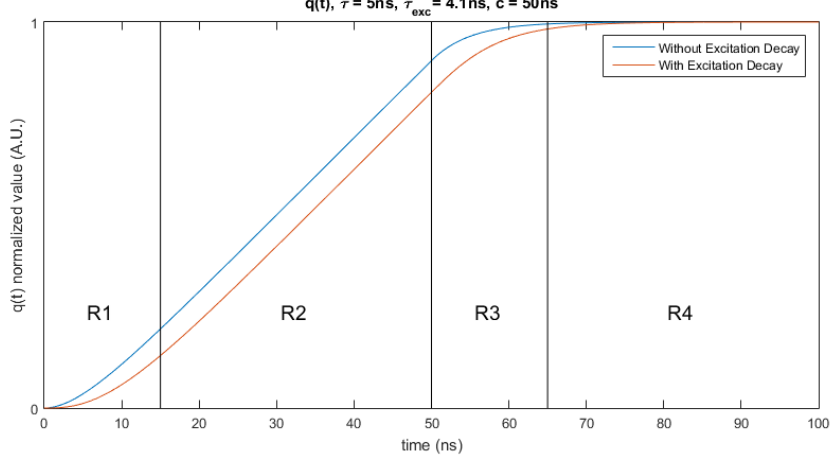


Figure 3.3: Comparison of $q(t)$ between with and without excitation decay. The model is also partitioned into four fluorescence states R1, R2, R3, and R4.

The primary difference when illumination decay is factored in is that it takes slightly longer for the fluorescence profile to reach steady state and off state compared to a ideal rectangular excitation pulse. Eq. (3.34) shows the resultant expanded form when the DOCI method is applied.

$$\frac{\text{Decay State}}{\text{Steady State}} = \frac{\frac{\gamma(x,y)A'_0}{(d-a)} \left[\frac{1}{a^2} \left(1 + e^{-a(C+B)} - e^{-aC} - e^{-aB} \right) - \frac{1}{d^2} \left(1 + e^{-d(C+B)} - e^{-dC} - e^{-dB} \right) \right]}{\frac{\gamma(x,y)A'_0}{(d-a)} \left[\frac{1}{a^2} \left(e^{-aC} - e^{-a(C-B)} + aB \right) - \frac{1}{d^2} \left(e^{-dC} - e^{-d(C-B)} + dB \right) \right]} \quad (3.34)$$

The common constant $\frac{\gamma(x,y)A'_0}{(d-a)}$ can still be divided out, which reaffirms that the ideal DOCI method is insensitive to non-uniform illumination when signal-to-noise is not considered. However, a new fractional ratio terms of $\frac{1}{a^2}$, $\frac{1}{d^2}$ is introduced that was nonexistent in the previous models. This requires using the assumptions previously defined in Eq. (3.15), Eq. (3.16), and Eq. (3.17) to be qualified so that all the exponential terms can be approximated to be ~ 0 . Variable β is defined in Eq. (3.35) to be the summation of the dominant exponential terms and requires the DOCI system parameter selection so that the summation of these terms are less than or equal to 0.05 in order to approximate these terms to be 0.

$$\beta = \frac{e^{-aB}}{a^2} + \frac{e^{-dB}}{d^2} \leq 0.050 \approx 0 \quad (3.35)$$

These two terms are the dominant exponential terms that remains when selecting the DOCI

system parameters as previously shown in Eq. (3.15), Eq. (3.16), and Eq. (3.17). The solution is to increase the integration time to be longer than the original 3τ . The length of the increase would depend on the decay of the illumination source and longest fluorophore lifetime of interest. This allows all of the exponential terms to be approximated as 0 and simplifies the DOCI model to be Eq. (3.36) after change of variables from a and d to $\frac{1}{\tau}$ and $\frac{1}{\tau_{exc}}$ respectively.

$$DOCI \text{ value} = \frac{\text{Decay State}}{\text{Steady State}} \approx \frac{\frac{\gamma(x,y)A_0}{(\frac{1}{\tau_{exc}} - \frac{1}{\tau})}(\tau^2 - \tau_{exc}^2)}{\frac{\gamma(x,y)A_0}{(\frac{1}{\tau_{exc}} - \frac{1}{\tau})}[B(\tau - \tau_{exc})]} = \frac{\tau + \tau_{exc}}{B} \quad (3.36)$$

When all terms are simplified, the DOCI value for the single exponential decay model is a function of the illumination decay time and the sample lifetimes divided by the integration time. The final equation simplifies down to a relatively intuitive model even with the double convolution that was introduced with the original mode. Figure 3.4 shows a simulated lifetime vs DOCI value of the derived linear model and the effects if β does not remain less than 0.05.

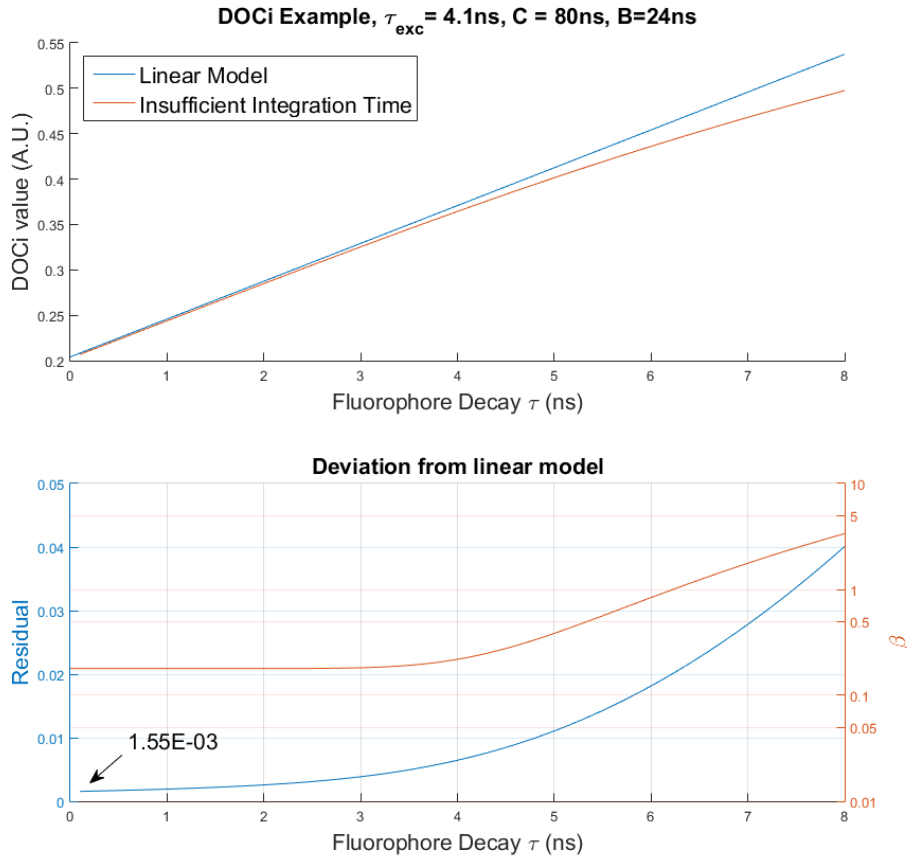


Figure 3.4: (*top*) Simulated linear decay model vs model with insufficient integration time. (*bottom*) Residual error deviation from linear model and β constant factor amongst different decay times

Parameters that were used in the following example includes a 4.1ns illumination decay time, 80ns pulse-width and a 24ns integration time. Under these conditions, the residual error differences between the linear model and the derived model for lifetimes less than 5ns have $\sim 1\%$ error. The β starts increasing exponentially after 5ns, which results in the deviation from the linear model to also start increasing exponentially. For a hypothetical 8ns fluorophore sample, which acts as upper bound for biological fluorophores, have errors approximate to be about $\sim 5\%$ of the linear DOCI model. Although this error deviation on the order of $\sim 5\%$ is relatively small, this error may be amplified when introducing other system-related noise. A solution to reduce this deviation would be to increase the integration

time (B), which will allow the error to be reduced to less than 1% as shown in figure 3.5.

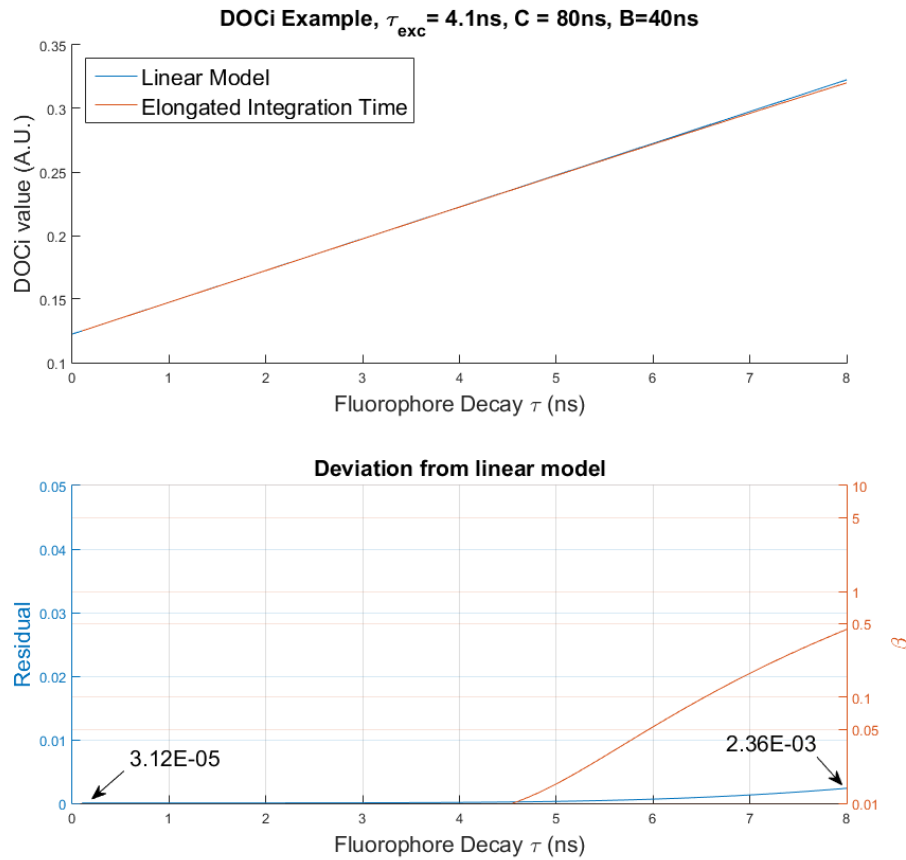


Figure 3.5: (*top*) Simulated linear decay model vs model with sufficient integration time. (*bottom*) Residual error deviation from linear model and β constant factor amongst different decay times

When the integration time is changed from 24ns to 40ns, the non-simplified model matches much more closely to the simplified linear model than the previous simulation. The residual is also 2 orders of magnitude less for short lifetime decays. At 8ns decay, deviation from the linear model occurs at $<1\%$. In addition to better correlation with the intuitive linear model, increasing the integration time also maximizes the contrast between short and long lifetimes as well as potentially increasing signal-to-noise ratio. This single exponential model with illumination decay has similarity with its previous counterpart where $\gamma(x, y)$ can be divided out. This reaffirms that the DOCi value is independent of the illumination profile

so long as SNR is high enough that noise is negligible. The terms A'_0, A'_1, \dots, A'_n remain since they cannot be canceled out due to their ratio-like characteristics.

3.2.2 Multi-exponential Model

This section continues the derivation of the DOCI method with the illumination decay for multi-exponential fluorescence decays. From the previous section, Eq. (3.36) is derived to be the simplified form for single exponentials. For multi-exponentials, this equation can be generalized for each unique fluorophore as an index (i) as shown in Eq. (3.37).

$$\frac{\text{Decay State}_i}{\text{Steady State}_i} \approx \frac{\frac{\gamma(x,y)A'_i}{(\frac{1}{\tau_{exc}} - \frac{1}{\tau_i})}(\tau_i^2 - \tau_{exc}^2)}{\frac{\gamma(x,y)A'_i}{(\frac{1}{\tau_{exc}} - \frac{1}{\tau_i})}[B(\tau_i - \tau_{exc})]} = \frac{\gamma(x,y)A'_i\tau_i\tau_{exc}(\tau_i + \tau_{exc})}{B\gamma(x,y)A'_i\tau_i\tau_{exc}} \quad (3.37)$$

This generalized form of the equation prior to division between the numerator and the denominator can then be expressed into a summation form for multi-exponential decays as shown in Eq. (3.38).

$$\frac{\text{Decay State}}{\text{Steady State}} \approx \frac{\sum_{i=0}^n \gamma(x,y)A'_i\tau_i\tau_{exc}(\tau_i + \tau_{exc})}{B \sum_{i=0}^n \gamma(x,y)A'_i\tau_i\tau_{exc}} = \frac{\sum_{i=0}^n A'_i\tau_i(\tau_i + \tau_{exc})}{B \sum_{i=0}^n A'_i\tau_i} \quad (3.38)$$

The illumination profile $\gamma(x, y)$ and τ_{exc} are common terms across all of the summed exponentials, which allows it to be simplified from the entire summation term. This final term is very similar to Eq. (3.24) that was previously derived for the ideal multi-exponential model, but with one of the τ_i term being replaced by $\tau_i + \tau_{exc}$.

Empirically, the illumination source used exhibits a 4-5ns decay, which is substantial considering that biological fluorophores under investigation have lifetimes between 1-10ns. Under conditions where the sample lifetime is much greater than the illumination decay time (*e.g* $\tau_i \gg \tau_{exc}$), then the τ_{exc} can be assumed 0 and would reduce the equation back down to the ideal multi-exponential case. This final ratio equation permits a quantitative interpretation of the contrast mechanism given that certain assumptions hold. Initial pilot study's goal was to be able to identify different tissue types through relative DOCI value. However, as multiple systems were developed where each system were slightly different, a more robust and quantitative approach is needed to enable cross-platform data amalgamation and system standardization.

3.3 System Noise

Brief explanation of the system noise can be incorporated into the ideal model as this is still a work in progress. The decay state and the steady state signal that are acquired from the DOCI system are termed $Signal_{DS}$ and $Signal_{SS}$, respectively. The two signals that are acquired from the DOCI system are a composition of the true fluorescence signal and the background signal as shown in Eq. (3.39). To extract the true fluorescence signal, the background signal must be subtracted out before applying the division, as shown in Eq. (3.40).

$$\frac{Signal_{DS}}{Signal_{SS}} = \frac{Decay\ State + BG}{Steady\ State + BG} \quad (3.39)$$

$$\frac{Decay\ State}{Steady\ State} = \frac{Signal_{DS} - BG}{Signal_{SS} - BG} \quad (3.40)$$

Sources of noise in the DOCI system that can be empirically measured includes the detector background noise and the illumination flux. The noises sources are assumed to be Poisson distributed. Additionally, the DOCI method allows for $>5\text{KHz}$ data acquisition rate, so as the sample size approach large values, the Poisson distribution can be approximate to follow a normal distribution. In a well-controlled in-vitro lab environment, the illumination flux per unit area can be accurately measured. However, this becomes difficult to reproduce in a clinical environment where there is high variations in imaging focal distances and object contours. There are also sources of noise from the sample because of its biochemical heterogeneity, dynamic chemical states (e.g. temperature, pH, oxygenation, hydration, etc..), and intermolecular interactions (quenching, bleaching, etc..) [44, 45]. These are more difficult, if not impossible to measure or identify in fresh tissue because the physiologic dynamics prohibit repeatability. These measurements are also not clinically relevant as the goal is to identify the average signal distribution of tissue A from tissue B. Eq. (3.41) shows a model for the noise distribution.

$$\frac{Signal_{DS} - BG}{Signal_{SS} - BG} \sim \frac{\mathcal{N}(\mu_{Signal_{DS}}, \sigma_{Signal_{DS}}) - \mathcal{N}(\mu_{BG}, \sigma_{BG})}{\mathcal{N}(\mu_{Signal_{SS}}, \sigma_{Signal_{SS}}) - \mathcal{N}(\mu_{BG}, \sigma_{BG})} = \frac{\mu_{DS} \pm \sigma_{DS}}{\mu_{SS} \pm \sigma_{SS}} \quad (3.41)$$

By propagation of uncertainty, the signal distribution of the decay state and steady state can be approximated separately as shown in shown in Eq. (3.42) and Eq. (3.43) respectively.

$$\mu_{DS} \pm \sigma_{DS}^2 = \mu_{Signal_{DS}} - \mu_{BG} \pm \sigma_{Signal_{DS}}^2 + \sigma_{BG}^2 + 2cov(DS, BG) \quad (3.42)$$

$$\mu_{SS} \pm \sigma_{SS}^2 = \mu_{Signal_{SS}} - \mu_{BG} \pm \sigma_{Signal_{SS}}^2 + \sigma_{BG}^2 + 2cov(SS, BG) \quad (3.43)$$

When the two distributions are divided together, the DOCI signal distribution can be approximate as shown in Eq. (3.44).

$$DOCI = \frac{\mu_{DS} \pm \sigma_{DS}^2}{\mu_{SS} \pm \sigma_{SS}^2} = \frac{\mu_{DS}}{\mu_{SS}} \pm \frac{\sigma_{DS}^2}{\mu_{DS}} + \frac{\sigma_{SS}^2}{\mu_{SS}} - 2 \frac{cov(DS, SS)}{\mu_{DS}\mu_{SS}} \quad (3.44)$$

The final form of the DOCI signal-to-noise distribution contains multiples ratio occurrences of the standard deviation from the steady state signal, decay state signal, and background. This equation can also be applied pixel to each pixel independently due to the method's insensitivity to illumination non-uniformity. Maximizing the signal or minimizing system noise has direct impact to the resolvable lifetime resolution.

3.4 Discussion

A single system was prototyped to demonstrate algorithm feasibility and clinical translatability in previous works. However, there are several challenges that exist in the development of the DOCI system such as creating a stable illumination source and system noise characterization. The primary limitation that results from these challenges is that the work reported to date use a relative system-specific models for device performances and data interpretation. This makes it difficult for massive data accumulation across heterogeneous tissues with many physiological confounding variables using multiple systems.

The derivation of the closed-loop model under different system and operating conditions allows for greater understanding of the effects of different subsystem variables on the DOCI data such as the illumination decay and system noise. This rigorous mathematical derivation allows for quantitative imaging as oppose to relative system-specific imaging. More focused simulations and models can be independently developed for system characterization and improvement in data accuracy.

3.5 Conclusion

DOCI generates image contrast through relative measurements of the autofluorescence decay rates (*lifetime*) of aggregate fluorophores in tissue. The mechanism of this tool is non-invasive and does not require special dye or injection of exogenous contrast agents. This technique quantifies measurements of intrinsic fluorescence lifetime ratios unique to tissue types and permits display of additional information that is not available to the unaided eye. It is superior to other fluorescence measuring approaches because the computation of absolute lifetime values is not required in this approach.

The simplicity of the data processing permits high-speed visualization of regions of interest suitable for translation into the clinic or the operating room. The presented derivation and results support ongoing efforts of adapting the algorithm to provide a useful tool for real-time intraoperative guidance. This novel tool warrants further investigation through large-scale clinical trial and engineering development in order to successfully expand the armamentarium of medical devices available to the physician.

CHAPTER 4

System Implementation

This chapter will provide the DOCI system implementations that was developed and system specifications.

4.1 System Overview

Figure 4.1 provides a system diagram of the DOCI system and how each of the major components are controlled.

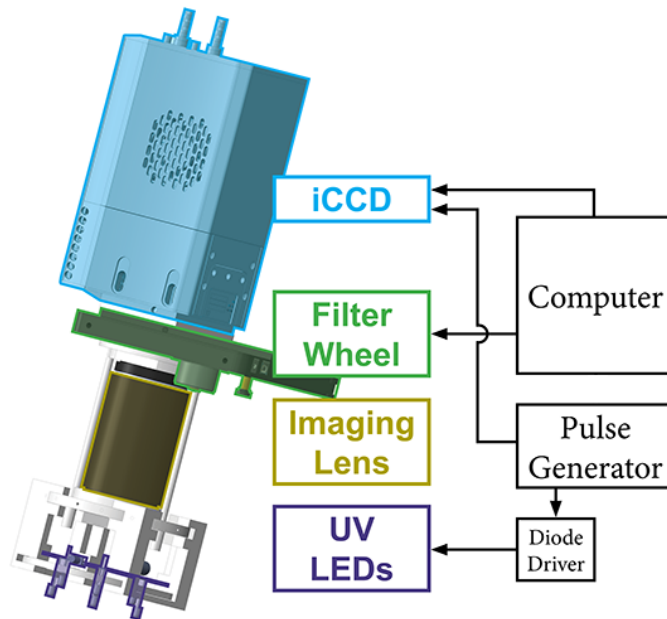


Figure 4.1: DOCI system diagram.

The major components of the DOCI system includes an intensified charged coupled device (iCCD), filter wheel, imaging lens, illumination source, computer, and a pulse generator. The

computer is used to synchronize the control the iCCD and the filter wheel, while the pulse generator is used to synchronize the acquisition timing of the iCCD and the illumination pulses of the illumination source. Figure 4.2 shows the multiple iterations of the DOCI system that was developed.

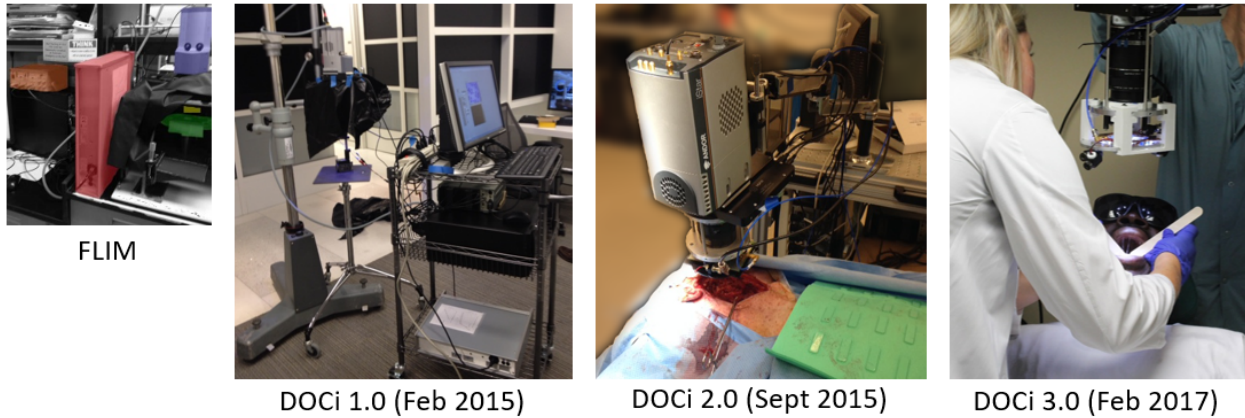


Figure 4.2: Different iterations of the DOCI system implementation.

The pre-DOCI fluorescence lifetime imaging microscopy (FLIM) system was an *ex vivo* imaging system used for imaging most of the *ex vivo* data set. The system stability and imaging environment were well controlled so variations amongst experiments were minimized. DOCI 1.0 was the first rapid-prototyped systems for *in vivo* imaging. There were many problems with this iteration, but most notably the multiple modules for transporting the system and the mechanical design for operating the system. The multiple modules required the system to be assembled and disassembled after every experiment for transportation. The wheels on the modules caused difficulty in transporting the systems across asphalt and small crevasse such as moving on and off elevators. The surgical microscope arm that was used for mounting the DOCI camera was also difficult to maneuver and required repositioning the patient instead of repositioning the system.

DOCI 2.0 was designed to address the logistical problems with transportation and system operations from DOCI 1.0. A custom cart was built so that all the components could be fixed and transported on a single module. Large air cushioned tread wheels were used to allow easier transportation of the system across rough terrains, but reduced the stability of fine

motions when focusing the camera onto specific regions on the patient. Only the primary power outlet from an electrical transformer was needed to be plugged and unplugged between experiments. An Ergotron LX monitor arm with 25lb weight rating was used to mount the imaging contraption to allow flexible maneuverability of the imaging module. The problem with this monitor arm was that the range was not long enough to fully reach across the entire surgical bed and the height was slightly low such that the surgical bed always had to be constantly oriented into the lowest possible position. The imaging lens allows for *in vivo* imaging of surfaces, but cannot be used to image deeper cavities. Focusing onto a targeted location was also difficult as the screen was fixated on the cart and aligning the camera required the user to be in ergonomically challenging positions. Lastly, the most difficult challenge was mass producing illumination source that can deliver reproducible illumination pulse profile. This is especially important because the illumination source is being driven in unconventional conditions.

DOCI 3.0 was designed to address many of the issues mentioned in version 2.0, such as the illumination and ergonomics. Circuit boards were designed for scalable fabrication and multiple boards were tested to determine performance reproducibility. Additional red targeting lasers were incorporated to allow for laser-guided focusing as oppose to being in ergonomically difficult positions to guide the camera. Longer Humanscale M8 monitor arms with 40lb rating was used to allow for longer range of motion and was fixed on an elevated platform tailored for normal surgical bed height. Longer focal length lens were used to allow for further and safer working distance. Incorporation of APC Smart-UPS 1500VA uninterruptible power supply (UPS) allows for protection of electronic equipment in the operating room to prevent power trips that can cause potential equipment and data damage by forced desktop and iCCD shutdown. This also allowed the system to be standalone usage without needing to be plugged into the wall, which causes tripping hazard in the OR. Some issues with this iterations again also includes cart wheel selection, in which harder D80 plastic urethane wheels were selected to allow stability in the OR environment. However, the extra hard wheels results in vibration during transportation on asphalts, which leads to loosening of fasteners and reduced mechanical integrity of the system. Future iteration of the system

should use softer wheels with of durometer of $\sim 80A$ hardness with shock absorption, which is a balance between DOCI 2.0 and 3.0 to reduce this hazard. Other issues includes the imaging arm being heavier and the center of mass gravitating away from the handle, which requires increased torque to maneuver the system. The illumination source, has always been at the center of the bottleneck in each system iteration. Longer focal and working distance leads to the the optical power both from illumination and fluorescence to fall off distance squared, thus effectively reducing signal-to-noise of images taken.

4.2 Optics

The optical components of the DOCI system includes the multiple optical bandpass filters used to acquire fluorescence at specific wavelengths, imaging lens, and the Andor iCCD. The optical bandpass filters are used for creating spectroscopic fluorescence lifetime tissue contrast and will be further explained in the section 4.3. Three different imaging lens were used for each iteration of the DOCI system, each with different trade-offs summarized in table 4.1.

Imaging Lens	Field of View	Working Distance	Resolution	Signal-to-Noise
Canon MP-E 65mm f/2.8 1-5X Macro Lens	-	-	++	++
Canon EF-S 18-55mm f/3.5-5.6 IS II SLR Lens	+	+	+	+
Canon EF-S 55-250mm F4-5.6 IS STM Lens	++	++	-	-

Table 4.1: Trade-off of different imaging lens.

In the *ex vivo* FLIM and DOCI 1.0 system, Canon MP-E 65mm lens was used. This lens offered best magnification/resolution and signal-to-noise, but has a very small field of view and working distance. This lens is best used when the sample can be finely positioned at a very close proximity. However, once the system was translated for *in vivo* use, the existing working distance became impractical and the small field of view made it very difficult to

identify accurate regions to image. Additionally, when motion of the patient and clinicians are introduced into the system, it is common that the targeted tissue becomes misaligned. The DOCI 2.0 system used the Canon EF-S 18-55mm lens, which offered increased field of view and working distance. However, when the illumination circuit is incorporated into the system, the clearing distance falls short and can be a clinical safety hazard. DOCI 3.0 readdresses this issue with the Canon EF-S 55-250mm lens, which allows for a large focus distance range. While the distance can be very far away, the trade-off is reduced signal-to-noise and reduced resolution. This in turn becomes a major problem as signal falls off distance squared both in the illumination and fluorescence direction.

The last primary optical component is the detector. The selection of using the Andor iCCD compared to other brands and models was carefully selected to optimize cost, performance, and control precision [46]. The specific detector criteria that is needed to obtain results using the DOCI method requires sub-nanosecond timing precision for both temporal offset delay and detector optical gate width. Furthermore, endogenous tissue typically have low autofluorescence yield, so a high quantum efficiency detector is needed to obtain enough signal to maximize signal-to-noise. Figure 4.3 shows the quantum efficiency (QE) of the two generations of Andor camera.

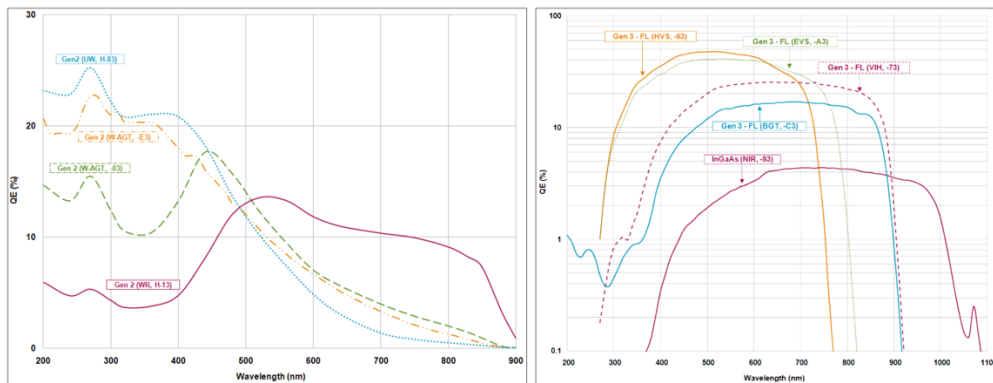


Figure 4.3: Camera quantum efficiency specifications. (*left*) Generation 2 detector and (*right*) generation 3 detector provided by Andor.

Three different models of Andor iCCD were used for developing each of the DOCI versions. In FLIM and DOCI 1.0 system, the Andor iStar DH734 Gen 2(W-AGT,-03) was

selected because it had the highest QE in the visible spectrum in the second generation systems. Third generation camera became available for the DOCI 2.0 and the Andor USB iStar 334T Gen 3 - FL (VIH,-73) was selected as it had high QE of $\sim 20\%$ and slightly extends to near-infrared (NIR). In DOCI 3.0, Andor USB iStar 334T Gen 3 - FL (EV3,-A3) was selected to have even greater QE of $\sim 40\%$, but sacrificing spectral data beyond 800nm.

4.3 Contrast Mechanism

Every tissue has different biochemical compositions and every biochemical fluorophore have unique spectroscopic signatures. The DOCI system uses multi-spectral optical bandpass filters as a method to distinguish ratios of these spectroscopic features. Figure 4.4 shows the optical bandpass filters spectra and major biological fluorophore fluorescence spectrum.

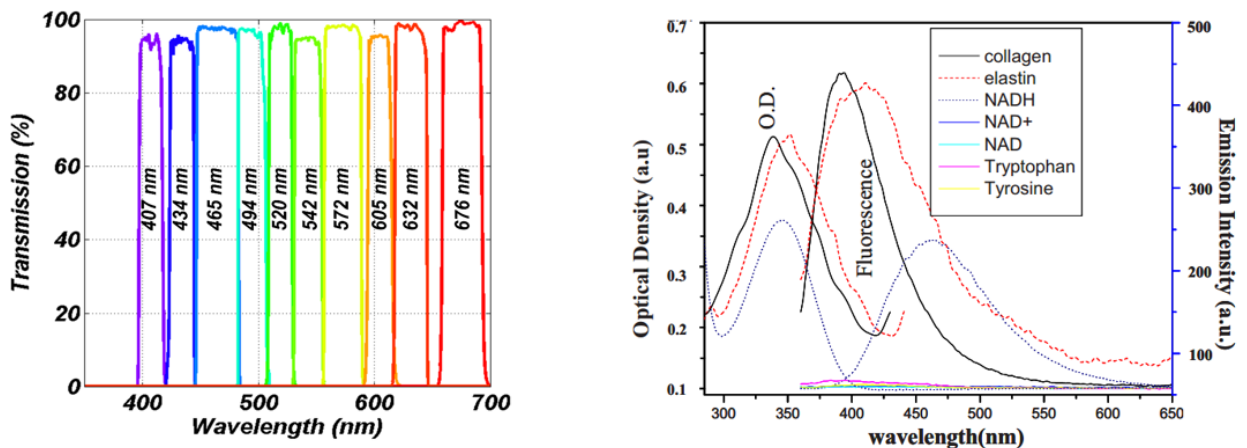


Figure 4.4: (*left*) Optical bandpass filter spectra [1] and (*right*) major biological fluorophore absorption and fluorescence spectrum [2].

Each of the optical bandpass filter were selected from Semrock. Each filter offered $>90\%$ transmission, optical density (O.D) $\sim 6-7$ rejection, and has a spectral bandwidth of $\sim 20-30\text{nm}$ resolution. Each of the selected wavelengths allows different fluorescence signal weighting, which translates to providing different fluorophore weighting amongst collagen, elastin, and NADH as these are the primary fluorophore. Shorter wavelengths(400-430nm) will provide large weighting to collagen and elastin, but very little towards NADH; intermediary

wavelengths (430-480nm) weights elastin more; and longer wavelengths (450nm-700nm) provide more similar emphasis on elastin and NADH while reducing collagen contribution. All three of these primary fluorophore have peak absorption at \sim 340-360nm, which is the motivation for using 370nm illumination source. This spectroscopic fluorescence information provides an additional layer of specificity to differentiate tissues in addition to selecting excitation sources and calculating the ratiometric fluorescence lifetime characteristics using the DOCI method.

4.4 Electronics

The electronics of the DOCI system consists of two major components - a pulse generator and the illumination source. The pulse generator generates rectangular electrical pulses at a high voltage (50-100V) to drive the illumination circuit and has an internal trigger used to synchronize with the camera. In FLIM and DOCI 1.0 system, the Avtech, AVR-E2-C pulse generator with analog dials was used. One of the problems with this pulse generator is the difficulty to accurately control the device especially when the dials are accidentally changed. In DOCI 2.0 and 3.0 system, digital models of pulse generator Avtech, AVR-E3-B-P was used in which settings are digitally adjusted and has built in settings memory. The digital pulse generator has capability to be synchronized with the computer to allow the settings to be controlled via software and programmable, but this feature was not implemented.

The illumination source is the only key component in the DOCI system that requires custom fabrication and has been the component that is the most difficult to produce. The key specifications that is necessary in the illumination circuit for an ideal DOCI system is the emission of a rectangular optical pulse response at high optical intensities. The optical response from circuit used in the FLIM, DOCI 1.0, and DOCI 2.0 was not reproducible as it used low quality perforated printed circuit board (PCB) and resistors that do not operate in high frequencies. In DOCI 3.0, this issue was addressed by creating a circuit CAD file using FR-4 PCB and surface mounted components. This allows for stable supply of circuit boards to be in place and allow for the illumination circuit to be more standardized than

a handcrafted board. Figure 4.5 shows the circuit diagram of the DOCI 3.0 illumination circuit.

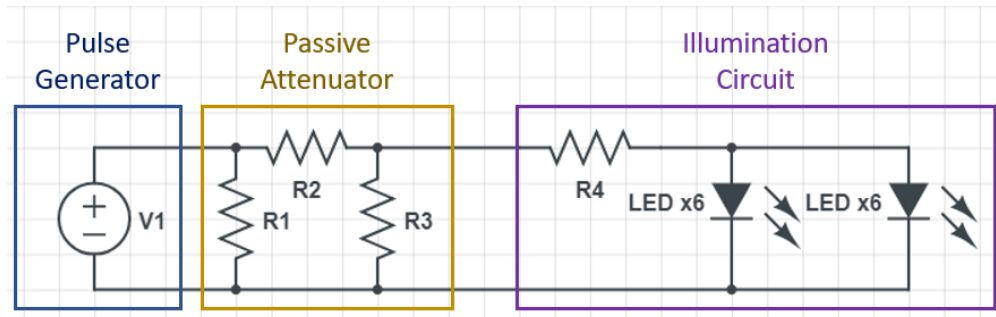


Figure 4.5: DOCI illumination circuit diagram.

The illumination circuit can be broken up into two parts in addition to the pulse generator - a passive attenuator and the illumination circuit. In previous circuit iteration, a stub-tuner line was used instead of the passive attenuator. One problem with the sub-tuner line is that it has to be individually tuned based on individual circuit response. In a multi-system environment, the need to individually make adjustments would be difficult to provide metrics to standardize the system. The addition of the MiniCircuits VAT-1+ 1DB passive attenuator was a component that allowed a path to ground for reflected radiofrequency pulses to prevent the accumulation of destructive interference while maintaining the present impedance response. The attenuator is designed as a simple pi-pad (Π -pad) resistor formation. The illumination circuit includes a resistor that tries to match the line to be 50Ω and two parallel paths of a series of Thorlabs LED370E - 375 nm Epoxy-Encased light-emitting diode (LED), 2.5 mW, T-1 3/4. This specific diagram shows two parallel paths of six LEDs. Earlier iterations of the DOCI system utilized two lines of three LEDs and also six LEDs in series on a single line. The trade-off is the turn-on voltage that is necessary to turn the LEDs on and optimizing for maximum illumination intensity that is within maximum permissible exposure range. Figure 4.6 shows the optical response created by this illumination circuit.

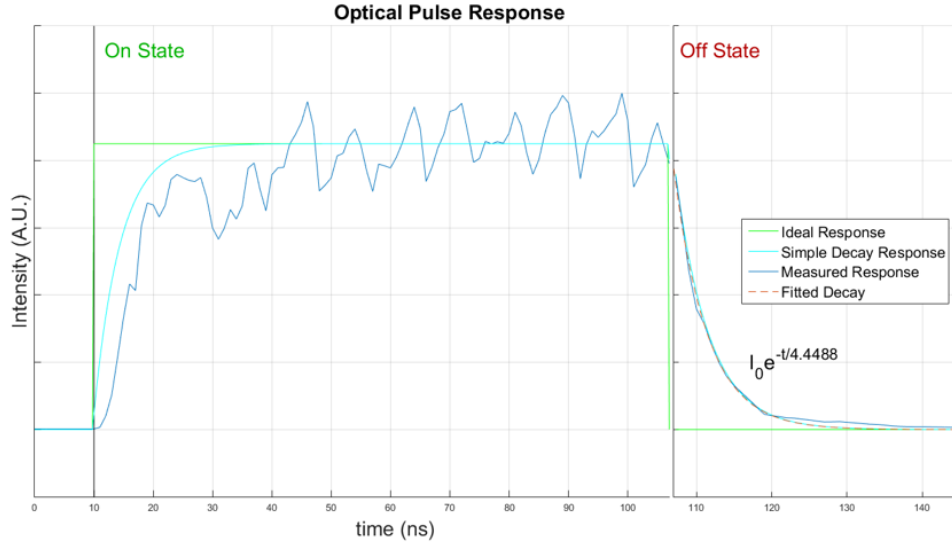


Figure 4.6: Comparison of measured and modeled DOCI illumination profile.

This figure compares the different pulse profile for the DOCI system. Ideally, the DOCI system should have a perfect rectangular pulse in order to simplify the mathematics as previously derived models. However, the operating conditions of LEDs in an ultra-short high power setting used in the DOCI system is unconventional. There is also no documentation of component behavior operating in these conditions. It is also known that LEDs operate in lower frequency ranges compared to pulsed lasers and that sub-nanosecond turn-off is difficult. This led to developing the illumination model that includes the simple decay response model. The mathematical derivation of the effects of this decay to the DOCI contrast mechanism is also described in previous sections. The actual measured optical response of the circuit seems highly correlated with the simple decay response model, but has a notable oscillation in the steady state. The decay state is highly correlated with the actual decay model extracted by fitting an exponential decay curve to the measured decay response. Qualitatively, the peaks and troughs of the oscillation cancel each other out when the DOCI integrates these regions, which is a trade-off that was acceptable in order to consistently mass-produce circuits with similar pulse profile. Identifying methods to reduce this oscillation and further increasing the optical power is a work in progress. Computational models to factor in noise or variations to optical profile is on a need basis, which is dependent

on the results from circuit behavior.

4.5 Discussion

There are many hardware components of the DOCI system that can be improved upon. Starting from the Andor cameras, there are major limitations in the form factor in which each camera weights 9-12lbs in a 4.4in x 1.9in x 2.0in. Some reasons for this form factor may be that the camera contains sub-nanosecond timing electronics and modules to cool the detector down to -40°C . The physical form limits the types of form factors that the DOCI system can be designed because large bulky cameras limit the system to be mounted on large mechanical arms. Some other limitation includes the ADC rate as it is one factor that determines the image refresh rate of the DOCI system. The current Andor USB iStar 334T Gen 3 has a 5MHz ADC rate, meaning it would take 0.2s to transfer a 1-megapixel image from the camera to the desktop. Three images are taken using the DOCI method - a steady state, decay state, and a hidden background state is taken. This means that without considering for signal-to-noise and exposure time of each image, the minimum refresh rate is limited to 0.6s/frame or $<2\text{Hz}$. The refresh rate and signal-to-noise could be improved by down-sampling and signal binning, but the cost is the sacrifice of image resolution. Real-time hand-held form factor would require either multi-mode flexible fiber optics bundling or improvements in the performance and form factor of the camera.

To optimize the specifications of the objective lens design, a specific clinical application needs to be first defined. Then, a consensus amongst affiliated clinicians of safe working distance needs to be agreed upon. The mechanical structure of the illumination circuit and the imaging optics would need to be designed to fulfill the clearing distance at the distal portion of the imaging module. By identifying these parameters, the imaging optics of the DOCI system can be optimized to maximize signal-to-noise and operational safety. Additionally, the sets of band-pass filters should not be changed until enough quality data is collected to allow for accurate machine learning and statistical techniques to be used to determine which spectroscopic parameters are best or worst for specific clinical applications.

The decision for adding, removing, or combining filters would be data-driven and not be from qualitative speculation.

The most essential of the system where off-the-shelf system that is not readily available is the illumination source. Illumination sources that operates is the required DOCI specifications has been a challenge. LEDs were first used due to their low-cost compared to laser source equivalent, but this low-cost is offset by the high cost of the pulse generator. There are also many safety hazards using UV lasers in the clinical setting, which requires all clinical personals to wear additional protection. The optical power of the illumination source should also be maximized to allow for best signal-to-noise quality images as biological fluorophores have low fluorescent yield. Current State of California Department of Industrial Relations title 8, chapter 4, subchapter 4, article 34, section 1801 - nonionizing radiation have safety power rating at $1\text{mW}/\text{cm}^2$. The FLIM, DOCI 1.0, and DOCI 2.0 used the same circuit that operated at $20\mu\text{W}/\text{cm}^2$, which means the current illumination can be amplified by over 40x and still be within the maximum permissible exposure. However, the peak power will also substantially increase and the effects would need to be studied. The LEDs in DOCI 3.0 system are driven by the pulse generator near its maximum power range, but the signal-to-noise of the images were sometimes not enough to resolve the images. Under these circumstances, the optical power density of DOCI 3.0 was not measured because the signal-to-noise of these image are already very poor. Active matching circuits using capacitive components are currently being tested but is beyond the scope of this thesis.

CHAPTER 5

Calibration

This chapter provide a method for calibrating the DOCI system using a few selected fluorescent dyes. This is essential for system standardization, multi-system data aggregation, and data reproducibility. There are currently several DOCI systems each with different cameras and illuminations circuits producing differing results. Proper system standardization should correct for these differences by translating unitless DOCI value image to quantitative lifetime or lifetime ratio values. To accomplish this, the dyes were measured using both conventional time-domain FLIM method and the DOCI method. Multiple lifetime data points extracted from several fluorescent dyes were then correlated with the DOCI method. The final objective is to develop a fluorescence lifetime-DOCI (FL-DOCI) curve for every unique system.

5.1 Methods & Materials

5.1.1 Calibration Dye Selection Criteria & Preparation

There are several references containing single-exponential lifetime data of dyes [45,54,57–59]. However, the current DOCI system for biological imaging uses excitation wavelength at 375nm and the biological fluorophores of interest such as collagen, elastin, reduced nicotinamide adenine dinucleotide (NADH), oxidised flavins, lipofuscin, keratin, and porphyrins have emissions in the visible spectrum with typical lifetimes of 1-10ns [47]. In order to develop a calibration method for current active clinical DOCI research systems, non-toxic dyes that exhibit properties closely related to the working conditions was selected for rapid translation and verification. The theoretical model has been developed and empirical results are

needed to verify the models. Fluorophores that exhibit stable mono-exponential decays are preferred, but a few dyes that are less stable were also used as representation of instability that is normal in biological fluorophores.

Fluorescein (*Sigma-Aldrich 46970-100G-F*) and Rhodamine 6G (*Exciton Rhodamine 590 - 05902 tetrafluoroborate*) dyes were selected as stable calibration dyes that have been well characterized in literature, but have limited range of decays (1-4ns). Perylene (*Sigma-Aldrich P11204-1G*) and 9,10-Diphenylanthracene (DPA) (*Sigma-Aldrich D205001-1G-A*) dyes were selected to expand the lifetime decay ranges (4-8ns) beyond Fluorescein and Rhodamine 6G at the cost of stability and increasing complexity [54, 60–63]. Fluorescein and Rhodamine 6G were dissolved in deionized water at concentrations 100 μ g/mL and 200 μ g/mL respectively, and is the preferred solvent for measurement. Perylene and DPA are insoluble in water, and both were dissolved in cyclohexane at concentrations of \sim 1.5mg/mL. A note in the preparation for Perylene and DPA dyes is that the mixtures were prepared in ambient atmospheric air. This introduces gas impurities into the mixture, specifically oxygen; which has been shown to quench fluorescence and lifetimes of aromatic hydrocarbons in cyclohexane solutions [45, 60, 61]. Each of the dye samples were placed in UV-fused quartz cuvettes (*Thorlabs CV10Q700FS*) to allow transmission in the ultraviolet and visible spectrum.

5.1.2 Time-Domain FLIM Characterization Method

The time-domain FLIM setup uses a nitrogen pulsed laser (*PTILasers FL2300*) with pulse characteristics of 1.2ns full-width half-maximum and 337nm central wavelength. The laser pulse was characterized using a photodetector (*Thorlabs DET025AL*) with an oscilloscope (*Teledyne LeCroy WaveSurfer 3074*). Although the nitrogen laser has nominal specifications of 0.7ns pulse width, the detector and oscilloscope used was not able to detect such high frequencies. This issue is negligible using an iterative convolution fitting algorithm. Figure 5.1 displays a system diagram of the FLIM system.



Figure 5.1: Time-domain FLIM dye calibration system setup that consists of the nitrogen laser, dye sample, optical filter, and photodetector.

Two measurements are needed to extract the lifetime of dye samples as previously shown in equation 1.3. First, the extraction of the input pulse $h(t)$ and second, the measurement of the fluorescence response $g(t)$. The extraction of the laser pulse $h(t)$ is acquired by directly illuminating the laser pulse at the photodetector without saturating the maximum voltage range. Next, the dye sample decay $g(t)$ is acquired by placing the dye in the path of the laser with a 450nm long-pass filter (*Thorlabs FEL0450*) between the dye and photodetector. This allows only the fluorescence signal to be acquired while removing signals from the laser. The dye samples were oriented to allow maximum surface area exposure for excitation and fluorescence emission.

5.1.3 Time-Domain FLIM Data Analysis

After the laser profile $h(t)$ and fluorescence response $g(t)$ of each dye samples were measured, the fluorescence lifetimes were extracted by using an optimization function as shown in equation 5.1.

$$error_{min} = \min (|g(t) - h(t) * i_0 e^{-t/\tau}|) \quad (5.1)$$

The concept is to minimize the error by subtracting the measured result by a computed model that is derived from the input pulse convolved by a range of ideal exponential decay, with an error associated with each decay model. The assumption that was made is that the

dye samples follow a mono-exponential decay. The lifetime extraction of the dyes is obtained by selecting the exponential decay model that has the minimum the error. Algorithm 1 was implemented in *MATLAB* to compare a generative model with the measured data.

Algorithm 1 Iterative lifetime extraction algorithm

```

1: dye : Fluorescence Lifetime Dye Data
2: pulse : Laser Data
3: error : Error Array
4: for  $\tau=0$ , steps=.01, end=10 do
5:   decay : Exponential Decay using  $\tau$ 
6:   model = pulse * decay
7:   Align & normalize peaks of dye, pulse, model
8:   dye = first decay subregion of dye
9:   model = first decay subregion of model
10:  residual = sum(dye - model)2
11:  error $\tau$  = residual
12: end for
13: Guessed Lifetime = argmin(error)

```

The pulse and dye measurements are acquired using methods described in section 5.1.2. The error variable is introduced to store the minimum residual value provided by iterating through an array of possible lifetimes of the dye. Following these variable declaration, an iterative process in the form of a forloop, is used to guess & determine lifetimes ranging from 0ns to 10ns with increments of 0.01ns. The guessed model is generated by convolving the guessed lifetime decay by the measured excitation pulse. The peaks between the measured fluorescence pulse with the model are aligned and normalized before finding the residual between the two curves. A subregion window is selected from the first pulse and exponential decay before the second oscillation spike. The residual for each lifetime is saved and the lifetime that is determined to be closest to the measured is the one with the smallest residual error.

The measurement process includes 5 sets of laser measurements and 5 sets of fluorescence measurements for each dye. This would allow 25 different permutations of laser and dye measurements that can be used to extract the lifetime. A distribution of extracted fluorescence lifetimes from multiple measurements can be used to acquired a mean and standard deviation. Figure 5.2 shows the visual comparison of one forloop iteration from the algorithm that compares the measured laser profile, measured dye fluorescence, and fitted predicted model.

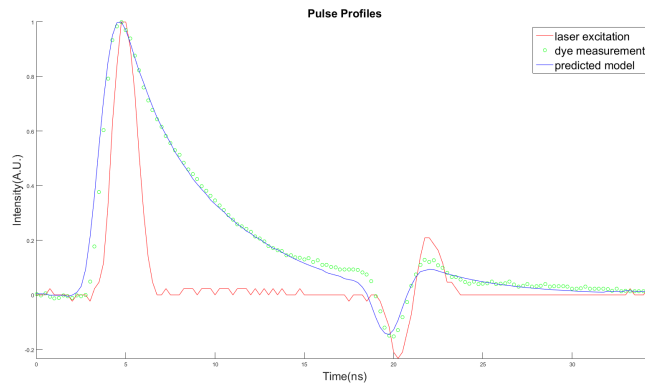


Figure 5.2: Intensity profile for excitation laser pulse, dye fluorescence measurements, and fitted predicted model.

This process is relatively time consuming because this doesn't have a closed-form solution and requires iterating through an array of possible lifetimes. The advantage of using this approach compared to other method is that fluorescence lifetime can be extracted without substantial preprocessing or system noise characterization. This method also does not require determining initial conditions and performing complex discrete deconvolution computations.

5.1.4 DOCI Characterization Method

After the dyes were characterized using conventional time-domain FLIM method, the dyes were measured using DOCI dye calibration setup as shown in figure 5.3.

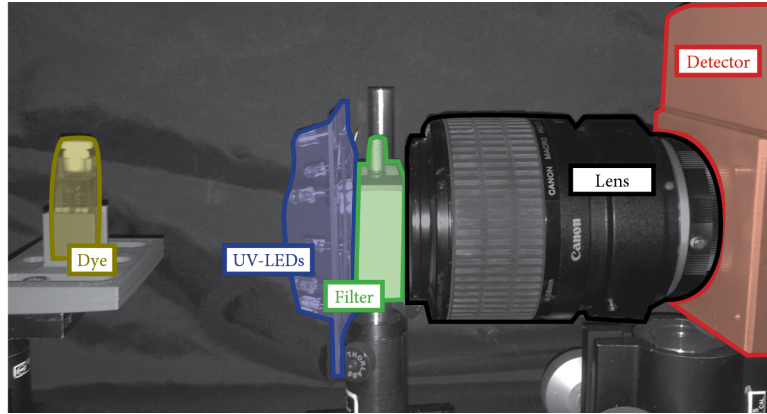


Figure 5.3: DOCI dye calibration system setup that consists of UV-LEDs, dye sample, optical filter, imaging lens, and detector.

The filters and dyes used in the DOCI experiment was same as that in the time-domain FLIM method. The UV-LED illumination circuit is similar to the circuit diagram shown in figure 4.5, but two parallel sets of three LEDs in series were used instead. The older Andor iStar DH734 Gen 2(W-AGT,-03) was used in this experiment because ADC rate and QE specifications has little effect on the results for phantom studies that have high fluorescence yields. The Canon MP-E 65mm f/2.8 1-5X Macro Len was used to maximize signal-to-noise and working distance is not an issue in this experiment. Lastly, the Avtech, AVR-E3-B-P digital pulse generator was used to allow for the settings and experiments to be reproducible. Prior to imaging the dyes, the optical pulse profile of the LED was obtained by acquiring a time sequenced data using kinetic series acquisition mode with the iCCD in 1ns step-sizes. The dull surface of an aluminum foil was used as the imaging target as it has extremely high isotropic reflectance characteristics in the UV-A range [64]. Figure 5.4 shows the optical response created by this illumination circuit with aluminum foil as the target.

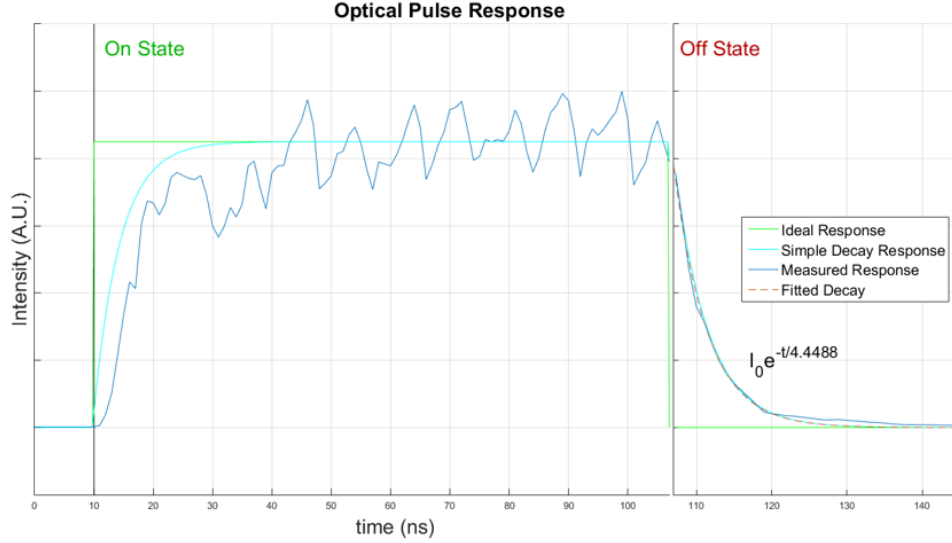


Figure 5.4: Comparison of measured and modeled DOCI illumination profile.

This circuit has a ~ 4.45 ns decay behavior with a remarkable periodic oscillation in the on state. The pulse generator had settings of 40 kHz duty cycle as this was the maximum repetition rate that generation 2 Andor iCCD camera could handle, 40 ns delay, 90 ns pulse-width, and 45 V electrical output. The camera was set to have 1.5 ns gate width for each step and 1 ns step size. The exposure time is negligible so long as the background noise fluctuation before and after the pulse is small because the intensity is normalized to the peak values.

Given this specific optical pulse profile, the camera settings that were used for collecting the steady state and decay state DOCI data is 40 ns integration bin with 68 ns delay and 40 ns step size. This means the area underneath the 68 ns-108 ns would represent the steady state signal and 108 ns-148 ns would represent the decay signal. An additional background set of DOCI data using the same parameter was obtained, but with the lens covered. Similar to the data sets acquired in the time-domain FLIM experiment, five sets of steady state and decay state images were obtained from each of the dyes and five sets of background DOCI images were also obtained. This also allows for 25 permutations of DOCI image results to be obtained.

5.1.5 DOCI Data Analysis

The data analysis for the DOCI method is much simpler than the FLIM method as it only requires simple arithmetic. Eq. (5.2) shows the arithmetic used to extract the DOCI data from the images.

$$DOCI\ image_{dye,i,j} = \frac{Decay\ State_{dye,i} - Decay\ State_{BG,j}}{Steady\ State_{dye,i} - Steady\ State_{BG,j}} \quad (5.2)$$

The *ith* and *jth* annotation represents the five sets of dye and background images respectively, which results in the 25 data permutation per dye. The result is a DOCI image, which is the 1MPx image obtained from the camera. The arithmetic subtraction and division of images are computed on an individual pixel basis. A subregion of the final DOCI image is selected because only a fraction of the image contains the dye results. This subregion across all 25 permutation were then obtained to create a histogram with >10,000 data entries per dye. The mean and standard deviation amongst the 10,000's of data points was also computed.

5.1.6 DOCI Computational Modeling

In addition to the empirical results from both the time-domain FLIM and DOCI methods, a computational model that uses the DOCI illumination data was also developed to determine if dyes were necessary to calibrate each system. The purpose is to determine whether the DOCI system can be calibrated solely from the illumination pulse profile of the system without the need for using calibration dye samples. It is also very difficult to prepare a wide range of dyes across multiple lifetimes that have low operational hazards. If the computational model is able to correlate with the empirical DOCI results, then this could be a potential alternative used to calibrate each system. This is important because there is many uncertainties with the illumination source due to its unique operating conditions. If the computational modeling calibration work, then future methods to automatically calibration the system after each usage would be possible. This is critical step that is needed until the product cycle of the illumination circuit becomes well characterized, which has been the major challenge in the DOCI project.

The DOCI computational modeling uses empirical data from the illumination pulse profile and modeled exponential decays to simulate the FL-DOCI curve. Eq.(5.3) and Eq.(5.4) shows the mathematical approach to generate the simulated curve.

$$\text{Simulated Fluorescence}(t, \tau) = (\text{Measured Optical Profile}(t) - \text{Background}(t)) * e^{-t/\tau} \quad (5.3)$$

$$\text{Simulated DOCI Value}(\tau) = \frac{\text{Area}(\text{Simulated Fluorescence}(108 - 148, \tau))}{\text{Area}(\text{Simulated Fluorescence}(68 - 108, \tau))} \quad (5.4)$$

Fluorescence lifetime(τ) between 1-10ns in 0.01ns increments were used to compute the simulated fluorescence response as a function of time. The 1-10ns range is selected to represent relevant fluorophores for clinical applications. The simulated fluorescence response was computed by convolving the exponential decay by the measured optical profile of the illumination circuit after subtracting by the detectors background signal. Then, for every simulated fluorescence response, the area under the curve is computed for the steady state and decay state. In this experiment, the steady state and decay state is from 68ns-108ns and 108ns-148ns respectively as previously mentioned in the empirical DOCI measurement experiment. The area is computed using trapezoidal approximation in MATLAB. The computed area of the decay state is divided by the steady state to obtain the simulated DOCI value for each exponential decay.

5.2 Results

Figure 5.5 shows the empirical dye sample results obtained from both the time-domain FLIM method and the DOCI method.

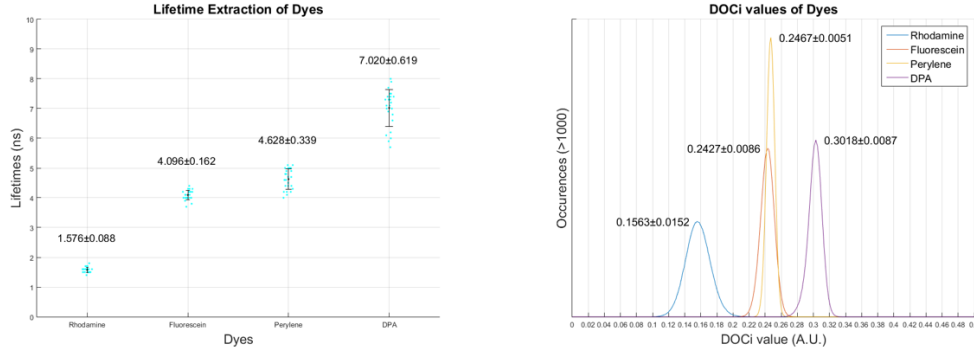


Figure 5.5: (*left*) Time-domain FLIM and (*right*) DOCI method results for each calibration dyes.

From the time-domain FLIM method, the fluorescence lifetime results for Rhodamine and Fluorescein correlates with literature values and has low standard deviation [45, 54, 59]. On the contrary, Perylene and DPA resulted in much lower fluorescence lifetime values compared with literature and has a high standard deviation [54, 61, 62]. This result was expected because the dyes were not made in an oxygen-sealed chamber and oxygen is a known fluorescence quencher in these two particular dyes, which also resulted in the fluorescence lifetime values to also be more susceptible to fluctuations. Fluorescein and Perylene resulted in much closer lifetime than expected. The order of the DOCI results correlates with the increasing lifetime measured using the time-domain FLIM. However, the histogram distribution of each dye is slightly different than the error distribution in the measured lifetimes. One explanation is the signal-to-noise of the dyes when the DOCI method was performed. The fluorescence of Rhodamine under the DOCI illumination was very weak compared to all the other dyes while Perylene exhibited the greatest fluorescence intensity. Figure 5.6 combines the empirical data and compares the results with the simulated calibration result.

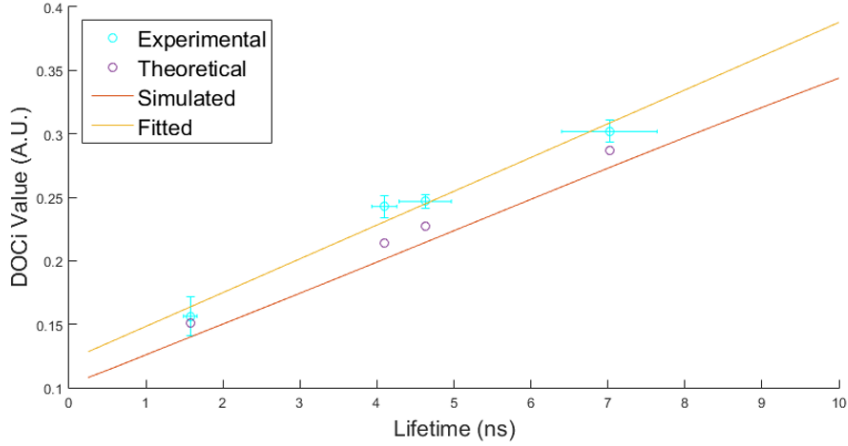


Figure 5.6: Fluorescence lifetime-DOCI curve that compares the experimental results, simulated results, fitted empirical results, and theoretical model.

The comparison between all of the methods show an interesting correlation in which the slopes from each method are highly correlated. The four data points obtained from the theoretical model was single exponential model with LED decay using Eq. (3.36). The τ_{exc} used to compute the DOCI value was ~ 4.5 ns because this was the extracted LED illumination decay. The τ used was the fluorescence lifetimes extracted from each of the dye samples from the time-domain FLIM method. The integration time (B) was set as 40ns because this was the constant used to control the camera integration in the DOCI method and the integration time used in the computational model for determining the area under the steady state and decay state. Although the curves from each of the methods shows a linear trend at similar slopes, there is a noticeable difference in the offsets. One hypothesis to this difference is the periodic fluctuation in the LED illumination source. All of the models that were developed for the DOCI method does not incorporate the effects of the oscillation. It is also complicated to create a generalized model for specific oscillation.

5.3 Discussion

Prior to this experiment, the DOCI method was based upon relative contrast imaging with no metrics to standardize systems. This is especially problematic when scaling to multiple

systems and providing quantitative reproducible results. This calibration experiment demonstrates that it is possible to relate experimental results with theoretical models. The results from each of the proposed methods and models show high linear correlation between single exponential fluorescence lifetime with DOCI value. However, there are still discrepancies in the ranges in each method. This may be due to several confounding factors, but the primary ones would be the imperfection in the illumination circuit and the lack of signal-to-noise characterization in various aspects of the system. However, once these issues are resolved, it is possible that the resulting FL-DOCI curve experimental, computational, and theoretical can have substantially reduced errors. Once the accuracies amongst the methods are improved, the unitless DOCI values can be better mapped to fluorescence lifetime values. For more complicated heterogeneous samples, the DOCI value would represent the area of aggregate fluorophore fluorescence lifetime ratios that is mapped to an equivalent DOCI value of some single exponential sample.

CHAPTER 6

Clinical Data Acquisition

This chapter will discuss the procedures and tools developed to assist in the clinical data acquisition and the progression over time. One of the goals is to redistribute work or train several individuals to perform certain tasks while maintaining integrity of the research. Such goals were accomplished by creating automation tools, streamlining experimental procedures, and developing several software interfaces with the intent to minimize training and explanations. All of this time minimization is essential for any project if the research is to be scalable for large clinical trials. Every minute saved during an experiment equates to thousands of minutes saved if the research project is to be widely adapted. Every task reduction that requires human intervention is a reduction to probabilistic human error. All of these optimizations were considered while evaluating the time-cost trade-off of developing tools for the clinical data acquisition process.

6.1 Software Automation Tools

One of the first few tools that were developed for the DOCI project is standardizing parameters and automating as much as the data acquisition process as possible. In the beginning, the data acquisition process was using end-user software developed by Andor and Optec for controlling the DOCI camera and filter wheel respectively. Figure 6.1 shows the initial DOCI user interface for running an experiment.

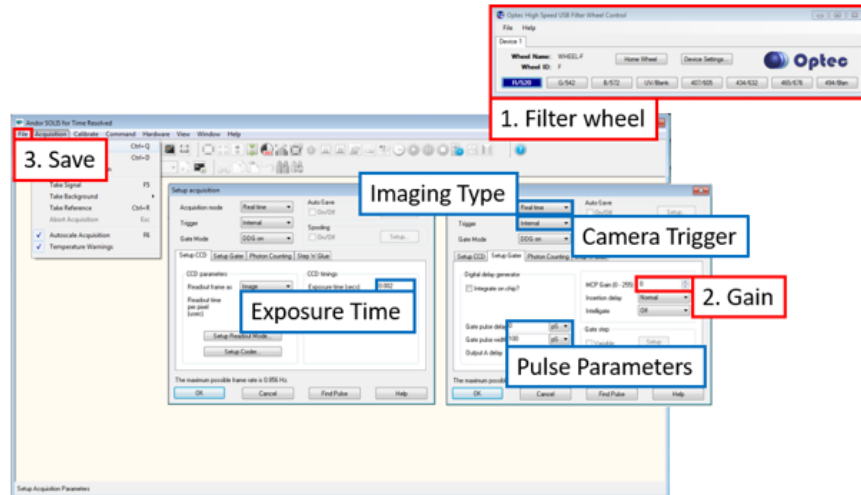


Figure 6.1: Initial software user interface provided by Andor and Optec.

In this user interface, blue highlighted box shows parameters that needs to be changed when alternating between brightfield video imaging for focusing the sample, brightfield RGB composite imaging, and DOCI fluorescence decay imaging. These parameters include the imaging type, which requires alternating between single image and kinetic series; camera trigger, which requires alternating between external and internal triggering; exposure time, which varies from 0.1s for the brightfield imaging to 5-10s for fluorescence decay imaging; and pulse parameters, which for brightfield is the entire exposure time with non-specific delay and specific pulse width integration binning at specific time points for the DOCI decay image. Next, there is the red highlighted box that shows parameters that needs to be changed for every single image frame, with a minor exception for the camera gain setting. For each of the brightfield images, the filter wheel needs to be switched amongst red, green, and blue filters at 0 detector gain. After each of the images, the user must name and save each of the images that are acquired. For each of the multi-spectral optical bandpass filter fluorescence decay images, the gain and filter needs to be changed. The user almost must manually name and save each of the images that each filter acquired. A filter wheel swap is also necessary due to the implementation of the filter wheel that only allows for eight filters to be mounted. Three filters are used to create the RGB composite image while ten optical bandpass filters are used to generate the multi-spectral fluorescence decay images.

Overall, there are hundreds of tasks that needs to be done for each experiment. If any one of these tasks were forgotten or parameters were accidentally set wrong, then the image set for the experiment would be incomplete and would be difficult to identify the errors unless the image seems obviously out of place. Furthermore, if all of this was done without any errors, the process still would have taken between 20-40 minute to complete. Under these circumstances, the DOCI project be difficult to scale to thousands of patients. Large amount of experiments would have incomplete dataset and the system would not be clinically translatable because each experiment would take too long. To address this issue, a software interface was developed in LABVIEW that automates most of these process as shown in figure 6.2.

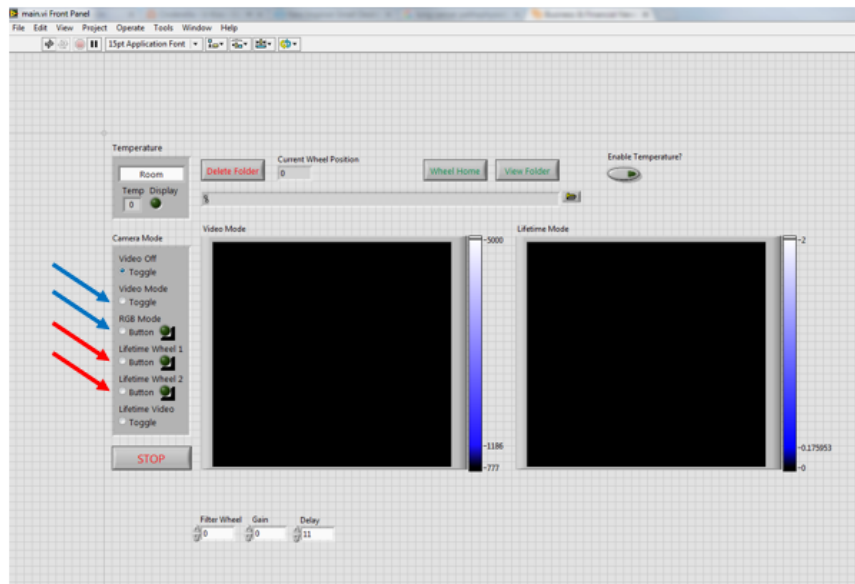


Figure 6.2: Software interface developed in LABVIEW to provide automation features.

The primary feature of the GUI is to allow for the DOCI experiments to be completed with four button clicks and a filter wheel swap. The blue arrows represents the buttons for brightfield imaging while the red arrows represent buttons for the DOCI fluorescence decay imaging. The blue arrows consists of video mode, which switches the filter to a UV longpass filter to allow maximum signal for focusing on the tissue; and RGB mode, which takes a brightfield image after each filter wheel swap for red, green, and blue filter. The

folders are created automatically and are date/time stamped to ensure folders created are unique. However, this may not be true in the future if multiple systems are to be used simultaneously. The files are automatically saved and are named based on the filter, hour, minute, and second that the image was taken on. The fluorescence decay images is split into two buttons in which each button controls a separate filter wheel. By implementing these automation features, the DOCI experiment time is reduced from 20-40min down to 2min, in which the rate limiting step that prevents even faster data acquisition is signal-to-noise, which determines the exposure time; and the analog-digital-converter of the camera, which determines the minimum amount of time for the camera to transfer data to the computer. This implementation accelerated a part of the research process by 10-20x and also makes the research system clinically translatable for *in vivo* patient imaging.

6.2 Experimental Procedure

There are many challenges with developing a clinical process to allow accurate data to be collected and be registered with existing gold standard. Two processes have been developed to attempt to correlate DOCI data with histopathology, but there are still challenges that exist to allow accurate image correlation.

6.2.1 Human *ex vivo*

The first method for processing tissue sections and histology was exclusively for *ex vivo* tissue specimen and the process is shown in figure 6.3.

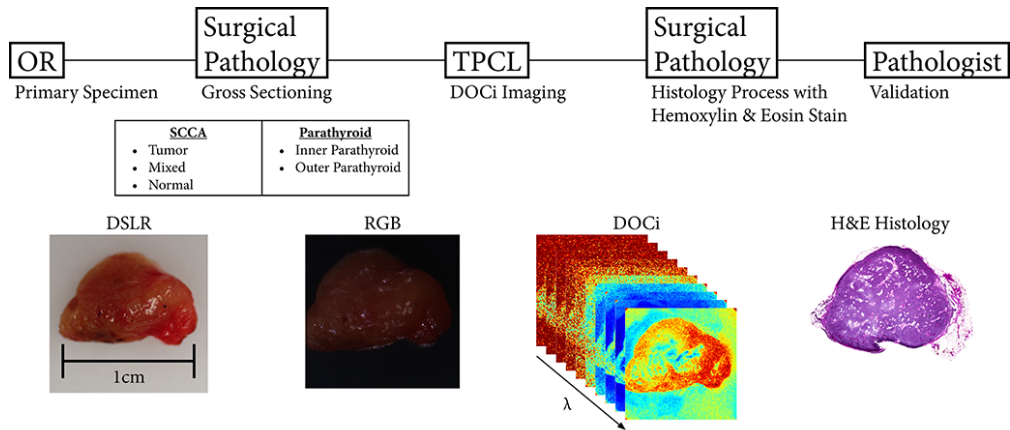


Figure 6.3: Human *ex vivo* clinical experimental procedure.

The tissue sample starts out being resected in the operating room (OR) as a primary specimen. The sample is then delivered to surgical pathology for pathologist assistants to perform gross sectioning of the tissue. Depending on whether the tissue is for squamous cell carcinoma (SCCA) or parathyroid experiment, different types of tissue sections will be obtained. For the SCCA experiments, three tissue sections are often obtained such that they consists of pure normal, pure tumor, and the boundaries that have a mix of both. The initial reason for obtaining three different sections is to have a ground truth normal data, ground truth tumor data, and the behavior of the margins. However, it is difficult for pathologists & pathology assistants to consistently provide accurate gross sections. For parathyroid experiments, the tissues that are obtained are usually bivalved such that data from the inner parathyroid and outer parathyroid can be obtained. Inner parathyroid data will provide the ground truth of parathyroid signal while outer parathyroid data represents what is clinically significant in surgery as this would be the images that would assist surgeons in parathyroid localization.

After the tissue sections have been obtained, they are delivered to Translational Pathology Core Lab (TPCL); where the DOCI imaging experiments are performed. During the DOCI experiment process, three distinct images are obtained - a digital single-lens reflex (DSLR) image, which shows high resolution color images that clinicians typically see during surgery; a RGB composite image, which is color image reconstruction from three color filtered image

obtained by the Andor scientific camera used for DOCI imaging; and a stack of multi-wavelength DOCI images, which measures the fluorescence decay properties of the tissue at specific optical wavelengths using optical bandpass filters.

After the imaging experiments are performed, the tissue samples are oriented such that the peripheral contours of the histology slides match that of the DOCI images. The gold standard Hematoxylin and Eosin (H&E) stain is performed on the tissue slices to allow for accurate differentiation between cell types [65,66]. After the histopathology results are obtained, validation of the DOCI results with histology is necessary by scheduling a time with a pathologist, a surgeon, and the engineer/researcher.

Issues arise during the histopathology procedure in which sometimes the section becomes very deformed such that the peripheral contours don't match with pre-histology processing. Additionally, there is a high chance that the the particular histology section does not correspond to the top most layer. This is especially important because the DOCI imaging system uses ultraviolet-A (UV-A) illumination, which means the tissue penetration of the source is also limited to sub-millimeter [67]. It is common to slice off the top most portions of tissue sections using a microtome in order to obtain a full tissue slice during the histological processing. Therefore it is also highly likely that the tissue layer that were imaged are actually thrown away, leaving the processed histology slices to be tissue sections somewhere in the middle, which would not be an accurate representation of what was imaged by the DOCI system. These issue leads to the development of the second clinical process that was developed for human *in vivo* studies.

6.2.2 Human *in vivo*

A second clinical process was developed for *in vivo* experiments to address the issues of inaccurate DOCI-histology registration that occurred in the *ex vivo* process. Figure 6.4 shows the process that was developed registering *in vivo* experiment with histology.

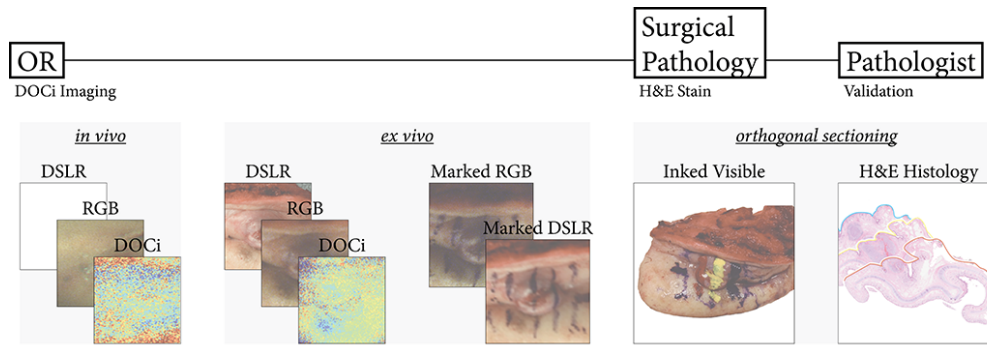


Figure 6.4: Human *in vivo* clinical experimental procedure.

The *in vivo* process is slightly more complicated as there are more intermediary steps that needs to be taken in order to register *in vivo* tissue with histology. The first is going through the entire imaging procedure; which is taking the DSLR image, RGB composite image, and the multi-spectral DOCI images of the region of interest on the patient *in vivo*. After the tissue is surgically removed, another set of of the imaging experiment is taken *ex vivo* in order to register *in vivo* results with *ex vivo* results as there might be tissue alterations during the surgical process. Without moving the *ex vivo* specimen after the imaging experiment, a surgical marking pen is used to annotate section lines on the sample that demonstrates remarkable contrasting features shown on the *ex vivo* DOCI image set. Afterwards, another set of DSLR image and RGB composite is taken as reference to where the tissue was marked. The marked specimen is then taken to surgical pathology where different colored pathology inks are drawn over the pen marks to annotate the orientation that pathologists need to section the tissue to provide gold standard ground truth for the DOCI experiments. When the histology slides are processed, the inked surface provides a reference to ensure that the histology section is definitively the layer that was imaged in the DOCI results.

One major difference is that all of the imaging experiments are all performed in the OR, which means that tissues are imaged before they are sectioned and therefore requires the researchers to dictate how the specimen section orientation. Otherwise there would be no intuitive way of correlating the results. This was only limited to clinical cases where

the tissue pathologies have well defined margins such as tongue SCCA, whereas intrusive pathologies like melanomas were off limits for this study due to clinical reasons.

The major issue with this method is that only a few perpendicular slices are taken, which means only the regions that were inked can be truly correlated. This means that 99% of the imaged results have no way to be directly correlated. Ideally, the entire specimen would be used to create a 3-dimensional layered histology to allow for a complete registration, however this is currently impractical at the massive scale [68]. Some other solutions that can be considered would be to increase the density of the sectioning lines or make the assumption that similar DOCI signal corresponds to similar tissue types.

6.3 DOCI Image Results

Figure 6.5 is an example of human *ex vivo* SCCA DOCI result at the transitional interface between normal and tumor tissue.

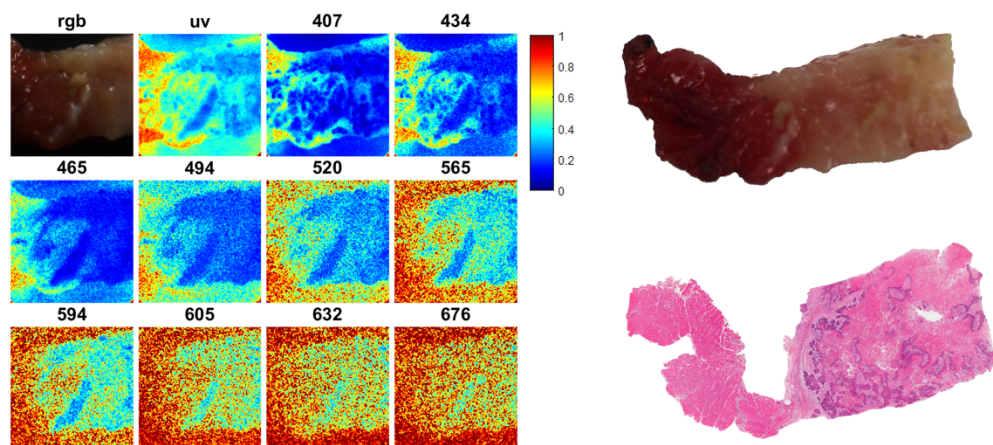


Figure 6.5: Human *ex vivo* SCCA image results. (left) Multi-spectral DOCI images, (top-right) DSLR color image, and (bottom-right) H&E stained histology image.

In the DSLR image, the whitish tissue on the right region of the tissue represents tumorous tissue while the reddish region on the left side corresponds to normal tissue. In the histology image, the left region of the tissue correlated with the DSLR whereas there is more heterogeneity on the tumorous right region. There is a large chunk of tissue that is missing at

the interface, which is a persistent issue for many experiments during histological processing step. The colorbar for the multi-spectral DOCI images shows values between 0-1, in which 0 represents tissue with short fluorescence decay while 1 represents long fluorescence decay. From this result, tumor has shorter fluorescence decay than normal tissue. These values are not calibrated in this system iteration and therefore only represents relative fluorescence lifetimes and contrast. Furthermore, it is also possible that DOCI signal >0.8 corresponds to fluorescence signal that has poor signal-to-noise and contains just noise. Most of the filters in this example shows remarkable contrast between normal and abnormal tissue.

Figure 6.6 shows an example of human *ex vivo* parathyroid DOCI result.

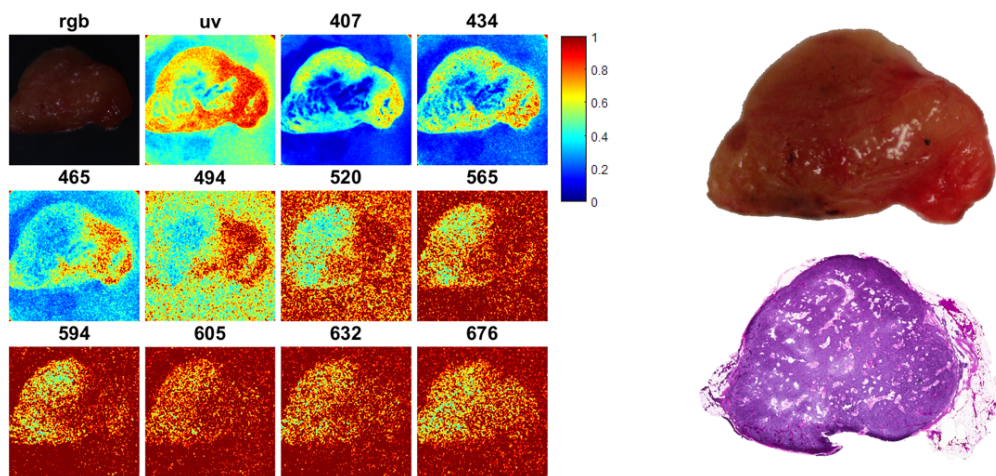


Figure 6.6: Human *ex vivo* parathyroid image results. (*left*) Multi-spectral DOCI images, (*top-right*) DSLR color image, and (*bottom-right*) H&E stained histology image.

In this example the brownish color on the DSLR image represents regions that are likely to be the parathyroid gland, whereas the pinkish tint on the right hand side of the tissue represents fat tissue. The H&E histology results shows a whole parathyroid gland on the left hand side while a sliver of adipose tissue appears on the right hand side. Similar to the SCCA result, the colorbar in the multi-spectral DOCI images shows that blue represents short fluorescence decay while red represents long fluorescence decay. Shorter lifetimes or blue represents parathyroid while the seemingly longer lifetime or red represent non-parathyroid peripheral tissue that encapsulates the parathyroid. The first row of DOCI images seems to

show that parathyroid is located only in the medial portion of the tissue. However, in the second row of DOCI images, it seems like only the left side of the tissue is parathyroid. The last row is much more difficult to see but the 676nm seems to show that the bulk of the tissue is parathyroid, which correlates with the deeper section of histology. This experiment shows that even though the signal-to-noise in longer wavelength is poor, it allows for deeper penetration into the tissue. However, there are currently no valid experiments to quantify the penetration depth of the DOCI system for the different optical wavelengths. Furthermore, another major issue in both of these *ex vivo* imaging is that the histology gets deformed and that the histology slice that is obtained might not be the top-most layer that was imaged. This makes the current method for registering DOCI images with histology impossible.

Figure 6.7 shows an example of human *in vivo* lip DOCI result.

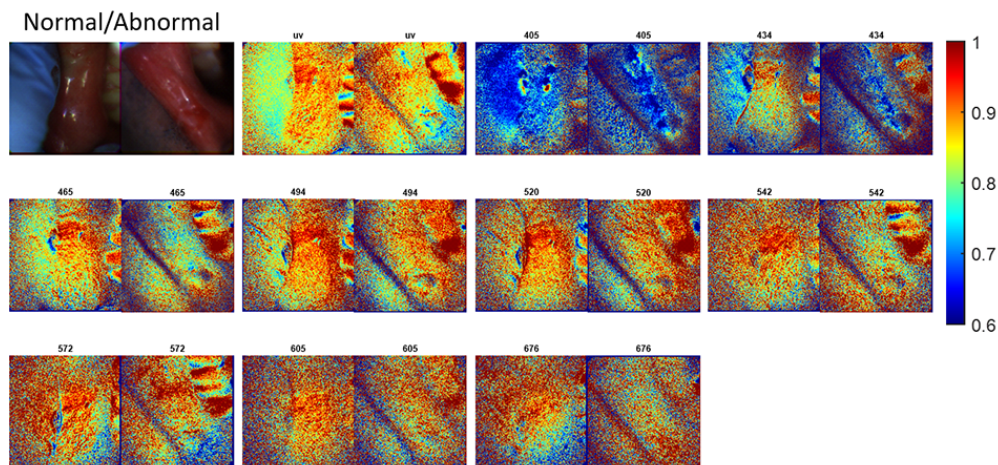


Figure 6.7: Human *in vivo* lip image results. Multi-spectral DOCI (*left*) normal lip and (*right*) abnormal lip.

These images were taken using the DOCI 2.0 system, where the camera and illumination behavior was slightly different compared to the *ex vivo* FLIM/DOCI 1.0 system. Therefore, the colorbar that represents the relative lifetime ratios is also very different and ranges from 0.6 to 1. The lip images are obtained from the same patient, which acts as a control. Just from the RGB composite image, it is noticeable that the pigment of the lips are slightly different. In the DOCI images, the 434nm shows the most pronounced different between

the normal and abnormal lips. The other filters seems to be more difficult in resolving the differences between the two lips. There is also a circular feature in the center of every DOCI image that represents the illumination gradient. In theory, the DOCI method should be insensitive to the illumination gradient. However, the illumination gradient can become a confounder if the signal-to-noise of the images are poor. Methods to quantify performance of system and image signal-to-noise has not been thoroughly conducted. Another potential confounder is radiative effect of exogenous peripheral objects such as tools, gloves, and other surgical equipments. The effects of objects that exhibit high reflectance or fluorescence on DOCI tissue images has not been studied. Additionally, the effects on tissue fluorescence when mechanical stress is applied also needs to be properly studied in order to identify confounding effects.

6.4 Experiment & Patient Documentation

Once the experimental portion is completed, the next step is storing, managing, documenting, and accessing specific datasets. One of the challenges is being able to quickly access a particular experiment on the spot without needing to spend hours making preparations. This entails creating a database and method of filtering of selecting experimental datasets in the vast data repository. Ideally, a comprehensive cloud database that allows for correlation of DOCI results amongst patient clinical data is needed because fluorescence decay characteristics is very sensitive to small changes [45]. Figure 6.8 shows a simplified example of several relational databases containing with specific IDs with the direction of arrows corresponding to 1-n relations of information flow.

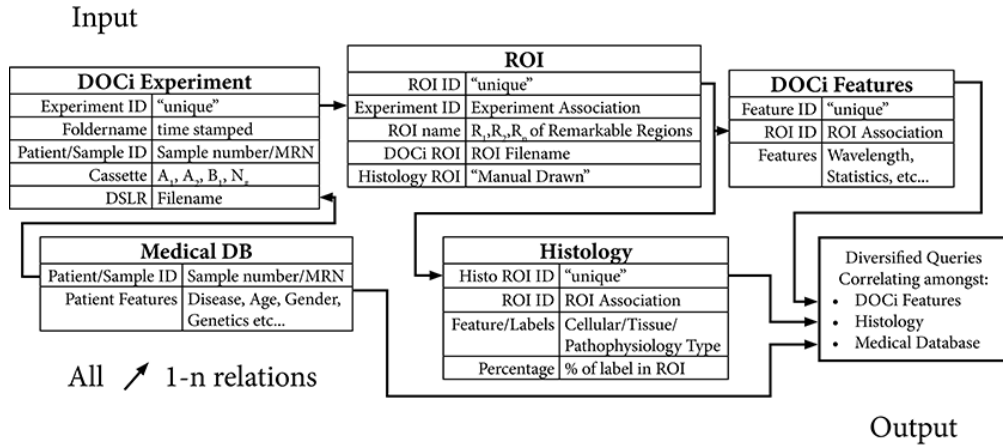


Figure 6.8: Simplified ideal database proposal.

The major purpose of creating such a comprehensive database is to allow for data consistency across heterogeneous patient populations. The beginning of this database flowchart starts with the medical database (medical DB) as this is what determines the patient sample size of the DOCI project. It should contain patient relevant information that are typically only accessible from clinicians. Having information such as the specific disease subtypes, medical history, age/gender of patients, genetics, and lifestyle habits can be used to determine whether any of these factors contribute to deviations or offsets in the DOCI lifetime ratio measurements. Similar to other existing medical imaging techniques, each patient may have multiple DOCI image scans in which each scan would be an entry in the DOCI experiment table. Each of these scans requires labeling regions that are relatively homogeneous from the fluorescence decay ratio and histology information. This leads to the next step of the diagram, which is the ROI database. Each DOCI images may consists of multiple region of interests (ROIs) that exhibit remarkable contrast. At the same time, two differentiable tissue types that exhibit similar DOCI signals would mean the fluorescence decay ratios are highly similar. This could lead to the ROI table splitting into multiple DOCI features and histology table. The DOCI feature table consists of the multi-spectral information and may contain various statistical outcomes for the particular pseudo-homogeneous ROI. The histology database can contain information for the specific ROI to have histopathology information such as cellular state, types of tissue, specific pathophysiology of tissues and cells

if they're abnormal, and the respective percentage or ratios. This database in conjunction with the DOCI feature database can potentially be used to determine what types of cellular features are insignificant or significant for generating tissue contrast. Ideally, comprehensive studies pertaining to molecular composition ratio of varying tissues would be needed to accurately extract all relevant fluorophores of interest. However, such comprehensive study or database are not known by the clinical collaborators that were part of the DOCI project. Finally, once all of the relevant databases, DOCI values, and clinical annotation are properly constructed; machine learning algorithms can be used to cross-compare to determine which clinical features result in changes in fluorescence decay.

If there are results that deviate from the hypothesis or expectations, it is important to identify the reason; which can be from a list of possibilities but not limited to patient heterogeneity, tissue heterogeneity, disease heterogeneity, system heterogeneity, or procedural heterogeneity. The creation of a master database will allow for faster and more precise identification of questionable results. However, due to current research limitations, most patient data are omitted at the current stage of the DOCI project. Figure 6.9 shows a rapid prototyped first iteration database created for the DOCI project in form of a table on a local system.

Excel Input													MATLAB Conversion									
J	A	B	C	D	E	F	G	H	I	J	K											
1	Folder	Sample	MIN	Cassette	Region	OSLR	Organ	Disease	pre-RDIs	post-RDIs	notes											
2	2014_12_11.11.49AM	S14	A1	R1	IMG_0769	neck	scca	tumor		lymphoma		'2015_05_28'	'S15'	'R15'	'IMG_0996'	'parathyroid'						
3	2014_12_11.12.55AM	S14	A2	R1	IMG_0770	neck	scca	mixed		lymphoma		'2015_05_28'	'S15'	'R15'	'IMG_0997'	'parathyroid'						
4	2014_12_11.12.02PM	S14	A3	R1	IMG_0772	neck	scca	normal		lymphoma		'2015_05_28'	'S15'	'R15'	'IMG_1000'	'parathyroid'						
5	2014_12_11.02.24PM	S14	A3a	R1	IMG_0774	parathyroid		parathyroid				'2015_05_28'	'S15'	'R15'	'IMG_1001'	'parathyroid'						
6	2014_12_11.02.30PM	S14	A3b	R1	IMG_0775	parathyroid		parathyroid				'2015_06_01'	'S15'	'R15'	'IMG_1002'	'larynx'						'eosa'
7	2014_12_11.02.53PM	S14	A3b	R1	IMG_0776	parathyroid		parathyroid				'2015_06_01'	'S15'	'R15'	'IMG_1003'	'larynx'						'eosa'
8	2014_12_11.02.59PM	S14	A3i	R1	IMG_0777	parathyroid		parathyroid				'2015_06_04'	'S15'	'R15'	'IMG_1004'	'parathyroid'						'eosa'
9	2014_12_11.03.00PM	S14	A181a	R1	IMG_0778	parathyroid		parathyroid,thymus				'2015_06_08'	'S15'	'R15'	'IMG_1006'	'mouth'						'eosa'
10	2014_12_11.03.19PM	S14	A181j	R1	IMG_0779	parathyroid		parathyroid,thymus				'2015_06_11'	'S15'	'R15'	'IMG_1007'	'parathyroid'						'eosa'
11	2014_12_11.03.33PM	S14	A182a	R1	IMG_0784	parathyroid		parathyroid,thymus				'2015_06_11'	'S15'	'R15'	'IMG_1008'	'parathyroid'						'eosa'
12	2014_12_11.03.42PM	S14	A182b	R1	IMG_0785	parathyroid		parathyroid,thymus				'2015_06_11'	'S15'	'R15'	'IMG_1009'	'parathyroid'						'eosa'

Figure 6.9: Microsoft Excel-MATLAB DOCI experiment database/table implementations. (left) Microsoft Excel user input table. (right) MATLAB converted table.

This rapid-prototyped database implementation allows for the experimental folders to be filtered base on tissue types, experiment types, patient sample number, date, tissue cassette sections, and the recorded DSLR number. The data entry is input in a Microsoft Excel spreadsheet for operations simplicity and the table is converted into a MATLAB table to allow software filtering and parsing. The following few sections will describe the current

implementations and challenges that uses this database in an attempt to register subsections of the image with histology. Furthermore, all of the image registration methods were only performed on results acquired using the human *ex vivo* process as explained in section 6.2.1 as the results are obtained in a well-controlled environment with limited confounding factors.

6.4.1 Image Registration - 1st Iteration

This section will give an overview of the initial methodology and tools used to attempt to register DOCI images acquired using the *ex vivo* process. The first iteration for image registration was rapidly developed such that the data can be quickly accessed by providing methods to filter dozens of experiments in order to access a particular dataset specified by the pathologist. In this attempt, the time spent coordinating with a pathologist, surgeon, and engineer/researcher to annotate data was very difficult and methods for quickly accessing data was necessary.

First, the surgeon and pathologists would have to schedule a time such that both are available while the researcher would have to work around the clinicians schedule. Next, the surgeon and researcher would create a list of experiments that needs to be analyzed. Usually it takes 1-2 weeks for the experiments to be processed with H&E stain, so the most recent experiments at the time would be backlogged to future meetings. The pathologist would go through the histology repository and obtain a stack of histology slides that are requested for the meeting. During the meeting, the pathologists would go from the top of the list and go through the slides sequentially in no particular order. In the mean time, the engineer/researcher would have to quickly go through a database of experimental folders and quickly select the right directory. Figure 6.10 shows an example of a software interface that was developed in MATLAB that allows traversing through vast experiment database by using reference keywords provided by clinicians.

Queries: "tongue"					Queries: "S14-####"								
'2014_12_22'	'S14-	'F1'	'R1'	'IMG_0804'	'tongue'	'scca'	'2014_09_08'	'S14-	'F1'	'R1'	'IMG_0580'	'tongue'	'scca'
'2014_12_22'	'S14-	'F2'	'R1'	'IMG_0805'	'tongue'	'scca'	'2014_09_08'	'S14-	'F1'	'R2'	'IMG_0580'	'tongue'	'scca'
'2014_12_22'	'S14-	'F3'	'R1'	'IMG_0806'	'tongue'	'scca'	'2014_09_08'	'S14-	'F2'	'R1'	'IMG_0581'	'tongue'	'scca'
'2015_01_12'	'S15-	'R1'	'R2'	'IMG_828'	'tongue'	'scca'	'2014_09_08'	'S14-	'F2'	'R2'	'IMG_0581'	'tongue'	'scca'
'2015_01_12'	'S15-	'R2'	'R1'	'IMG_829'	'tongue'	'scca'	'2014_09_08'	'S14-	'F3'	'R1'	'IMG_0582'	'tongue'	'scca'
'2015_01_12'	'S15-	'R3'	'R1'	'IMG_830'	'tongue'	'scca'							
'2015_01_28'	'S15-	'J1'	'R1'	'IMG_0856'	'tongue'	'scca'							
'2015_01_28'	'S15-	'J2'	'R1'	'IMG_0857'	'tongue'	'scca'							

Figure 6.10: Database filtering and case selection. (*left*) Filtering by tissue types for data analysis. (*right*) Filtering by patient for histopathology-DOCI registration.

This MATLAB software implementations allows for the user to type in small text fragments to filter particular entries, in which the software will simultaneously generate a filtered table from the previous displayed table. The example shows that by inputting "tongue", all of the experiments that are not tongue will be filtered out, resulting in only experiments that contains tongue. This is important when trying to isolate specific organs or tissue types when performing data analysis as different tissue may contain very different fluorophore compositions. The second example shows that entering a patient sample reference within the "tongue" subset table will filter out all other experiments that are not for the specific patient. This filtering method is not limited to just tongue and patient reference and can be used for any categorical features listed in the original Excel spreadsheet. This implementation allows a rapid method to quickly filter hundreds of experiments down to a small handful in a very short amount of time. The filtering within the user interface continues until a unique entry remains. Figure 6.11 shows the first iteration for ROI selection graphical user interface (GUI) developed in MATLAB when the database filter reduces down to a single entry.



Figure 6.11: First DOCI image ROI selection.

This user interface displays four figures - multi-spectral DOCI images, RGB composite, DSLR image, and a ROI selection interface, in which the first three figures are used only for visualization and peripheral information to make informed ROI selection. No longer is it necessary to open folder directories to select individual experiments. The DSLR image is used for histology orientation due to the fact that the histology in the first *ex vivo* process were sliced parallel to the surface, while the ROI was drawn on the RGB composite as a way to minimize DOCI-biased ROI selection. Prior to ROI selection, a microscope that have shared objective view is used and the pathologists would guide both the surgeon and the engineer/researcher through the histology slide sample, making comments on remarkable feature. At the same time, the researcher would have to quickly scramble through individual DOCI experiments, try to orient the DOCI image results to match with the histology slide, and draw ROIs for the experiment. Figure 6.12 shows the format that the ROI is saved after an ROI is selected and a label is typed in.

 632_x1 02.34.35PM	9/18/2014 2:34 PM	TIF File	2,049 KB
 632_x2 02.34.35PM	9/18/2014 2:34 PM	TIF File	2,049 KB
 676_x1 02.34.48PM	9/18/2014 2:34 PM	TIF File	2,049 KB
 676_x2 02.34.48PM	9/18/2014 2:34 PM	TIF File	2,049 KB
 b 02.31.43PM	9/18/2014 2:31 PM	TIF File	2,049 KB
 g 02.31.41PM	9/18/2014 2:31 PM	TIF File	2,049 KB
 r 02.31.39PM	9/18/2014 2:31 PM	TIF File	2,049 KB
 roi_normal_parathy...	10/16/2014 2:41 PM	MATLAB Data	1 KB
 roi_parathyroid	10/16/2014 2:41 PM	MATLAB Data	1 KB
 tissue_mask%%201...	12/30/2014 3:31 PM	MATLAB Data	25 KB
 uv_x1 02.32.07PM	9/18/2014 2:32 PM	TIF File	2,049 KB
 uv_x2 02.32.07PM	9/18/2014 2:32 PM	TIF File	2,049 KB

Figure 6.12: DOCI region of interest (ROI) database implementations. (*top*) Manual registration between DOCI data and histology reference. (*bottom*) ROI database for each respective experiment.

In this first iteration, the ROIs are saved directly within the folder of the experiment in MATLAB data format (.mat). The ROIs that the user selected in the GUI are saved as x and y coordinates to minimize file size. These coordinates can be used to generate a binary black and white mask as previously shown in figure 6.11 on the bottom right image.

Sometimes detailed explanations of tissue features resulted in ROI labels that were confusing and inconsistent, such as tumorous cells that were necrotic, regions with highly proliferative cancer cells, or highly calcified regions. While each feature has significant clinical implications, it also means that the molecular properties of abnormal or tumor categorization are also extremely heterogeneous and that fluorescence decay in biological tissue is weighted heavily on collagen, elastin, and NADH ratio. Other abnormalities such as calcification creates a new dimension of fluorescence in which inorganic compounds and crystalline structure becomes prevalent [69, 70].

The process of annotating, classifying, or clustering groups of data will create high uncertainties if the underlying pathophysiology and medical implications are not properly identified. This process for annotating one of the slides can take 5-15min and even then, everything is very rushed. There are dozens of slides that needs to annotated in each meeting because the amount of DOCI experiments that can be performed in a single day varies from 2-27 datasets. Unless a meeting is scheduled every other day, which is unlikely because H&E

staining process itself takes 1-2 weeks; a backlog of 20-60 histology slides every 1-2 weeks is common. The amount of time that is required to attempt to obtain accurate ROI selection becomes impractical using this initial method. The next few sections will use this process as a baseline and attempt to streamline the image registration process by improving task distribution and developing more intuitive tools.

6.4.2 Image Registration - 2nd Iteration

In this iteration, a completely new research management process was introduced to allow for each individual researcher and clinical investigator to be able to work independently on their own time. This is essential because it increases the amount of time slots that work can be performed and reduces time that is needed for coordination and communication. In this iteration, the needs to quickly find specific experiments in a repository of data is no longer needed, but instead a list of all experiments are transferred from one researcher to another. One of the first criteria is that all histopathology slides are digitally scanned and documented. This is important to ensure that all information is intact and registered digitally and that future data archeology will no longer be needed. All of the SCCA *ex vivo* samples were scanned from experiments using the FLIM/DOCI 1.0 system because the images were taken in optical and mechanical stable environment. The resolution of the digital scans will be dependent on the pathologists' needs to make the most informed annotation, which for this new process came down to be 16x magnification. There is also more tissue diversity and heterogeneity in SCCA experiments compared to parathyroid experiments. However, no magnification is needed for the sake of selecting ROIs.

A software interface was developed to sequentially goes through the entire sub-clinical dataset via all SCCA cases, and digital histology scans would be manually modified in the form of rotation and reflection to match the orientation of the DOCI image. The DOCI experiments and histology scans are registered together using a database table shown in figure 6.13.

1	Date	Experiment	Sample #	Region	DSL	Organ	KB	Histo ref	Cassette	Usable? 0	Histology ROI performed?
2	2014_09_08	2014_09_08 04.16PM	S14-	R1	IMG_0580	tongue		72578	f1	0	Too much artifact
3	2014_09_08	2014_09_08 04.26PM	S14-	R2	IMG_0580	tongue		72578	f1	0	Too much artifact
4	2014_09_08	2014_09_08 04.46PM	S14-	R1	IMG_0581	tongue		72579	f2-1	2	
5	2014_09_08	2014_09_08 05.02PM	S14-	R2	IMG_0581	tongue		72579	f2-1	2	
6	2014_09_08	2014_09_08 05.15PM	S14-	R1	IMG_0582	tongue		72580	f3-1	0	Histology not complete to match
7	2014_09_17	2014_09_17 04.43PM	S14-	R1	IMG_0593	neck				na	
8	2014_09_17	2014_09_17 04.56PM	S14-	R1	IMG_0594	tongue		72581	i1-1	0	multiple fragments
9	2014_09_17	2014_09_17 05.05PM	S14-	R1	IMG_0595	tongue		72582	i2-1	0	multiple fragments
10	2014_09_17	2014_09_17 05.28PM	S14-	R2	IMG_0595	tongue		72582	i2-1	0	multiple fragments

Figure 6.13: DOCI experiment and histology registration.

Although there are several categorical columns in this table, the most important features are the time stamped experiment, the histology reference, and whether the histology data is usable. All the other categories are metadata used to assist in the registration process. One thing to note from this example is that this was a testbed for creating a new research process. Few things were not standardized, which resulted in data entry that deviated from the intended values e.g "na" in usability as opposed to a 0. After the DOCI experiment and histology is registered properly, the next phase is to create ROIs. Figure 6.14 shows a software GUI developed in MATLAB for selection of ROIs.

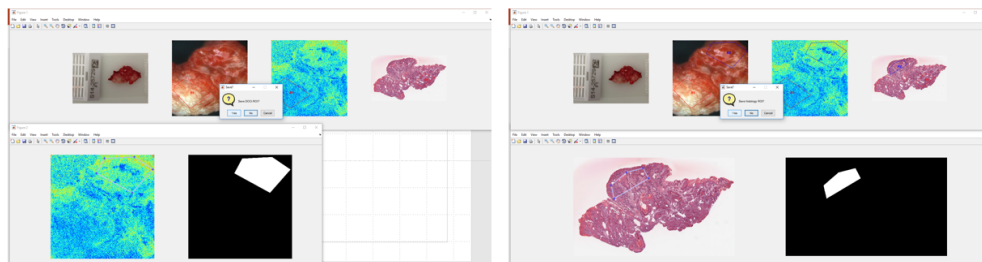


Figure 6.14: Second DOCI experiment ROI selection. (left) ROI selection on DOCI image. (right) ROI selection on histology image.

In the first version, the ROI of the histology was not considered because the DOCI ROI was selected on the fly while looking at the histology slides. This second version was developed so that digital records for ROIs drawn on both DOCI images and histology images are always accessible. The histology image was manually rotated and/or flipped to match the orientation from the DSLR images. Afterwards, the user interface will display all the relevant images to allow the user to draw ROIs on a DOCI image. Afterwards, the histology image will show up to allow the user draw ROIs on the histology image. After the are created

from the ROI, a MATLAB script is used to create a list of all of the ROIs that were drawn as shown in figure 6.15.

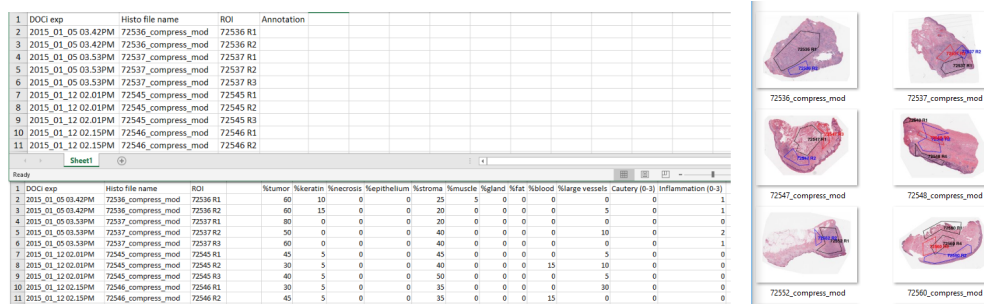


Figure 6.15: DOCI region of interest (ROI) database implementation. (*top*) ROI database from each experiment, (*bottom*) ROI database with pathologist’s labeling, and *right* histology with ROI annotations.

The MATLAB script was used to parse through every single folder that was created and has the experiment foldername, histology image filename, and the ROI filename. After the ROI database is generated and exported in Excel format, the database and the all of the histology images with ROI annotations are sent to the pathologists for tissue annotation. In this example, the pathologists created 9 tissue categories, a cautery rating, and an inflammation rating. The pathologists would use the low-resolution annotated histology image and reconstruct similar ROI in the 16x magnification high-resolution histology scans to determine the percentage of each tissue types. Some of the problems with both iteration first and second of the ROI selection GUI is the popups of figures one after another. Sometimes the sequence of actions might be unintuitive and methods of correcting mistakes or checking if accurate annotations of labeled are difficult. However, the major benefits of the second iteration for image registration is that the research investigators can all work independently and that each process have digital references that can be backtracked if uncertainties in any step occurs. Furthermore, this distributed research model enables future project scalability by parallelizing various tasks for researchers that specializes in their respective fields.

6.4.3 Image Registration - 3rd Iteration

The third and last iteration of the image labeling software GUI was created to address the ambiguous UI and allow methods to quickly check the accuracies of previous ROI annotations. Figure 6.16 shows the GUI that was developed in the third iteration.

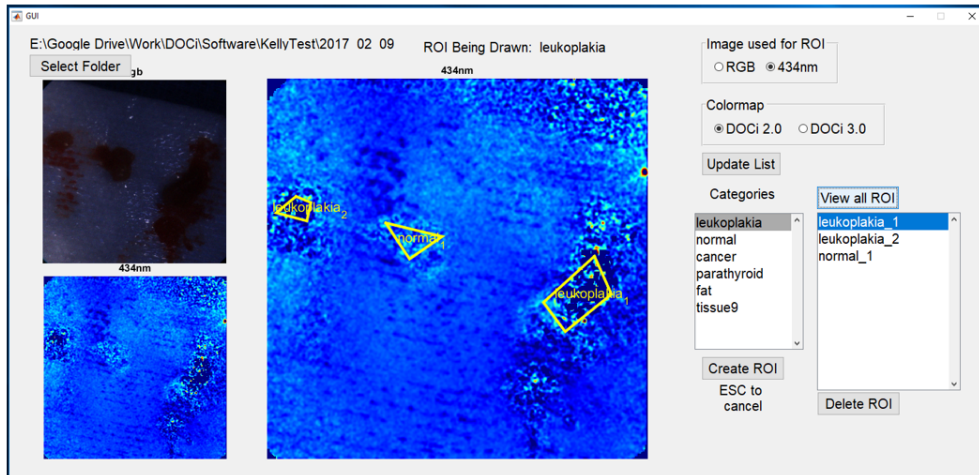


Figure 6.16: Third DOCI image ROI selection.

The intent of the third GUI is to create a more intuitive user friendly interface starting out with the experiment selection. On the top left corner, the user can select the experiment folder and the software will process the RGB and the 434nm DOCI image to allow the user to draw ROIs. These two specific images were selected because the RGB image is useful for demarcating tissue boundaries against background while the 434nm DOCI image has historically been excellent in terms of signal-to-noise and producing remarkable contrast between tissues. The left panel of the GUI shows both the RGB and 434nm DOCI images as references to what the image looks like. The center panel is the primary image panel for the user to draw ROIs and to view ROIs that were drawn for this experiment. The right panel contains all of the user controls for using the GUI. On the top of the control panel, the user can select whether they want the center panel to display the RGB or 434nm DOCI image. Next, a simple control to alter the heatmap of the DOCI image depending on the version of the system. Lastly, there are control options to create ROI, display specific ROI, delete specific ROI, and display all ROI drawn for the experiment. A list of preset categories

is also displayed to allow for quick selection of tissue types when drawing ROIs. The presets can be changed from an external text file to prevent constant alterations. Histology image implementation was not included in this iteration because this GUI was developed for a clinician to annotate regions of tissue from the DOCI 2.0 and 3.0 system that do not have the histology digitally scanned. Issues with directory paths was also an issue when the software was ported from Windows OS to macOS. Ideally, a similar GUI should be developed and compiled as a static build to allow for the program to run as standalone executable.

6.5 Discussion

Translating an *ex vivo* research system used in a lab setting into the operating room for *in vivo* patient experiments requires many intermediary steps and abundant considerations with research logistics. Engineering better systems or acquiring more accurate images are not enough to allow research projects to translate into the clinical setting, especially for high diversity of patient population. The need to sustain data integrity while minimizing the time required to complete the full clinical process is extremely difficult. This preliminary overview of the clinical workflow that was developed for the DOCI project requires knowledge across scientific fundamentals, project management, clinical logistics, technology integration, and rapid-prototyping of tools. The lack of science fundamentals will prevent understanding limitations in the physics and biology of the project. Poor project management will result in extremely costly research process that seems to have no end in sight with high data variations. Understanding the full process of the clinical logistics allows for alterations in existing clinical workflow without compromising patient outcome. Lastly, the ability to identify and integrate unconventional technologies and rapidly develop prototype systems into the research process can achieve unexpected promising outcomes.

CHAPTER 7

Image Processing

There are several imaging techniques that were applied to the DOCI images, but not unique to the DOCI method. These techniques includes background subtraction, white balancing for the RGB composite image, and various filtering techniques to enhance image quality. However, none of these methods can compensate for motion when *in vivo* DOCI images were taken. This chapter will primarily be focused on motion correction as this specific types of problem is relatively uncommon compared to other biophotonic imaging modalities.

7.1 Motion Correction

Prior to the development of motion correction algorithms, it was necessary for both the patient and the physician to remain as steady as possible. However, the success yield is very low and many experiments required multiple re-runs in order to acquire data that had minimal motion. For the DOCI method, motion correction is an important stage in analyzing the images because the steady state and decay state images are taken at different time points. For *in vivo* experiments, motion can occur from either the patient or from the clinician and even small amounts of motion can cause noticeable artifacts in the images. Therefore, motion correction is a prerequisite step to data analysis. Motion correction methods are usually achieved by selecting a reference image and augment the other images to the fixed reference [71]. Scale-invariant feature transform (SIFT) method was implemented to solve patient motion with *in vivo* DOCI images.

7.2 Scale-Invariant Feature Transform (SIFT) Overview

Scale Invariant Feature Transform (SIFT) has been widely developed in the robotics and computer vision industry standards for more than a decade now with applications ranging from autonomous feature matching, searching, image stitching (panorama stitching), and vehicular/object motion tracking [72, 73]. SIFT is also used in multiple medical imaging applications to allow automatic registration of multiple volume scans such as optical coherence tomography (OCT), magnetic resonance images (MRIs) [74], computed tomography (CT) images [75], and positron emission tomography images [76]. The SIFT algorithm can be broken into several key stages [72, 73]:

1. The creation of the image scale space as shown in figure 7.1.

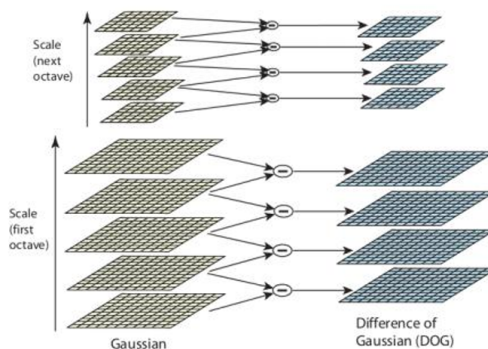


Figure 7.1: Image scale space.

Each image scale octave is the image convolved with with different size Gaussian filters.

2. Approximating Laplacian function, which is the 2^{nd} derivative of an image data. This is accomplished by using Difference of Gaussians (DoG) approximation to simplify computation. The Laplacian kernel is computed to be the subtraction between 2 Gaussian kernels of different standard deviations (σ) as shown in figure.

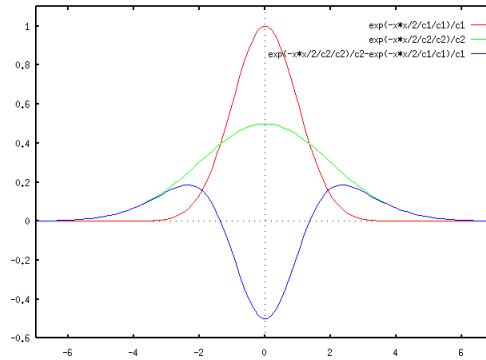


Figure 7.2: Visualization of Gaussian curves and Different of Gaussians. (*red*) and (*green*) curves are Gaussians with different σ . (*blue*) curve is the the resultant DoG curve that is computed by the subtraction between the two Gaussian curves.

From linear time-invariant systems theory, $I(x,y)$ is the original image and $H(\sigma)$ is the Gaussian filter of varying σ as shown in Eq. (7.1).

$$I(x, y) * [H(\sigma_n - \sigma_{n+1})] = I(x, y) * H(\sigma_n) - I(x, y) * H(\sigma_{n+1}) \quad (7.1)$$

3. Finding keypoints from DoG frames, which is defined as the local 3-D maxima/minima using a 3-D quadratic Taylor's expansion interpolation from a stack DoG frames as shown in figure 7.3.

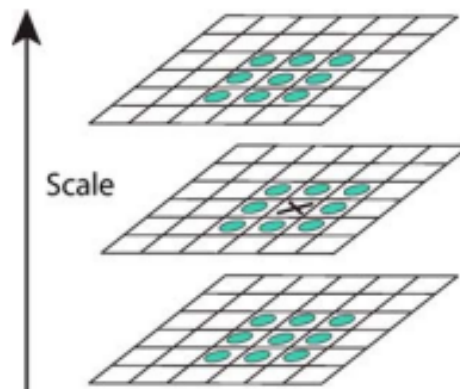


Figure 7.3: Identifying local "3-D" optima by stacking multiple DoG frames.

4. Filtering low contrast and poorly localized edge keypoints.

5. Computing the feature orientation, which creates a gradient vector map around each keypoint pixel .
6. Assigning local image descriptor using areas around keypoints as shown in figure 7.4 [77].

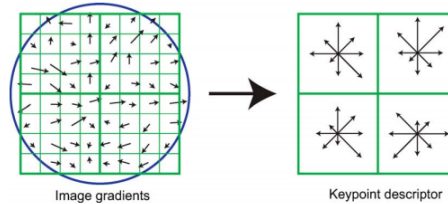


Figure 7.4: Gradient vector map for each optima.

7. The descriptors between 2 images are compared using variants of nearest neighbor indexing and hough transform clustering, in which each descriptor contains 128 feature vectors.
8. With two sets of mapped descriptors, a similarity transformation matrix (scaling, rotation, translation) can be generated from the pairs of x and y coordinate arrays.
9. The transformation matrix applied to image 2, which can be either the decay DOCI image or the green & blue channels in the RGB brightfield image.

For the DOCI project, the implementation of the SIFT algorithm was provided using the VLFeat open source computer vision library for the local feature extraction and matching. Once the SIFT descriptors were mapped, the distance formula for each descriptor x and y pixel pairs was calculated to determine the total pixel distance that the algorithm was correcting. The pixel distance can then be translated into real distances. A user-defined percentage of pixels were then filtered out in the order of maximum pixel distance translation to reduce noise during the translation. A built-in MATLAB "estimateGeometricTransform" function was used to calculate the transformation matrix for the final sets of SIFT descriptors.

7.3 Motion Correction Results

This section will review the results that applies the SIFT algorithm with images acquired from the DOCI system. Figure 7.5 shows an example of feature selection mapping between the steady state and decay state of fluorescence lifetime images.

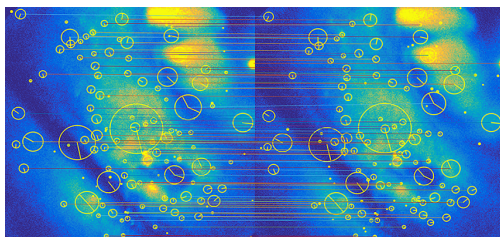


Figure 7.5: Example of SIFT features mapping. *(left)* Steady state fluorescence image and *(right)* decay state image

Each of the circles shows remarkable features that the SIFT algorithm extrapolates with the line within each circle as the vector direction of the resultant sum of image gradients. The lines that map features from steady state and decay state images show result of the automated feature mapping using the SIFT algorithm. Figure 7.6 shows the SIFT algorithm applied to stacking individual red, green, and blue filtered brightfield images using the DOCI camera.

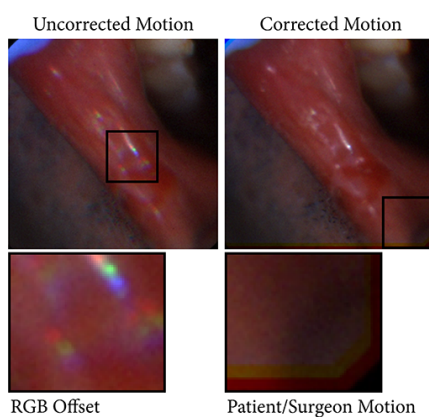


Figure 7.6: Example of SIFT algorithm applied to RGB images. *(left)* Before motion correction and *(right)* after motion correction

Before motion correction is performed, an RGB separation artifact can be seen when stacking the three channel images. After motion correction, the RGB separation is corrected to become white. At the same time, near the edge of the color image, three separate image layers can be seen, in which the pixel offset count can be used to determine the net motion that is introduced. Figure 7.7 shows an example of a DOCI result before motion correction for both normal and abnormal lip from the same patient.

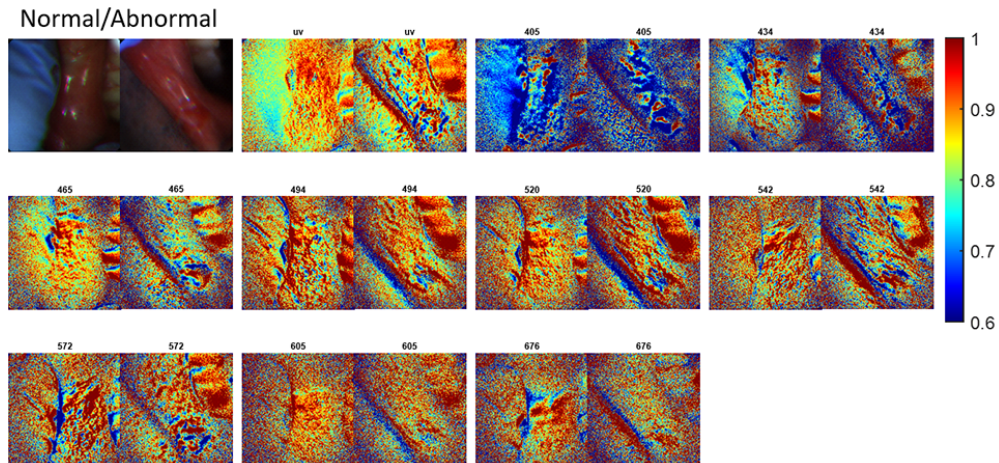


Figure 7.7: DOCI result before motion correction for both normal and abnormal lip

From this particular example, much of the image produces noise, which can be identified by the sharp blue & red contrast. If the percentage of sharp blue or sharp red is quantified, then it can be a potential method for determining the quality of the DOCI image. The colorbar from 0.6 to 1 is a random scale that was selected to produce sufficient contrast in this particular DOCI system iteration. Figure 7.8 shows an example of a DOCI result before and after motion correction for a normal lip.

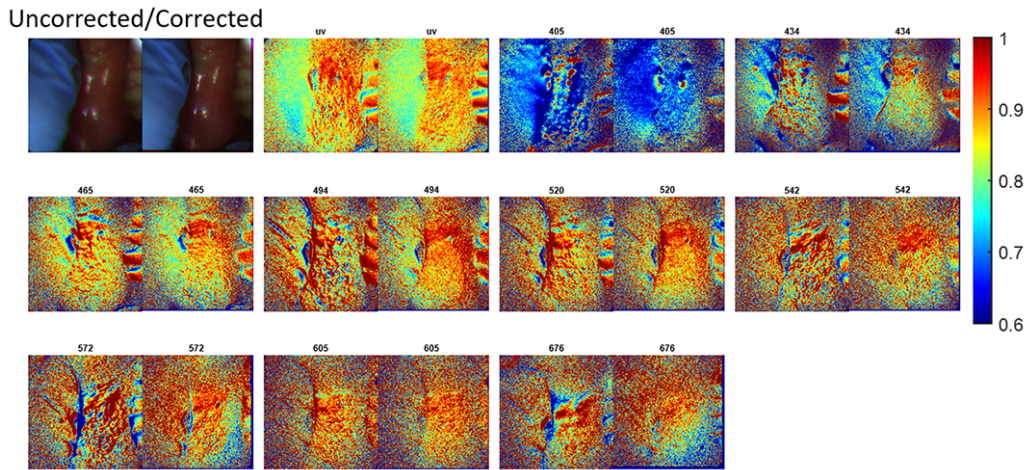


Figure 7.8: DOCI result before and after motion correction for normal lip

Figure 7.9 shows an example of a DOCI result before and after motion correction for an abnormal lip.

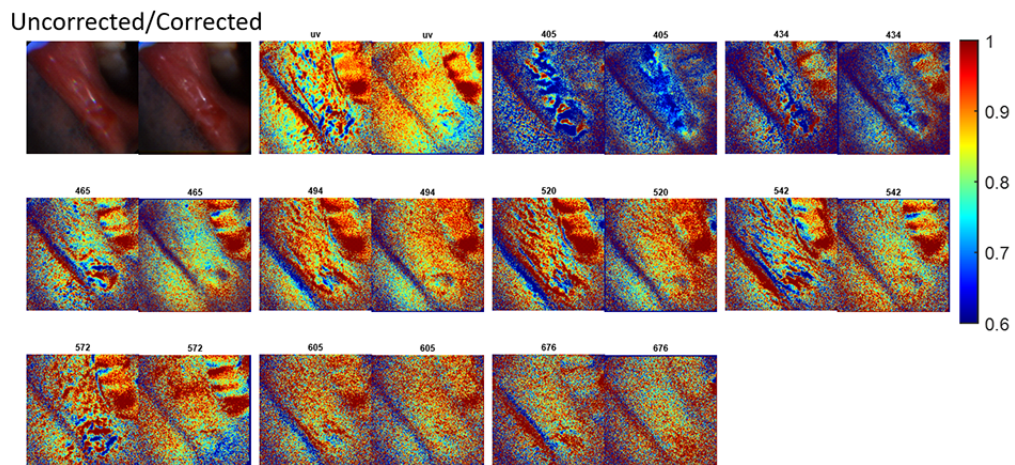


Figure 7.9: DOCI result before and after motion correction for abnormal lip

One remarkable feature from both the before and after motion correction of the normal and abnormal lip is the highly contrasting solid red & blue feature that represents DOCI data above and below the ranges of the color schema. Such abrupt change does not make sense because the tissues in adjacent regions should be relatively similar or have transitional gradient features. Identifying the percentage of these abrupt changes may be a potential method for determining image quality of DOCI images in response to motion artifacts.

Figure 7.10 shows an example of a DOCI result after motion correction for both normal and abnormal lip from the same patient.

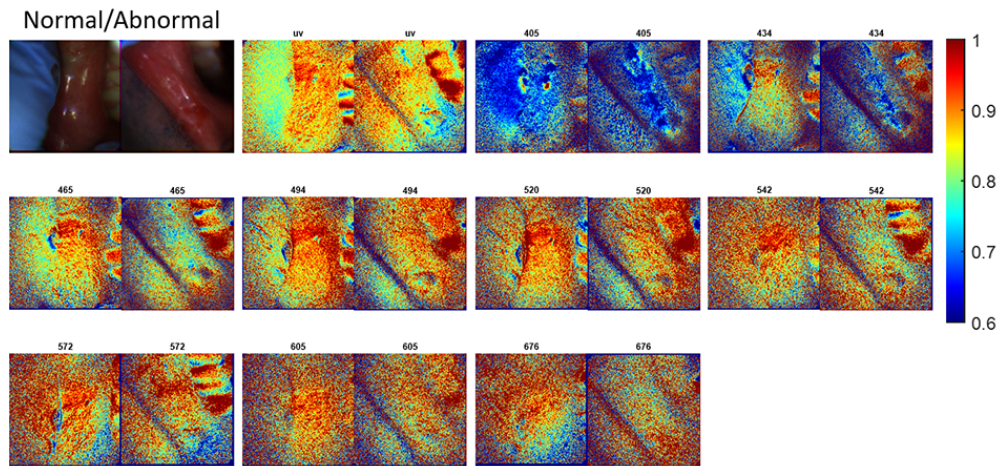


Figure 7.10: DOCI result after motion correction for both normal and abnormal lip

When the motion is corrected, the abrupt red & blue features are reduced. Features in the teethes are still pronounced, but this may be due to the highly fluorescent nature of the teeth that is causing signal saturation in the detector.

7.4 Discussion

Although there are already highly heterogeneous tissue samples in *ex vivo* experiments, there is another layer of complexity when performing experiments *in vivo*. Patient motion and additional background noise is introduced as the imaging environment may not always be well-controlled. Attempts using 2D Cross-Correlation was first performed, but the technique only allowed for 2-dimensional motion correction in the x and y direction. The technique does not compensate for rotation or z-directional motion. This led to using the SIFT method, which can correct for all x,y,z translation motion along with two degrees of freedom of rotation.

From the 2-D image, the z-direction translation correction can be interpreted as scaling the whole image, in which a scaling factor greater than 1 would be further from the camera

while scaling factor less than 1 would result in moving closer to the camera. The before and after motion correction results show the importance of motion correction algorithms in order to enhance image quality for the DOCI system. The ability to reduce the sharp red & blue contrast is a feature that motion correction algorithms can help improve image quality. Some issues that arise from these *in vivo* lip images is that a noticeable circular ring also appears near the center of the image. This seems to show the illumination profile of the illumination circuit, in which photons are highly concentrated in the center while near the edges. Methods for determining sufficient signal-to-noise is necessary in order to determine which regions of the image can be accurately analyzed.

Motion artifacts in images is inherent in most *in vivo* experiments and a need to identify methods to correct for these is necessary. There is limited number of ways to quantify the quality of images and using this sharp red-blue contrast is not a proven method to assess the quality of images. However, the qualitative assessments of the results generated using SIFT in the previous few figures seems to show significant improvement to the overall image quality. Some challenges that have not been resolved is determining which pixel provides sufficient signal-to-noise for accurate analysis. This can be performed by characterizing the noise of the DOCI system, which includes the detector, the illumination, and software.

For *in vivo* patient images, motion will always occur over the span of the experimental time. For massive clinical trial, it is essential that motion correction is fully automated. Otherwise, each experiment may take 5-10min to manually align through translation, rotation, and scaling. Manual alignment is also susceptible to human bias and human error. Furthermore, the analysis of pixel deviations that are corrected can be a prospective way of determining how fast the DOCI method has to be to bypass the need for any motion correction algorithms.

CHAPTER 8

Conclusion

A conceptual road-map for translational research and project scalability was developed for the DOCI project. Methods for a generalize DOCI theoretical model and calibration techniques were developed. Experimentation in various aspects of research management were attempted to demonstrate the significance of every process. Many of these issues are typically neglected in academic setting due to the lack of academic novelty and publication possibilities; but is necessary for successful clinical translation. The DOCI system has been automated in order to accelerate data acquisition process, reduce human error, and enabled *in vivo* clinical practicality. Process for reproducing illumination pulse profile was introduced, but the illumination pulse shape is still non-ideal. Various calibration methodologies were attempted in order to cross-validate computational system standardization. Several methods and tools were developed for registering research data with gold-standard histology, but the issue is still a major challenge. Preliminary image processing solutions were used to correct *in vivo* translational problems, but there are still many uncertainties in characterization of the system and image noise.

CHAPTER 9

Future Work

There are numerous of issues in the DOCI project that were discussed after the end of every section in the thesis, but the future direction of the project should be trying to accurately complete the six key phases of the project cycle. Performance assessments of the DOCI system can then be assessed to determine the clinical effectiveness of using fluorescence lifetime as a method to differentiate tissue. This final chapter will highlight some of the key issues that were encountered during this research.

9.1 Data Management

Issues with data management includes a mix of data acquisition, experiment labeling, data storage, which is being able to document and label data accurately. Having information such as the specific disease subtypes, medical history, age/gender of patients, genetics, and lifestyle habits can be used to determine whether any of these factors contribute to deviations or offsets in the DOCI lifetime ratio measurements. If there are results that deviate from the hypothesis or expectations, it is important to identify the reason; which can be from a list of possibilities but not limited to patient heterogeneity, tissue heterogeneity, disease heterogeneity, system heterogeneity, or procedural heterogeneity. After properly assigning labels can machine learning and artificial intelligence algorithms be performed to provide accurate results.

9.2 Registration, Region of Interest Selection, and Multivariate Statistical Analysis

Image registration between DOCI images with the current gold standard of histology is a challenge not only for the DOCI project, but in many emerging medical imaging modalities. Being able to correlate research results with histology is essential because this is the current fundamental ground truth. This thesis attempted both horizontal and vertical two-dimensional slices, but the registration is still very difficult and time consuming. Developing a more streamlined process or finding alternative methods to register the DOCI data with the histology methods should be explored. Preliminary results using pseudo-automated ROI selection as a prospective alternative method can provide faster annotation process while removing human bias as shown in figure 9.1.

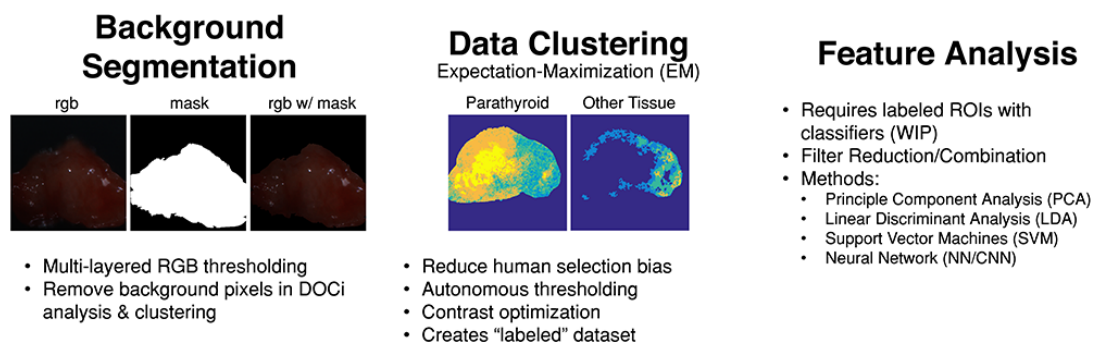


Figure 9.1: (*left*) Automated RGB background segmentation, (*center*) automated region of interest clustering, and (*right*) feature analysis using machine learning techniques.

The concept of automating of ROI selection is to streamline the process even further and to provide non-bias demarcation. The background segmentation uses RGB thresholding that allows separation of the background from the tissue. This mask would act as a filter that would remove any background data that are mistakenly selected by the researcher. The data clustering automates grouping of data points that have similar values in bins. This technique assumes the DOCI method works properly and that that similar DOCI values represents similar tissue types. Data clustering techniques can be applied to individual DOCI wavelength images as oppose to the researcher aggregating all the information and

select a few ROI for the particular experiment. Clusters of ROIs in each wavelength can be used to create a voting schema that represents overlapping information amongst the spectral data to provide confidence or likelihood values. The regions of high tissue homogeneity can then be labeled by a clinician without needing to spend time to demarcate regions.

Once the properly annotated ROI dataset is constructed, various methods of statistics, machine learning, and artificial intelligence algorithms can be used to rationalize the results. Specifically, algorithms that provides statistical results from multivariate input and multivariate output would be needed to process the multi-spectral DOCI input and the heterogeneous tissue ratio output respectively. However, the multivariate output could potentially be simplified into single output category to allow for more common algorithms to be used.

9.3 Noise Characterization

Preliminary models of the DOCI method using propagation of uncertainties were derived in the DOCI theory section. However, there are still other noise sources that hasn't been properly characterized. The primary ones are the noise in the detector and the noise in the illumination source. These two sources of noise will be the major contributor to the image quality. This leads to unexplored work for characterizing various aspects of image quality. These includes identifying the resolvable resolution for each optics configuration, the resolvable fluorescence lifetime and DOCI value resolution, the signal-to-noise threshold to ensure that noise is not interfering with the final results, and the net effect of all other sources of noise in the final DOCI image after several arithmetic operations. Furthermore, once the DOCI system is transitioned into *in vivo* imaging, methods for quantifying motion noise and ambient noise should also be considered.

9.4 Illumination Source

One of the major accomplishments of the project is to be able to reproduce the illumination pulse profile. However, there are still a few flaws with the existing illumination pulse shape. The largest flaw is the oscillatory response in the steady state of the illumination pulse width. This is an issue that may detract the results from the derived theoretical models. A secondary flaw would be the long rise and fall time of the illumination source. Although a model was derived to compensate for this issue, the multi-exponential model does result in less-intuitive explanation of the contrast information where quadratic information is present. Other improvements that can be made to the circuit is to maximize the optical power of the illumination source to ensure the optimal signal-to-noise, which can greatly reduce the exposure time needed to obtain each DOCI image.

9.5 Progress of Surgery

The current progress of can be quickly summarized into three distinct epoch across history, starting with open surgery [78]. Advancements in surgery led to developments laparoscopic and minimally invasive procedures; and more recently robotic and remote surgery [79, 80]. Figure 9.2 shows a research robotic surgical platform and the progression of surgery.

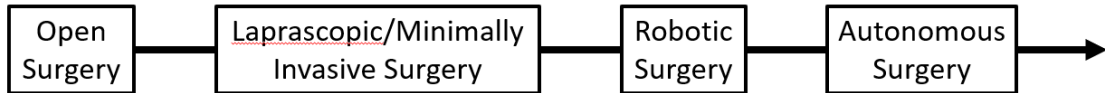


Figure 9.2: (*top*) Intraocular robotic interventional and surgical system (IRISS) a pseudo-automated cataract robotic surgery and (*bottom*) progression of surgery.

One common denominator in many medical technology advancement is an ever increasing cost for the cutting edge therapies. In some robotic surgery cases, advance technology and higher cost may not always lead to improved patient outcomes [81]. A side project to this thesis was pioneering research on automating sub-tasks in a cataract surgery, specifically the phacoemulsification. One motivation to automating surgery is being able to have one surgeon operate on multiple patient simultaneously to reduce healthcare cost and address clinician shortage across the world [82, 83]. The Intraocular robotic interventional and surgical system (IRISS) project is a project that tries to advance automation and surgical technology, but many challenges in the sensing and recognition have prohibit further progress. Conceptually, for autonomous surgery to progress in the future, robust imaging technologies for tissue differentiation is a prerequisite to allow surgical robots to sense the environment before performing the tasks. The DOCI project and the purpose of this thesis is to provide a prospective framework to enable the development of various translational research biophotonics imaging tools that can assist in tissue differentiation.

APPENDIX A

Appendix - Theory

A.1 main idealModel function

```
clear all; close all; clc;
t = [0:.1:100];
uR = ones(1,length(t));
c = 50;
uR(t<c) = 0;
tal = 5;
a = 1/tal;
y = (exp(-a*t)/a^2-1/a^2+t/a) - (exp(-(t-c)*a)/a^2-1/a^2+(t-c)/a).*uR;
normFigure(0,.1,.5,.5)
plot(t,y); hold on;
xshift = -2;
yshift = -70;
fontsize = 14;
text((15-0)/2+xshift,125+yshift,'R1','FontSize',fontsize)
text((50-15)/2+15+xshift,125+yshift,'R2','FontSize',fontsize)
text((65-50)/2+50+xshift,125+yshift,'R3','FontSize',fontsize)
text((100-65)/2+65+xshift,125+yshift,'R4','FontSize',fontsize)

rect = zeros(1,length(t));
decay = exp(-t/a);
```

```

rect(t<c) = 1;
y2 = conv(decay,rect);
y2 = y2(1:length(t));
for i = 1:length(y2)
    y_sum(i) = sum(y(1,i));
end
plot(t(1:10:end),y_sum(1:10:end),'.')
legend({'Closed_Form_Solution','Simulated_Convolution_Model'})

plot([15 15],[0 250],'k');
plot([50 50],[0 250],'k');
plot([65 65],[0 250],'k');
xlabel('time(ns)');
set(gca,'ytick',[0 250],'yticklabel',{'0','1'})
% set(gca,'xtick',[0 10 20 30 35 40 50 60 70 80 90 100],'xticklabel
    ↪ ',{'0','10','20','30','C-B''40','C','60','70','C+B
    ↪ ', '80','90','100'})
ylabel('Normalized_q(t)');
title('q(t), \tau=5ns, C=50ns');

fig = gcf;
fig.PaperPositionMode = 'auto';
print('q','-dpng','-r0')

```

A.2 main parameterEffect function

```
clear all; close all; clc;
```

```

B = 24;
C = 80;
x = [0:.1:200];
y = zeros(1,length(x));

tau = 1.62;
tau_ill = 4.9;

y(x>=C) = 1;
% plot(x,y)
a = 1/tau;
d = 1/tau_ill;

% for i = 1:length(x)
% out(i) = q(x(i),y(i),a,d,C);
% end
TAU = [0:.1:8];
for i = 1:length(TAU)
    a = 1/TAU(i);
    doci(i) = (q(C+B,y(find(x==C+B)),a,d,C)-q(C,y(find(x==C)),a,d,C))/(q(C,y
        ↪ (find(x==C)),a,d,C)-q(C-B,y(find(x==C-B)),a,d,C));
    ideal(i) = (TAU(i)+tau_ill)/B;
    beta(i) = exp(-a*B)/a^2+exp(-d*B)/d^2;
end
normFigure(0,.1,.5,.9);
subplot(2,1,1); hold on;
plot(TAU,ideal);
plot(TAU,doci);
xlabel('Fluorophore Decay \tau (ns)', 'FontSize',16);

```

```

ylabel('DOCi value (A.U.)', 'FontSize', 16);
title('DOCi Example, \tau_{exc}= 4.1ns, C = 80ns, B=24ns', 'FontSize', 16);
legend({'Linear Model', 'Insufficient Integration Time'}, 'Location', '
    ↪ NorthWest', 'FontSize', 16);

residual = abs(ideal-doci);
subplot(2,1,2);
[hAx,hLine1,hLine2] = plotyy(TAU,abs(ideal-doci),TAU,log10(beta));
title('Deviation from linear model', 'FontSize', 16);
xlabel('Fluorophore Decay \tau (ns)', 'FontSize', 16);
ylabel(hAx(1), 'Residual', 'FontSize', 16);
ylabel(hAx(2), '\beta', 'FontSize', 16);
set(hAx(1), 'YTick', [0:.01:.05], 'ylim', [0, .05]); box(hAx(1), 'off')
annotation('textarrow', [.182 .15], [.16 .13], 'String', sprintf('%1.2E',
    ↪ residual(2)), 'FontSize', 16)
grid on
set(hAx(2), 'YTick', log10([.01, .05, .1, .5, 1, 5, 10]), 'YTickLabel
    ↪ ', [.01, .05, .1, .5, 1, 5, 10], 'ylim', [-2 1], 'Ygrid', 'on')
fig = gcf;
fig.PaperPositionMode = 'auto';
print('doci_insufficient', '-dpng', '-r0')

```

APPENDIX B

Appendix - Calibration

B.1 main FLIM function

```
%% Single Dye Lifetime Calculator
%Calculates the lifetime of a single dye obtained from oscilloscope & laser
%set up
%Loads a single laser pulse and a single pulse from the dye
%Convolve the laser pulse with computer generated exponential decay
%Check for best fitting approximation

%Displays plot of laser, dye, and calculated convolution (non-aligned) and
    ↪ bin area of
%comparison with peaks set at 10th point
%Output values of Lifetime(ns), Binwidth(ns),
%and Error over binwidth (A.U).
clear;clc; clf; clear all; close all;
laser_files = [0:4];
fluor_files = [20:24];
data = [];
idx = 1;
for i = 1:length(laser_files)
    if(laser_files(i)<10)
```

```

    file_laser = strcat('C1laser0000',num2str(laser_files(i)));% Select
        ↪ laser file name(change only # 'C1laser#####')
else
    file_laser = strcat('C1laser000',num2str(laser_files(i)));% Select
        ↪ laser file name(change only # 'C1laser#####')
end
for j = 1:length(fluor_files)
    [i j]
    if(fluor_files(j)<10)
        file_dye = strcat('C1laser0000',num2str(fluor_files(j)));% Select
            ↪ laser file name(change only # 'C1laser#####')
    else
        file_dye = strcat('C1laser000',num2str(fluor_files(j)));% Select
            ↪ dye file name(change only # 'C1laser#####')
    end
    [Lifetime, t, predicted, dye, laser, peak, width] = analyzeDye(
        ↪ file_laser,file_dye);
    data(idx) = Lifetime;
    idx = idx+1;
end
end
save('flim_d.mat','data')
mean(data)
std(data)
%% Plot best curves and measuring area
close all;
normFigure(0,0,1,1);
%Top subplot displaying the laser, dye, and convolution profiles
%t is multiplied by 109 to adjust from s to ns

```

```

% subplot(2,1,1);
hold on;
plot(t*10^9,laser,'r');
plot(t*10^9,dye,'og');
plot(t*10^9,predicted,'b');
legend({'laser excitation','dye measurement','predicted model'},'FontSize
    ↪ ',20);
title('Pulse Profiles','FontSize',20);
xlabel('Time(ns)','FontSize',20);
ylabel('Intensity(A.U.)','FontSize',20);
axis tight;
hold off;

fig = gcf;
fig.PaperPositionMode = 'auto';
print('algorithm','-dpng','-r0')

% %Bottom subplot displaying the dye and convolution over the width of the
% %measuring bins
% subplot(2,1,2); hold on;
% plot(t(peak+1:peak+width)*10^9,predicted(peak+1:peak+width),'b');
% plot(t(peak+1:peak+width)*10^9,dye(peak+1:peak+width),'r');
% legend('predicted','measured');
% title('Measuring Bin Area (aligned)');
% xlabel('Time(ns)');
% ylabel('Intensity(A.U.)');
% axis tight;
% hold off;

```

```

%% % Display the Lifetime(ns), Binwidth(ns), and error[A.U.] in command
    ↪ window
%% %factor of 109 is to change from s to ns
%% format short e
%% disp(strcat('Lifetime(ns):',num2str(Lifetime*109)))

```

B.2 analyzeDye function

```

function [Lifetime, t, predicted, dye, laser, peak,width] = analyzeDye(
    ↪ laserfile,dyefile)
% Set width of decay measuring area (begins immediately after peak) [#
    ↪ of points]
width = 15; %[#]
%Create lifetime range to test for conv. in ns
minlife= 1; %Shortest lifetime to test [ns]
maxlife= 10; %Longest lifetime to test [ns]
lifetimestep=0.1; %Precision of lifetime range [ns]

%Set cutoff lengths around data
peak = 20; %Set location of maximum (removing points before)
tail = 120; %Set points after peak to keep
%Generates lifetime array to be tested
nT = (maxlife-minlife)/lifetimestep+1;
T = linspace (minlife*10-9,maxlife*10-9,nT);

%% Load files and timestep
laserload = xlsread(strcat(laserfile,'.csv')); %Select and Load laser
    ↪ pulse file

```

```

dyeload = xlsread(strcat(dyefile, '.csv')); %Load dye file
laserload(:,1:2) = []; %Removes non-data cells
dyeload(:,1:2) = []; %Removes non-data cells
dt = laserload(2,1)-laserload(1,1); %Time steps from sensor

%% Reformat and remove excess data
%Remove excess data from before laser pulse and reformat
laser = zeros(length(laserload),1); %Create array for laser
laser = laserload(:,2); %Separate amplitude data from laserload file
[maxlaser,maxlaserloc] = max(laser); %Finds peak of laser
laser(1:maxlaserloc-peak) = []; %Removes excess front end points on
    ↪ laser (max at 10)
laser(peak+tail:length(laser)) = []; %Removes excess trailing data
    ↪ points from laser (after tail)
laser = laser/maxlaser; %Normalize laser to max of 1

% Interpolates dye to lasertime offset, reformats and removes excess
    ↪ data
dye = dyetimecorrect(dyeload,laserload,dt); %spline interpolation of
    ↪ dye onto laser time frame (corrects substep offset)
[maxdye,maxdyeloc] = max(dye); %Finds peak of dye
dye(1:maxdyeloc-peak) = []; %Removes excess front end points on dye (max
    ↪ at 10)
dye(peak+tail:length(dye)) = []; %Removes excess trailing data points
    ↪ from dye (after tail)
dye=dye/maxdye; %Normalize dye to 1 amplitude

%% Create standard time space
n = peak+tail-1; %Length of cleaned data

```

```

t = linspace(0,dt*(n-1),n); %Time space for sensor
texperimental = linspace(0,dt*(2*n-1),2*n-1); %Time space of convolution

%% Initiate predicted arrays
%Initiate 0 arrays
decay = zeros(n,1); %Initiates exponential decay array
difference = zeros(nT,1); %Initiates total error between predicted and
    ↪ measured array

%% Run the simulation and plot
for k = 1:nT
    decay = exp(-t/T(k)); %Create exponential decay
    predicted(1:2*n-1,1) = conv(laser,decay); %Convolve decay and laser
        ↪ pulse
    [maxpredicted,maxpredictedloc]=max(predicted); %Find max location of
        ↪ predicted convolution for start of decay behavior
    predicted=predicted/maxpredicted; %Normalize convolution to 1
        ↪ amplitude
    separation(1:width) = (dye(peak+1:peak+width) - predicted(
        ↪ maxpredictedloc+1:maxpredictedloc+width)).^2; %Square of the
        ↪ difference at each point
    difference(k) = sum(separation); %Sum the difference for each
        ↪ predicted curve
end
%Find minimum errors and locations
[min_diff,I] = min(difference); %Find minimum error for best lifetime T(
    ↪ I)

%% Use best values to create a plot for comparison

```

```

%Clear decay and convolution arrays
decay = zeros(n,1); %Clear exponential decay curve for convolution
predicted = zeros(2*n-1,1); %Clear predicted curve

Lifetime = T(I); %Use Identified lifetime

%Simulate with best lifetime
decay(:,1) = exp(-t/Lifetime); %Create exponential decay
predicted = conv(laser,decay); %Convolve best decay with laser pulse
[maxpredicted,maxpredictedloc]=max(predicted); %Find max location of
    ↪ predicted convolution for start of decay behavior
predicted(1:maxpredictedloc-peak) = []; %Removes excess front end points
    ↪ on predicted (max at 10)
predicted(peak+tail:length(predicted)) = []; %Removes excess trailing
    ↪ data points from predicted (after tail)
predicted=predicted/maxpredicted; %Normalize convolution to 1 amplitude
end
function s=dyetimecorrect(dyeload,laserload,dt)
    a= dt*((floor(dyeload(1,1)/dt)-dyeload(1,1)/dt)); %Determines time
        ↪ offset of dye
    b= dt*((floor(laserload(1,1)/dt)-laserload(1,1)/dt)); %Determines time
        ↪ offset of laser
    adjust= b-a; %Calculates difference in offsets
    t= dyeload(:,1)-adjust; %Shifts time of dyel
    s=spline(dyeload(:,1),dyeload(:,2),t); %Cubic interpolation of dye
        ↪ signal onto corrected time
end

```

B.3 main FLIM vs DOCi function

```
clear all; close all; clc;
dyes = {'r','f','p','d'};

fig = [1 1 1 1];
if(fig(1))
    %Show Dye Lifetimes
    fig1 = normFigure(0,.1,.5,.7); hold on;
    for i = 1:length(dyes)
        file_flim = strcat('flim_',dyes{i},'.mat');
        load(file_flim);
        data = data*1E9;
        scatter(i*ones(size(data)),data, 'c.', 'jitter','on', 'jitterAmount
            ↪ ', 0.05);
        errorbar(i,mean(data),std(data),'k');
        plot(i,mean(data),'k. ');
        flim_mean(i) = mean(data);
        flim_std(i) = std(data);
        str = strcat(num2str(sprintf('%0.3f',mean(data))),char(177),num2str(
            ↪ sprintf('%0.3f',std(data))));
        text(i-.3, mean(data)+std(data)+1,str,'FontSize',14)
    end
    axis([.5 4.5 0 10])
    xlabel('Dyes','FontSize',18)
    ylabel('Lifetimes (ns)','FontSize',18);
    fig1.Children.XTick = [1:4];
    fig1.Children.XTickLabel = {'Rhodamine','Fluorescein','Perylene','DPA'};
    title('Lifetime Extraction of Dyes','FontSize',18);
```

```

grid on;

fig0 = gcf;
fig0.PaperPositionMode = 'auto';
print('flim_comp','-dpng','-r0')
end

if(fig(2))
    fig2 = normFigure(0,.1,.5,.7); hold on;
    for i = 1:length(dyes)
        file_doci = strcat('doci_',dyes{i},'.mat');
        load(file_doci);
        meanVal = mean(data1);
        stdVal = std(data1);
        doci_mean(i) = meanVal;
        doci_std(i) = stdVal;
        [h,bin] = hist(data1,[0:.001:.5]);
        plot(bin,h)

        [val idx] = max(h);
        if(i<3)
            text(bin(idx)-.1,val, strcat(sprintf('%0.4f',mean(data1)),char
                ↪ (177),sprintf('%0.4f',std(data1))), 'FontSize',15)
        else
            text(bin(idx)+.01,val, strcat(sprintf('%0.4f',mean(data1)),char
                ↪ (177),sprintf('%0.4f',std(data1))), 'FontSize',15)
        end
    end
% data = data*1E9;

```

```

% scatter(i*ones(size(data)),data, 'c.', 'jitter','on', 'jitterAmount',
    ↪ 0.05);
% errorbar(i,mean(data),std(data),'k');
% plot(i,mean(data),'k. ');

% str = strcat(num2str(sprintf('%0.3f',mean(data))),char(177),num2str(
    ↪ sprintf('%0.3f',std(data))));
% text(i-.3, mean(data)+std(data)+1,str,'FontSize',14)
    end
    legend({'Rhodamine','Fluorescein','Perylene','DPA'},'FontSize',14)
    xlabel('DOCi value (A.U.)','FontSize',18)
    ylabel('Occurences (>1000)','FontSize',18)
    title('DOCi values of Dyes','FontSize',18);
    set(gca,'ytick',[0 5E5],'yticklabel',{'},'xtick',[0:.02:.5])
    grid on;

    fig0 = gcf;
    fig0.PaperPositionMode = 'auto';
    print('doc_i_comp','-dpng','-r0')
end
%%
close all;
if(fig(3))
    fig3 = normFigure(0,.1,.5,.5); hold on;
    plot(flim_mean,doci_mean,'o')
    p = polyfit(flim_mean,doci_mean,1);
    h1 = errorbar(flim_mean,doci_mean,doci_std,'co')
    h2 = herrorbar(flim_mean,doci_mean,flim_std,'co')
    xlabel('Lifetime (ns)','FontSize',16);

```

```

        ylabel('DOCi Value (A.U.)','FontSize',16);
end
if(fig(4))
% info = imfinfo('pulse1.tif');
% N = numel(info);
% for i = 1:N
% i
% off = imread('pulse1.tif',i);
% pulse = imread('pulse2.tif',i);
% img = pulse-off;
% curve0(i) = mean(mean(img(100:900,400:700)));
% end
    load('curve0.mat');
    t0 = [0:length(curve0)-1];
    t1 = [0:.25:max(t0)];
    t2 = [0:.25:400];

    curve1 = interp1(t0,curve0,t1,'spline');
    lt = [.25:.25:10];
    for i = 1:length(lt)
        a = exp(-t1./lt(i)); a = a/max(a);
        b = conv(curve1,a); b = b/max(b); b = b(1:length(b)/2);
        integ_decay = trapz(b(t2>=107 & t2<107+40));
        integ_steady = trapz(b(t2<107 & t2>=107-40));
        doci(i) = integ_decay/integ_steady;
    end
    fit = polyval(p,lt);
    h3 = plot(lt,doci)
    h4 = plot(lt,fit)

```

```
h5 = plot([1.58 4.1 4.63 7.02],([1.58 4.1 4.63 7.02]+4.47)/40,'o')
legend([h1 h5 h3 h4],{'Experimental','Theoretical','Simulated','Fitted
    ↪'},'FontSize',16,'Location','NorthWest')
fig0 = gcf;
fig0.PaperPositionMode = 'auto';
print('full_comp','-dpng','-r0')
end
```

APPENDIX C

Appendix - SIFT Implementation

C.1 main checkRaw function

```
%For DOCi 3.0, uses SIFT motion correct
clearvars -except folderPath;
% clear all;
close all; clc;
addpath('functionsV3')
format short g

motion = 1;
if(~exist('folderPath'))
    folderPath = uigetdir(strcat(getDBPath,'DOCi 3.0\Trial\'));
    folderPath = strcat(folderPath,'\');
end
% BGPath = strcat(getDBPath,'DOCi 3.0\Trial\2017_06_07 01.03.38PMBG\');
% BGPath = strcat(getDBPath,'DOCi 3.0\Trial\2017_05_14 05.52.02PM BG\');
BGPath = strcat(getDBPath,'DOCi 3.0\Trial\2017_05_19 01.51.51PMBG\');
rgb = generateRGB3(folderPath,BGPath,motion);
%%
filt = {'uv' '407' '434' '465' '494' '520' '542' '572' '605' '632' '676'};
% filt = {'uv' '405' '434' '465' '494' '520' '542' '572' '605' '676'};
scaler = 1.2;
```

```

shiftX = 0;
shiftY = .01;
deltaX= .01;
deltaY = 0;
normFigure(0,0,.7,1);
h = subplot(3,4,1);
p = get(h,'pos');
p(3:4) = p(3:4)*scaler;
p = p-[0 shiftY 0 0]; set(h,'pos',p);
imshow(rgb);
axis off; title('rgb','FontSize',16);

for i = 1:length(filt)
    dyRange(i).val = [0 1];
% dyRange(1).val = [0 1];
% dyRange(2).val = [.4 .7];
% dyRange(3).val = [.2 .6];
% dyRange(4).val = [.3 .6];
% dyRange(5).val = [.4 .7];
% dyRange(6).val = [.5 .9];
% dyRange(7).val = [.5 .9];
% dyRange(8).val = [.5 .9];
% dyRange(9).val = [.5 1];
% dyRange(10).val = [.5 1];
% dyRange(11).val = [.5 1];
% % dyRange(i).val = [0 .8];
% dyRange(1).val = [0 .8];
% dyRange(2).val = [.4 .7];
% dyRange(3).val = [.2 .8];

```

```

% dyRange(4).val = [.5 .9];
% dyRange(5).val = [.4 .7];
% dyRange(6).val = [.5 .9];
% dyRange(7).val = [.5 .9];
% dyRange(8).val = [.5 .9];
% dyRange(9).val = [.5 1];
% dyRange(10).val = [.5 1];
% dyRange(11).val = [.5 1];

filt{i}
lt = generateLT(folderPath,BGPath,filt{i},motion);
j = i;
figure(2);
h(j+1)= subplot(3,4,j+1); p(j+1,:) = get(h(j+1),'pos');

p(j+1,:) = p(j+1,:)-[deltaX 0 0 0]*mod(j,4)-[shiftX 0 0 0]; %x-shift
p(j+1,:) = p(j+1,:)+[0 deltaY 0 0]*floor(j/4)-[0 shiftY 0 0]; %y-shift
p(j+1,:) = p(j+1,:).*[1 1 scaler scaler]; %scaling

set(h(j+1),'pos',p(j+1,:))
imagesc(lt); hold on; axis off; axis image; colormap(jet); caxis(dyRange
    ↪ (i).val); %colorbar; %normal .6-1
title(filt{j},'FontSize',16);
% save(strcat(folderPath,filt{j},'_x3BG.mat'),'lt');
% if(0)
% %elastin
% elastin = reshape(lt(654:720,283:353),1,[]);
% %collagen
% lt(611:683,593:681);

```

```

% collagen = reshape(lt(611:683,593:681),1,[]);
%
% figure;
% [count,pos] = hist(elastin,100);
% [count2,pos2] = hist(collagen,100);
% plot(pos,count/max(count)); hold on;
% plot(pos2,count2/max(count2));
% legend('Elastin','Collagen')
% title(num2str(i))
% end
    pause(.01);
end

figure(2)
savename = strcat(folderPath(end-21:end-1),'.png');
saveas(gca,savename)

```

C.2 generateRGB function

```

function rgb = generateRGB(folderPath,BGPath,motion)
    if(nargin > 2)
        if(motion)
            run(strcat(getGDPath,'Work\MATLAB\vlfeat-0.9.20-bin\vlfeat
                ↪ -0.9.20\toolbox\vl_setup'))
        end
    end
    r = loadImg(folderPath,BGPath,'r*.tif');
    g = loadImg(folderPath,BGPath,'g*.tif');

```

```

b = loadImg(folderPath,BGPath,'b*.tif');
r = r/max(max(r));
g = g/max(max(g));
b = b/max(max(b));
if(nargin > 2)
    if(motion)
        mod_g = motionCorrect(r,g,.95,0);
        mod_b = motionCorrect(mod_g,b,.95,0);
    else
        mod_g = g;
        mod_b = b;
    end
else
    mod_g = motionCorrect(r,g,.95,0);
    mod_b = motionCorrect(mod_g,b,.95,0);
end
amp = 1;
correctedrgb = cat(3,r,mod_g,mod_b)*amp;
rgb = cat(3,r,g,b)*amp;
% normFigure
% subplot(1,2,1);
% imshow(rgb); title('No Motion Correct')
% subplot(1,2,2);
% imshow(correctedrgb); title('Motion Corrected')
    rgb = correctedrgb;
end

function I = loadImg(folderPath,BGPath,imgType)
    filename = dir(strcat(folderPath,imgType));

```

```

    filenameBG = dir(strcat(BGPath,imgType));
% filenameBG.name
    I = imread(strcat(folderPath,filename.name));
    Ibg = imread(strcat(BGPath,filenameBG.name));

% I = medfilt2(I,[6 6]);
% Ibg = medfilt2(Ibg,[6 6]);
% I = medfilt2(I-Ibg,[6 6]);
    I = I-Ibg;
    I = single(I);
end

```

C.3 generateLT function

```

function mod_lt = generateLT(folderPath,BGPath,filt,motion)
    I1 = loadImg(folderPath,BGPath,'_x1*.tif',filt);
    'I1 loaded'
    I2 = loadImg(folderPath,BGPath,'_x2*.tif',filt);
    'I2 loaded'

% I1 = loadImg(folderPath,folderPath,'_x1*.tif',filt);
% I2 = loadImg(folderPath,folderPath,'_x2*.tif',filt);
    nargin
    if(nargin > 3)
        if(motion)
            mod_I2 = motionCorrect(I1,I2,.9,0,filt);
        else
            mod_I2 = I2;
        end
    end

```

```

        end
    else
        mod_I2 = motionCorrect(I1,I2,.9,0,filt);
    end

% normFigure;
% [y1 x1] = histcounts(I1(521:688,499:618),[0:1000]);
% x11 = (x1(1:end-1)+x1(2:end))/2;
% plot(x11,y1); hold on;
% [y2 x2] = histcounts(mod_I2(521:688,499:618),[0:1000]);
% x12 = (x2(1:end-1)+x2(2:end))/2;
% plot(x12,y2); hold on;
% legend('I1','I2');

    lt = I2./I1;
% lt = imgaussfilt(lt,[5 5]);
    mod_lt = mod_I2./I1;
    mod_lt = imgaussfilt(mod_lt,[3 3]);
    mod_lt(isnan(mod_lt)) = 0;
    mod_lt(mod_lt>1) = 0;
% mod_lt(I1<1000) = 0;
% normFigure;
% [y3 x3] = histcounts(mod_lt(521:688,499:618),[0:.005:1]);
% x33 = (x3(1:end-1)+x3(2:end))/2;
% plot(x33,y3); hold on;
% % normFigure
% subplot(1,2,1); imshow(lt); colormap(jet)
% subplot(1,2,2); imshow(mod_lt); colormap(jet)

```

```

% %For Collagen Elastin
% %elastin
% filt
% mean(reshape(I1(654:720,283:353),1, []))
% mean(reshape(mod_I2(654:720,283:353),1, []))
%
% %collagen
% mean(reshape(I1(611:683,593:681),1, []))
% mean(reshape(mod_I2(611:683,593:681),1, []))
end

function I = loadImg(folderPath,BGPath,imgType,filt)
    filename = dir(strcat(folderPath,strcat(filt,imgType)));
    filenameBG = dir(strcat(BGPath,strcat(filt,'_x3*.tif')));
% filenameBG = dir(strcat(BGPath,strcat(filt,imgType)));
% filenameBG.name
    I = imread(strcat(folderPath,filename.name));
% size(I)
    Ibg = imread(strcat(BGPath,filenameBG.name));

% I = medfilt2(I,[6 6]);
% Ibg = medfilt2(Ibg,[6 6]);
% Ibg = mean(mean(Ibg))
% Ibg = 580;
% I = medfilt2(I-Ibg,[6 6]);
    I = single(I-Ibg);
    I = medfilt2(I,[3 3]);
% I = imgaussfilt(I,[5 5]);

```

```

% I = single(I);
% figure;
% imagesc(I);title(imgType)
% figure;
% imagesc(Ibg)
end

```

C.4 motionCorrect function

```

function I = motionCorrect(ref,mod,perc,peak_thresh,filt)
    [ref_f,ref_d] = vl_sift(ref, 'PeakThresh', peak_thresh);
    [mod_f,mod_d] = vl_sift(mod, 'PeakThresh', peak_thresh);
% length(ref_f)
% length(mod_f)
    if(~(length(ref_f)<1 | length(mod_f)<1))
        refmod = [ref mod];
        [matches,scores] = vl_ubcmatch(ref_d,mod_d);
        ref_sel = matches(1,:);
        mod_sel = matches(2,:);

        %Extra to see how thigns matched
        mod_f2 = mod_f;
        mod_f2(1,:) = mod_f(1,:)+1024;
        %----end Extra

        x1 = ref_f(1,matches(1,:));
        y1 = ref_f(2,matches(1,:));
        x2 = mod_f(1,matches(2,:));

```

```

y2 = mod_f(2,matches(2,:));

%First Filtering Method %Percentage Thresholding
if(0)
    dx = (x2-1024)-x1;
    dx
    x2-x1
    dy = y2-y1;
    %Filtering Matching
    matchDisp = sqrt(dx.^2+dy.^2);
    p_tile = floor(length(matchDisp)*perc);
    sorted_matchDisp = sort(matchDisp);
    max_matchDisp = sorted_matchDisp(p_tile);
    %End matching Filter

    loc = find(matchDisp<=max_matchDisp);
    x1 = x1(loc); x2 = x2(loc);
    y1 = y1(loc); y2 = y2(loc);
end

%Second Filtering Method
if(1)
    distance_thresh = 100;
    dx = x2-x1;
    largeDX = find(abs(dx)>distance_thresh);
    x1(largeDX) = [];
    x2(largeDX) = [];
    y1(largeDX) = [];
    y2(largeDX) = [];

```

```

dy = y2-y1;
largeDY = find(abs(dy)>distance_thresh);
x1(largeDY) = [];
x2(largeDY) = [];
y1(largeDY) = [];
y2(largeDY) = [];

dx = x2-x1;
dy = y2-y1;
matchDisp = sqrt(dx.^2+dy.^2);
% length(matchDisp)
p_tile = floor(length(matchDisp)*perc);
% min(p_tile)

sorted_matchDisp = sort(matchDisp);
max_matchDisp = sorted_matchDisp(p_tile);
%End matching Filter

loc = find(matchDisp<=max_matchDisp);
x1 = x1(loc); x2 = x2(loc);
y1 = y1(loc); y2 = y2(loc);
end

%Extra to see how things match
x = [x1;x2+1024];
y = [y1;y2];

%Check how features are matched
if(0)

```

```

f1 = figure;
set(f1, 'Position', [100, 100, 1800, 800]);
imagesc(refmod); hold on; caxis([2000 30000])
h1 = vl_plotframe(ref_f(:,ref_sel)) ;
set(h1,'color','y','linewidth',2);
h2 = vl_plotframe(mod_f2(:,mod_sel)) ;
set(h2,'color','y','linewidth',2);
plot(x,y); axis off;
if(nargin > 4)
    filt
    title(strcat('Img1 & Img2 ', filt));
else
    title('Img1 & Img2');
end
pause(1);
end
%End Extra

% size(x2)
% size(x1)
[mod_tform,inlierPtsDistorted,inlierPtsOriginal] = ...
estimateGeometricTransform([x2;y2]',[x1;y1]',...
'similarity');

% estimateGeometricTransform([x2;y2]',[x1;y1]',...
%'affine');

I = imwarp(mod,mod_tform,'OutputView',imref2d(size(ref)));
else
    I = mod;

```

```
    end
end
```

APPENDIX D

Other

Contact Harrison Cheng for other software implementations.

REFERENCES

- [1] Asael Papour. *Analysis and Optimization of a Lifetime Fluorescence System to Detect Structural Protein Signatures in Varying Host Mediums for Rapid Biomedical Imaging*. PhD thesis, University of California, Los Angeles, 2012.
- [2] Yang Pu, Wubao Wang, Guichen Tang, and Robert R. Alfano. Changes of collagen and nicotinamide adenine dinucleotide in human cancerous and normal prostate tissues studied using native fluorescence spectroscopy with selective excitation wavelength. *Journal of Biomedical Optics*, 2010.
- [3] Brian C Drolet, Nancy M Lorenzi, and And Nashville. *Translational research: understanding the continuum from bench to bedside*. 2011.
- [4] Pablo A Valdés, David W Roberts, Fa-Ke Lu, and Alexandra Golby. *Optical technologies for intraoperative neurosurgical guidance* HHS Public Access.
- [5] Guolan Lu and Baowei Fei. Medical hyperspectral imaging: a review. *Journal of Biomedical Optics*, 19(1):010901, 1 2014.
- [6] Sylvain Gioux, Soo Choi, and John V Frangioni. *Image-Guided Surgery Using Invisible Near-Infrared Light: Fundamentals of Clinical Translation*.
- [7] Alexander L. Vahrmeijer, Merlijn Hutteman, Joost R. van der Vorst, Cornelis J. H. van de Velde, and John V. Frangioni. Image-guided cancer surgery using near-infrared fluorescence. *Nature Reviews Clinical Oncology*, 10(9):507–518, 9 2013.
- [8] Stijn Keereweer, Jeroen D F Kerrebijn, Pieter B A A Van Driel, Bangwen Xie, Eric L Kaijzel, Thomas J A Snoeks, Ivo Que, Merlijn Hutteman, Joost R Van Der Vorst, J Sven, D Mieog, Alexander L Vahrmeijer, Cornelis J H Van De Velde, Robert J Baatenburg De Jong, and Clemens W G M Löwik. Optical Image-guided Surgery-Where Do We Stand? *Mol Imaging Biol*, 13:199–207, 2011.
- [9] Douglas L. Heintzelman, Urs Utzinger, Holger Fuchs, Andres Zuluaga, Kirk Gossage, Ann M. Gillenwater, Rhonda Jacob, Bonnie Kemp, and Rebecca R. Richards-Kortum. Optimal Excitation Wavelengths for In Vivo Detection of Oral Neoplasia Using Fluorescence Spectroscopy ¶. *Photochemistry and Photobiology*, 72(1):103–113, 5 2007.
- [10] Ekaterina Svistun, Reza Alizadeh-Naderi, Adel El-Naggar, Rhonda Jacob, Ann Gillenwater, and Rebecca Richards-Kortum. Vision enhancement system for detection of oral cavity neoplasia based on autofluorescence. *Head & Neck*, 26(3):205–215, 3 2004.
- [11] Ann Gillenwater, Rhonda Jacob, Ravi Ganeshappa, Bonnie Kemp, Adel K. El-Naggar, J. Lynn Palmer, Gary Clayman, Michele Follen Mitchell, and Rebecca Richards-Kortum. Noninvasive Diagnosis of Oral Neoplasia Based on Fluorescence Spectroscopy and Native Tissue Autofluorescence. *Archives of OtolaryngologyHead & Neck Surgery*, 124(11):1251, 11 1998.

- [12] Ann Gillenwater, Rhonda Jacob, and Rebecca Richards-Kortum. Fluorescence spectroscopy: A technique with potential to improve the early detection of aerodigestive tract neoplasia. *Head & Neck*, 20(6):556–562, 9 1998.
- [13] Rebekah Drezek, Konstantin Sokolov, Urs Utzinger, Iouri Boiko, Anais Malpica, Michele Follen, and Rebecca Richards-Kortum. Understanding the contributions of NADH and collagen to cervical tissue fluorescence spectra: Modeling, measurements, and implications. *Journal of Biomedical Optics*, 6(4):385, 2001.
- [14] Konstantin Sokolov, Michele Follen, Jesse Aaron, Ina Pavlova, Anais Malpica, Reuben Lotan, and Rebecca Richards-Kortum. Real-time vital optical imaging of precancer using anti-epidermal growth factor receptor antibodies conjugated to gold nanoparticles. *Cancer research*, 63(9):1999–2004, 5 2003.
- [15] Rebecca Richards-Kortum and Eva Sevick-Muraca. QUANTITATIVE OPTICAL SPECTROSCOPY FOR TISSUE DIAGNOSIS. *Annual Review of Physical Chemistry*, 47(1):555–606, 10 1996.
- [16] Kristine E. Day, Larissa Sweeny, Brian Kulbersh, Kurt R. Zinn, and Eben L. Rosenthal. Preclinical Comparison of Near-Infrared-Labeled Cetuximab and Panitumumab for Optical Imaging of Head and Neck Squamous Cell Carcinoma. *Molecular Imaging and Biology*, 15(6):722–729, 12 2013.
- [17] Juergen Scheidler, Hedvig Hricak, Daniel B. Vigneron, Kyle K. Yu, Dahlia L. Sokolov, L. Royal Huang, Charles J. Zaloudek, Sarah J. Nelson, Peter R. Carroll, and John Kurhanewicz. Prostate Cancer: Localization with Three-dimensional Proton MR Spectroscopic ImagingClinicopathologic Study. *Radiology*, 213(2):473–480, 11 1999.
- [18] Matthew D. Rifkin, Elias A. Zerhouni, Constantine A. Gatsonis, Leslie E. Quint, David M. Paushter, Jonathan I. Epstein, Ulrike Hamper, Patrick C. Walsh, and Barbara J. McNeil. Comparison of Magnetic Resonance Imaging and Ultrasonography in Staging Early Prostate Cancer. *New England Journal of Medicine*, 323(10):621–626, 9 1990.
- [19] D J Rubens, M A Hadley, S K Alam, L Gao, R D Mayer, and K J Parker. Sonoelasticity imaging of prostate cancer: in vitro results. *Radiology*, 195(2):379–83, 5 1995.
- [20] J.S.P. YUEN, C.H. THNG, P.H. TAN, L.W. KHIN, S.J.L. PHEE, D. XIAO, W.K.O. LAU, W.S. NG, and C.W.S. CHENG. ENDORECTAL MAGNETIC RESONANCE IMAGING AND SPECTROSCOPY FOR THE DETECTION OF TUMOR FOCI IN MEN WITH PRIOR NEGATIVE TRANSRECTAL ULTRASOUND PROSTATE BIOPSY. *The Journal of Urology*, 171(4):1482–1486, 4 2004.
- [21] E.C. Fear, S.C. Hagness, P.M. Meaney, M. Okoniewski, and M.A. Stuchly. Enhancing breast tumor detection with near-field imaging. *IEEE Microwave Magazine*, 3(1):48–56, 3 2002.

- [22] Thomas Rösch, Reinhard Lorenz, Christine Braig, Stefan Feuerbach, Jrg Rudiger Siewert, Volker Schusdziarra, and Meinhard Classen. Endoscopic ultrasound in pancreatic tumor diagnosis. *Gastrointestinal Endoscopy*, 37(3):347–352, 5 1991.
- [23] T M Kolb, J Lichy, and J H Newhouse. Occult cancer in women with dense breasts: detection with screening US—diagnostic yield and tumor characteristics. *Radiology*, 207(1):191–9, 4 1998.
- [24] Christiane K Kuhl, Simone Schradling, Claudia C Leutner, Nuschin Morakkabati-Spitz, Eva Wardelmann, Rolf Fimmers, Walther Kuhn, and Hans H Schild. Mammography, Breast Ultrasound, and Magnetic Resonance Imaging for Surveillance of Women at High Familial Risk for Breast Cancer. *J Clin Oncol*, 23:8469–8476, 2005.
- [25] D D Adler, P L Carson, J M Rubin, and D Quinn-Reid. Doppler ultrasound color flow imaging in the study of breast cancer: preliminary findings. *Ultrasound in medicine & biology*, 16(6):553–9, 1 1990.
- [26] Sandro J. Stoeckli, Stephan K. Haerle, Klaus Strobel, Sarah R. Haile, Thomas F. Hany, and Bernhard Schuknecht. Initial staging of the neck in head and neck squamous cell carcinoma: A comparison of CT, PET/CT, and ultrasound-guided fine-needle aspiration cytology. *Head & Neck*, 34(4):469–476, 4 2012.
- [27] C.N. Patel, H.M. Salahudeen, M. Lansdown, and A.F. Scarsbrook. Clinical utility of ultrasound and ^{99m}Tc sestamibi SPECT/CT for preoperative localization of parathyroid adenoma inpatients with primary hyperparathyroidism. *Clinical Radiology*, 65(4):278–287, 4 2010.
- [28] Yong Joon Suh, June Young Choi, Su-jin Kim, In Kook Chun, Tae Jin Yun, Kyu Eun Lee, Ji-hoon Kim, Gi Jeong Cheon, and Yeo-Kyu Youn. Comparison of 4D CT, Ultrasonography, and ^{99m}Tc Sestamibi SPECT/CT in Localizing Single-Gland Primary Hyperparathyroidism. *Otolaryngology-Head and Neck Surgery*, 152(3):438–443, 3 2015.
- [29] Claudio Marcocci and Filomena Cetani. Primary Hyperparathyroidism. *New England Journal of Medicine*, 365(25):2389–2397, 12 2011.
- [30] Melanie A. McWade, Constantine Paras, Lisa M. White, John E. Phay, Carmen C. Solórzano, James T. Broome, and Anita Mahadevan-Jansen. Label-free Intraoperative Parathyroid Localization With Near-Infrared Autofluorescence Imaging. *The Journal of Clinical Endocrinology & Metabolism*, 99(12):4574–4580, 12 2014.
- [31] Constantine Paras, Matthew Keller, Lisa White, John Phay, and Anita Mahadevan-Jansen. Near-infrared autofluorescence for the detection of parathyroid glands. *Journal of Biomedical Optics*, 16(6):067012, 2011.
- [32] Daniel E. Abbott, Scott B. Cantor, Elizabeth G. Grubbs, Rachel Santora, Henry F. Gomez, Douglas B. Evans, Jeffrey E. Lee, Think Vu, and Nancy D. Perrier. Outcomes

- and Economic Analysis of Routine Preoperative 4-Dimensional CT for Surgical Intervention in de novo Primary Hyperparathyroidism: Does Clinical Benefit Justify the Cost? *Journal of the American College of Surgeons*, 214(4):629–637, 4 2012.
- [33] Kevin Cheung, Tracy S. Wang, Forough Farrokhyar, Sanziana A. Roman, and Julie A. Sosa. A Meta-analysis of Preoperative Localization Techniques for Patients with Primary Hyperparathyroidism. *Annals of Surgical Oncology*, 19(2):577–583, 2 2012.
- [34] J P Ehlers, S K Srivastava, D Feiler, A I Noonan, and A M Rollins. Integrative Advances for OCT-Guided Ophthalmic Surgery and Intraoperative OCT: Microscope Integration, Surgical Instrumentation, and Heads-Up Display Surgeon Feedback. *PLoS ONE*, 9(8):105224, 2014.
- [35] Despina G Contopoulos-Ioannidis, Evangelia E Ntzani, and John P A Ioannidis. Translation of Highly Promising Basic Science Research into Clinical Applications. *Am J Med*, 114:477–484, 2003.
- [36] Daniele Fanelli. Is sciencereallyfacingareproducibilitycrisis,anddo we need it to?
- [37] C. Glenn Begley and John P.A. Ioannidis. Reproducibility in Science Improving the Standard for Basic and Preclinical Research. *Circulation Research*, 2015.
- [38] Jack W Scannell and Jim Bosley. When Quality Beats Quantity: Decision Theory, Drug Discovery, and the Reproducibility Crisis. 2016.
- [39] Eddy Kuwana and Eva M Sevick-Muraca. Fluorescence lifetime spectroscopy in multiply scattering media with dyes exhibiting multiexponential decay kinetics. *Biophysical Journal*, 83(2):1165–1176, 2002.
- [40] David M Jameson, Enrico Gratton, and Robert D Hall. The measurement and analysis of heterogeneous emissions by multifrequency phase and modulation fluorometry. *Applied Spectroscopy Reviews*, 20(1):55–106, 1984.
- [41] Jing Liu, Yang Sun, Jinyi Qi, and Laura Marcu. A novel method for fast and robust estimation of fluorescence decay dynamics using constrained least-squares deconvolution with Laguerre expansion. *Physics in Medicine and Biology*, 57(4):843–865, 2012.
- [42] Michelle A Digman, Valeria R Caiolfa, Moreno Zamai, and Enrico Gratton. The phasor approach to fluorescence lifetime imaging analysis. *Biophysical Journal*, 94(2):14–16, 2008.
- [43] A D Elder, S M Matthews, J Swartling, K Yunus, J H Frank, C M Brennan, A C Fisher, and C F Kaminski. Application of frequency-domain Fluorescence Lifetime Imaging Microscopy as a quantitative analytical tool for microfluidic devices. *Optics express*, 14(12):5456–5467, 2006.
- [44] Laura Marcu. Fluorescence Lifetime Techniques in Medical Applications.
- [45] Joseph R. Lakowicz. *Principles of Fluorescence Spectroscopy*. Springer {US}, 3rd edition, 2006.

- [46] Pei-Chi Jiang. *Quasi-Real Time Fluorescence Imaging with Lifetime Dependent Contrast*. PhD thesis, University of California, Los Angeles, 2011.
- [47] M Y Berezin and S Achilefu. Fluorescence Lifetime Measurements and Biological Imaging. *Chem. Rev.*, 110(5):2641–2684, 2010.
- [48] Pei-Chi Jiang, Warren S. Grundfest, and Oscar M. Stafsudd. Quasi-real-time fluorescence imaging with lifetime dependent contrast. *Journal of Biomedical Optics*, 16(8):086001, 2011.
- [49] Asael Papour, Zach Taylor, Adria Sherman, Desiree Sanchez, Gregory Lucey, Linda Liao, Oscar Stafsudd, William Yong, and Warren Grundfest. Optical imaging for brain tissue characterization using relative fluorescence lifetime imaging. *Journal of biomedical optics*, 18(6):60504, 2013.
- [50] Asael Papour, Zachary Taylor, Oscar Stafsudd, Irena Tsui, and Warren Grundfest. Imaging autofluorescence temporal signatures of the human ocular fundus in vivo. *Journal of Biomedical Optics*, 20(11):110505, 2015.
- [51] Z. Taylor, I. Kim, J. Pesce, W. Grundfest, and M.S. St. John. Dynamic Optical Contrast Imaging as a Novel Modality to Rapidly Distinguish Oral Squamous Cell Carcinoma From Surrounding Normal Tissue. *International Journal of Radiation Oncology*Biophysics*, 94(4):921, 2016.
- [52] Irene A. Kim, Zachary D. Taylor, Harrison Cheng, Christine Sebastian, Ashkan MacCabi, James Garritano, Bobby Tajudeen, Ali Razfar, Fernando Palma Diaz, Michael Yeh, Oscar Stafsudd, Warren Grundfest, and Maie St. John. Dynamic Optical Contrast Imaging: A Technique to Differentiate Parathyroid Tissue from Surrounding Tissues. *Otolaryngology-Head and Neck Surgery*, 156(3):480–483, 2017.
- [53] Judith A Johnson and Kavya Sekar. NIH Funding: FY1994-FY2019. Technical report.
- [54] Nol Boens, Wenwu Qin, Nikola Basarić, Johan Hofkens, Marcel Ameloot, Jacques Pouget, Jean Pierre Lefèvre, Bernard Valeur, Enrico Gratton, Martin VandeVen, Norberto D Silva, Yves Engelborghs, Katrien Willaert, Alain Sillen, Garry Rumbles, David Phillips, Antonie J W G Visser, Arie Van Hoek, Joseph R Lakowicz, Henryk Malak, Ignacy Gryczynski, Arthur G Szabo, Don T Krajcarski, Naoto Tamai, and Atsushi Miura. Fluorescence lifetime standards for time and frequency domain fluorescence spectroscopy. *Analytical Chemistry*, 79(5):2137–2149, 2007.
- [55] Stijn Keereweer, Pieter B A A Van Driel, Thomas J A Snoeks, Jeroen D F Kerrebijn, Robert J de Jong, Alexander L Vahrmeijer, Henricus J C M Sterenberg, and Clemens W G M Löwik. Optical image-guided cancer surgery: challenges and limitations. *Clinical cancer research : an official journal of the American Association for Cancer Research*, 19(14):3745–3754, 2013.
- [56] Philippe Roudot, Charles Kervrann, and Francois Waharte. Lifetime estimation of moving vesicles in frequency-domain fluorescence lifetime imaging microscopy. *Proceedings - International Symposium on Biomedical Imaging*, 32(10):668–671, 2012.

- [57] J.B Birks. *Photophysics of Aromatic Molecules*. Wiley-Interscience, 1970.
- [58] Douglas Magde, Gail E. Rojas, and Paul G. Seybold. Solvent dependence of the fluorescence lifetimes of xanthene dyes. *Photochemistry and Photobiology*, 1999.
- [59] Arne S. Kristoffersen, Svein R. Erga, Brge Hamre, and yvind Frette. Testing fluorescence lifetime standards using two-photon excitation and time-domain instrumentation: Rhodamine B, coumarin 6 and lucifer yellow. *Journal of Fluorescence*, 2014.
- [60] J. Thomas Brownrigg and Jonathan E. Kenny. Fluorescence intensities and lifetimes of aromatic hydrocarbons in cyclohexane solution: Evidence of contact charge-transfer interactions with oxygen. *Journal of Physical Chemistry A*, 2009.
- [61] N. Nijegorodov, R. Mabbs, and W. S. Downey. Evolution of absorption, fluorescence, laser and chemical properties in the series of compounds perylene, benzo(ghi)perylene and coronene. *Spectrochimica Acta - Part A: Molecular and Biomolecular Spectroscopy*, 2001.
- [62] Mona Mardelli and John Olmsted. Calorimetric determination of the 9,10-diphenylanthracene fluorescence quantum yield. *Journal of Photochemistry*, 1977.
- [63] Klaus Suhling, Liisa M. Hirvonen, James A. Levitt, Pei Hua Chung, Carolyn Tregidgo, Dmitri A. Rusakov, Kaiyu Zheng, Simon Ameer-Beg, Simon P. Poland, Simao Coelho, Robert Henderson, and Nikola Krstajic. Fluorescence lifetime imaging. In *Handbook of Photonics for Biomedical Engineering*. 2017.
- [64] Byung Yong Lee, Kris Behler, Murat Erdem Kurtoglu, Meghan Ann Wynosky-Dolfi, Richard F. Rest, and Yury Gogotsi. Titanium dioxide-coated nanofibers for advanced filters. *Journal of Nanoparticle Research*, 2010.
- [65] Robert D. Cardiff, Claramae H. Miller, and Robert J. Munn. Manual hematoxylin and eosin staining of mouse tissue sections. *Cold Spring Harbor Protocols*, 2014.
- [66] Hani A Alturkistani, Faris M Tashkandi, and Zuhair M Mohammedsaleh. Histological Stains: A Literature Review and Case Study. *Global Journal of Health Science*, 8(3), 2016.
- [67] Pinar Avci, Asheesh Gupta, Magesh Sadasivam, Daniela Vecchio, Zeev Pam, Nadav Pam, Michael R Hamblin, and Semin Cutan Med Surg Author manuscript. Low-level laser (light) therapy (LLLT) in skin: stimulating, healing, restoring. Technical Report 1, 2013.
- [68] Derek Magee, Yi Song, Stephen Gilbert, Nicholas Roberts, Nagitha Wijayathunga, Ruth Wilcox, Andrew Bulpitt, and Darren Treanor. Histopathology in 3D: From three-dimensional reconstruction to multi-stain and multi-modal analysis. *Journal of pathology informatics*, 6:6, 2015.
- [69] Sebastian R Contiguglia, Allen C Alfrey, Nancy L Miller, Donald E Runnells, and Racquel Z Le Geros. Nature of soft tissue calcification in uremia. Technical report, 1973.

- [70] Hussain Fatakdwala, Dimitris Gorpas, John W Bishop, Julien Bec, Dinglong Ma, Jeffrey A Southard, Kenneth B Margulies, and Laura Marcu. Fluorescence Lifetime Imaging Combined with Conventional Intravascular Ultrasound for Enhanced Assessment of Atherosclerotic Plaques: an Ex Vivo Study in Human Coronary Arteries.
- [71] Mark Jenkinson, Peter Bannister, Michael Brady, and Stephen Smith. Improved optimization for the robust and accurate linear registration and motion correction of brain images. *Neuroimage*, 17(2):825–841, 2002.
- [72] David G Lowe. Object recognition from local scale-invariant features. In *Computer vision, 1999. The proceedings of the seventh IEEE international conference on*, volume 2, pages 1150–1157, 1999.
- [73] David G Lowe. Distinctive image features from scale-invariant keypoints. *International journal of computer vision*, 60(2):91–110, 2004.
- [74] Stephen M Smith, Mark Jenkinson, Mark W Woolrich, Christian F Beckmann, Timothy E J Behrens, Heidi Johansen-Berg, Peter R Bannister, Marilena De Luca, Ivana Drobnyak, David E Flitney, and others. Advances in functional and structural MR image analysis and implementation as FSL. *Neuroimage*, 23:S208S219, 2004.
- [75] Martin Urschler, Joachim Bauer, Hendrik Ditt, and Horst Bischof. SIFT and shape context for feature-based nonlinear registration of thoracic CT images. In *International Workshop on Computer Vision Approaches to Medical Image Analysis*, pages 73–84, 2006.
- [76] Arman Rahmim. Advanced motion correction methods in pet. *Iranian Journal of Nuclear Medicine*, 13(2):1–17, 2005.
- [77] Shimon Edelman, Nathan Intrator, and Tomaso Poggio. Complex cells and Object Recognition. 1997.
- [78] Atul Gawande. Two Hundred Years of Surgery. 2012.
- [79] Shelley Jane Spaner, B M Sc, and Garth Loren Warnock. A Brief History of Endoscopy, Laparoscopy, and Laparoscopic Surgery. Technical Report 6, 1997.
- [80] Satyam Kalan, Sanket Chauhan, Rafael F Coelho, Marcelo A Orvieto, Ignacio R Camacho, Kenneth J Palmer, and Vipul R Patel. History of robotic surgery. 4:141–147, 2010.
- [81] Dipen J Parekh, Isildinha M Reis, Erik P Castle, Mark L Gonzalgo, Michael E Woods, Robert S Svatek, Alon Z Weizer, Badrinath R Konety, Mathew Tollefson, Tracey L Krupski, Norm D Smith, Ahmad Shabsigh, Daniel A Barocas, Marcus L Quek, Atreya Dash, Adam S Kibel, Lynn Shemanski, Raj S Pruthi, Jeffrey Scott Montgomery, Christopher J Weight, David S Sharp, Sam S Chang, Michael S Cookson, Gopal N Gupta, Alex Gorbonos, Edward M Uchio, Eila Skinner, Vivek Venkatramani, Nachiketh Soodana-Prakash, Kerri Kendrick, Joseph A Smith Jr, and Ian M Thompson. Robot-assisted radical cystectomy versus open radical cystectomy in patients with bladder

cancer (RAZOR): an open-label, randomised, phase 3, non-inferiority trial. Technical report, 2018.

- [82] Bhagwan Satiani, Thomas E Williams, and Christopher Ellison. The Impact of Employment of Part-Time Surgeons on the Expected Surgeon Shortage. *ACS*, 213:345–351, 2011.
- [83] George F Sheldon and G F Sheldon. The Evolving Surgeon Shortage in the Health Reform Era. *J Gastrointest Surg*, 15:1104–1111, 2011.